**Title**
A Numerical Investigation of Moderate Magnetic Reynolds Number Fusion Liquid Metal Magnetohydrodynamic Flows



**Author**
Kawczynski, Charles Newlin

**Publication Date**
2018

UNIVERSITY OF CALIFORNIA

Los Angeles

# A Numerical Investigation of Moderate Magnetic Reynolds Number Fusion Liquid Metal Magnetohydrodynamic Flows

A dissertation submitted in partial satisfaction

of the requirements for the degree

Doctor of Philosophy in Mechanical Engineering

by

Charles Newlin Kawczynski

2018

ABSTRACT OF THE DISSERTATION

A Numerical Investigation of Moderate Magnetic Reynolds Number Fusion Liquid Metal Magnetohydrodynamic Flows

by

Charles Newlin Kawczynski

Doctor of Philosophy in Mechanical Engineering

University of California, Los Angeles, 2018

Professor Mohamed A. Abdou, Chair

In this study, mathematical and numerical methodologies are developed, and an induction-based incompressible magnetohydrodynamic (MHD) flow solver was created, to study moderate $Re_m$ liquid metal (LM) MHD flows for fusion blanket design. Most LM MHD flow numerical studies in fusion blanket design have traditionally assumed that the magnetic Reynolds number ($Re_m$) is much less than unity. The $Re_m$, a dimensionless parameter in the magnetic induction equation, is a measure of the ratio of convection to diffusion of the magnetic field ($\mathbf{B}$). The low $Re_m$ approximation, also known as the inductionless or quasi-static approximation, assumes that the applied magnetic field is quasi-static and that the ratio of induced to applied magnetic field strength is much less than unity. This assumption is not valid under certain conditions, however. For example, during unsteady plasma events, such as major disruptions, the applied magnetic field ($\mathbf{B}^0$) changes on the order of Tesla per milliseconds. The strongly unsteady applied magnetic field requires the use of the magnetic induction formulation. Furthermore, these conditions may lead to high velocities such that $Re_m$ is greater than unity.

The objectives of this study are to (1) study the effects of moderate $Re_m$ on steady

MHD flows, (2) compare approximate magnetic boundary conditions (BCs) with proper far-field magnetic BCs for moderate $Re_m$ steady MHD flows and our main objective (3) study flow physics of a flow induced from a strongly unsteady applied magnetic field, similar to conditions expected in the LM during a fusion plasma disruption. We limit our scope of the first two objectives to a simple lid-driven cavity (LDC) flow with a transversely applied magnetic field. For the third objective, we consider a long three-dimensional rectangular enclosure (akin to a blanket module) with no-slip conducting walls on all sides and an unsteady applied magnetic field computed from a plasma code, used for the international thermonuclear experimental reactor (ITER).

The $Re_m$ effect on MHD flows was analyzed by considering a LDC MHD flow with a transversely applied magnetic field using proper far-field magnetic BCs. Results show that the flow is mostly two-dimensional (except for the Hartmann layers) when $Re_m < 100$, but becomes more three-dimensional as $Re_m$ increases. The integral kinetic energy and velocity distributions indicate that the $Re_m$ effect on the flow is negligible for $Re_m \lesssim 100$ at steady state, suggesting that approximate magnetic BCs are valid in this range under steady-state conditions. While the flow is unsteady, however, the integral kinetic energy deviated significantly with respect to changes in $Re_m$, indicating that the approximate magnetic BCs are likely invalid during flow unsteadiness. For $0 \leq Re_m \leq 100$, the induced magnetic field magnitude increases linearly with $Re_m$ while its distribution remains qualitatively unchanged. The induced magnetic field energy in the flow domain is higher than the applied one for $Re_m$ values higher than $Re_m \sim 850$. First results of linear and non-linear dynamo tests were performed for the LDC flow problem and while both tests were ultimately inconclusive, the results were analyzed and time-local induced magnetic field generation was observed in the non-linear dynamo test.

The dissertation of Charles Newlin Kawczynski is approved.

J. John Kim

Jonathan M. Aurnou

Jeffrey D. Eldredge

Sergey Y. Smolentsev

Mohamed A. Abdou, Committee Chair

University of California, Los Angeles

2018

*To my parents . . .*

*whose support and encouragement*

*during my childhood led me to science.*

TABLE OF CONTENTS

**1 Introduction** . . . . . **1**

1.1 Background . . . . . 1

1.2 Literature review . . . . . 4

1.2.1 Fusion LM blankets . . . . . 4

1.2.2 Hydrodynamic formulations . . . . . 5

1.2.3 Electromagnetic formulations . . . . . 6

1.2.4 Low $Re_m$ MHD flows . . . . . 10

1.2.5 Moderate $Re_m$ MHD flows . . . . . 11

1.2.6 Magnetic boundary conditions . . . . . 14

1.2.7 Enforcing $\nabla \bullet \mathbf{B} = 0$ . . . . . 16

1.2.8 Plasma disruptions . . . . . 17

1.3 Objectives and scope . . . . . 18

**2 Physical and Mathematical Model** . . . . . **19**

2.1 Governing equations . . . . . 19

2.1.1 Discussion of dimensionless parameters . . . . . 21

2.1.2 Magnetic induction equation in vacuum . . . . . 23

2.2 Magnetic boundary conditions . . . . . 24

2.2.1 Real vacuum boundary conditions . . . . . 24

2.2.2 Pseudo vacuum boundary conditions . . . . . 26

2.2.3 Thin wall boundary conditions . . . . . 27

2.2.4 Decay function boundary conditions . . . . . 27

2.3 Computational challenges . . . . . 28
2.3.1 Enforcing $\nabla \bullet \mathbf{B} = 0$ . . . . . 28
2.3.2 Applying real vacuum boundary conditions . . . . . 28
2.3.3 Challenges with low and variable $\overline{\sigma}$ . . . . . 29
2.3.4 Determining a sufficiently large computational domain size . . . . . 29
2.3.5 Determining a sufficiently small vacuum $\overline{\sigma}$ value . . . . . 30

**3 Code Development . . . . . 32**
3.1 Numerical methodology . . . . . 32
3.1.1 Spatial discretization . . . . . 32
3.1.2 Correction procedure to assure $\nabla \bullet \mathbf{B} = 0$ . . . . . 34
3.1.3 Temporal discretization . . . . . 36

**4 Testing the Code . . . . . 39**
4.1 Hydrodynamic flows . . . . . 39
4.2 Low $Re_m$ MHD flows . . . . . 40
4.3 Moderate $Re_m$ MHD flows . . . . . 44
4.3.1 A 2D pressure-driven moderate $Re_m$ MHD flow . . . . . 44
4.3.2 An unsteady, time-varying applied magnetic field-driven moderate $Re_m$ MHD flow . . . . . 45

**5 Applications . . . . . 48**
5.1 Preliminary tests . . . . . 48
5.1.1 Selecting the electrical conductivity of the insulating outer domain . . 48
5.1.2 Mesh independence study . . . . . 50
5.1.3 Selecting the computational domain size . . . . . 50

5.2 Moderate $Re_m$ MHD flow characterization . . . . . 51
5.2.1 Steady to unsteady flow comparison . . . . . 51
5.2.2 Applicability of the inductionless approximation . . . . . 53
5.2.3 Two-dimensionality . . . . . 61
5.2.4 Frozen magnetic field lines and flux expulsion . . . . . 65
5.2.5 Magnetic field penetration into the vacuum . . . . . 68
5.2.6 Energy balance and distribution as $Re_m$ increases . . . . . 69
5.2.7 Linear and non-linear dynamo tests . . . . . 75
5.3 Magnetic boundary conditions . . . . . 78
5.3.1 Real vacuum magnetic boundary conditions . . . . . 78
5.3.2 Pseudo vacuum magnetic boundary conditions . . . . . 79
5.3.3 Comparison of real and pseudo-vacuum magnetic boundary conditions 82
5.4 LM MHD flows induced by plasma disruptions . . . . . 83

**6 Concluding Remarks . . . . . 89**

6.1 Conclusions . . . . . 89

**A Appendix . . . . . 93**

A.1 Analytic 1D solution to an unsteady applied magnetic field induced flow . . 93

LIST OF FIGURES


1.1 ITER design and blanket module. . . . . 2

1.2 Plasma magnetic and electric current fields. . . . . 2

1.3 Plasma toroidal current and poloidal magnetic field. . . . . 2

1.4 Simplified 1D model for unsteady applied magnetic field. . . . . 3

2.1 Sketch of computational domains of variable electrical conductivity. . . . . 19

2.2 Non-zeros of matrix structure for curl-curl operator, when solved implicitly, for staggered $\mathbf{B}$, variable $\overline{\sigma}$ and mesh $N_{cells} = (3, 3, 3)$. . . . . 30

3.1 Staggered variables on computational cell. . . . . 33

4.1 u-component velocity comparison in cavity center. . . . . 40

4.2 Iso-surfaces of $|\tilde{\mathbf{B}}|$ between $(0 \leq z \leq 0.94)$ for a LDC flow. . . . . 41

4.3 u-component velocity comparison in cavity center at $Re = 400$, $Ha = 45$. . . . . 41

4.4 Normalized streamwise-component of velocity vs $z$ and $y$ for Hunt (a) and Shercliff (b) flows. . . . . 42

4.5 Normalized streamwise velocity distribution for Hunt flow at $Ha = 15000$ and $c_w = 0.01$. . . . . 43

4.6 (a) axial velocity and lines of $\mathbf{B}^0$. (b) lines of $\mathbf{B}^0 + \mathbf{B}^1$. (c) axial velocity comparison at $x = \pi/2, \pi$. . . . . 44

4.7 Effect of $Re_m$ on Hartmann to Poiseuille transition, visualized by the streamwise core velocity, as a function of inverse interaction number $Q$. . . . . 45

4.8 Dimensionless velocity and induced magnetic field solutions for a simplified 1D plasma disruption scenario for several Hartmann numbers. . . . . 46

4.9 Comparison of MOONS computation with a simplified 1D plasma disruption-driven moderate $Re_m$ MHD flow. . . . . 47

5.1 Effect of the electrical conductivity of the insulating outer domain on the computed magnetic energy. . . . . 49

5.2 Grid independence study at $Re_m = 200$. . . . . 50

5.3 Kinetic energy (a) and induced magnetic field energy (b) over time. . . . . 53

5.4 Ratio of the steady-state induced to applied magnetic field energy vs. $Re_m$. . . . 53

5.5 The $u$-component of velocity along $x$ (a) and $y$ (b) directions and $v$-component of velocity along $x$ (c) and $y$ (d) directions in the cavity center. . . . . 56

5.6 The $x$ component of induced magnetic field contours from $x$ direction in the cavity center. . . . . 57

5.7 The $y$ component of induced magnetic field contours from $x$ direction in the cavity center. . . . . 58

5.8 The $z$ component of induced magnetic field contours from $x$ direction in the cavity center. . . . . 59

5.9 The $x$-component electric current along $x$ (a) and $y$ (b) directions and $y$-component electric current along $x$ (c) and $y$ (d) directions in the cavity center. . . . . 60

5.10 The $x$ (a), $y$ (b) and $z$ components of electric current along the $z$ direction in the cavity center for half of the domain. . . . . 61

5.11 $u$ component velocity contours from $x$ direction in cavity center. . . . . 62

5.12 $v$ component velocity contours from $x$ direction in cavity center. . . . . 63

5.13 $w$ component velocity contours from $x$ direction in cavity center. . . . . 64

5.14 Velocity distributions along $z$ direction in cavity center in half domain. . . . . 65

5.15 Velocity distributions along $z$ direction in cavity center in half domain. . . . . 65

5.16 Total magnetic field lines traced in a grid of 10 by 10 points from $z = -1.05$ to $z = 1.05$, along the applied magnetic field direction for (a) $Re_m << 1$, (b) $Re_m = 100$, (c) $Re_m = 500$, and (d) $Re_m = 1000$. The magnetic field lines begin to become frozen to the flow as $Re_m$ increases. . . . . 67

5.17 Magnetic field distributions along $x$ (a) and $y$ (b) directions in the cavity center. 68

5.18 The $x$ (a) $y$ (b) and z (c) components magnetic field components along $z$ direction in the cavity center for half of the domain. . . . . 68

5.19 Graphical representation of energy and energy components. The flows at $Re_m = 1500$ and $Re_m = 2000$ are unsteady. Values were computed at the last time-step for points shown without variation bars. . . . . 71

5.20 The steady-state magnetic energy in different domains. . . . . 73

5.21 Kinetic energy iso-surfaces and three-dimensional velocity streamlines for (a) $Re_m = 1$, (b) $Re_m = 100$, (c) $Re_m = 500$, and (d) $Re_m = 1000$. . . . . 74

5.22 Induced magnetic field energy iso-surfaces and streamtraces for (a) $Re_m = 1$, (b) $Re_m = 100$, (c) $Re_m = 500$, and (d) $Re_m = 1000$. . . . . 75

5.23 Induced magnetic field energy vs time for kinematic dynamo test. . . . . 76

5.24 Kinetic and induced magnetic field energies vs time for full dynamo test at $Re_m = 2000$. $\mathbf{B}^0$ was turned off at $t = 543.255$. . . . . 77

5.25 LDC MHD flow schematic (left). Zoomed view (right). . . . . 78

5.26 Results of a LDC MHD flow using real-vacuum (RV) BCs at $Re = 400$, $Ha = 20$, $Re_m = 100$, $t_{wall} = 0.5$. . . . . 79

5.27 LDC MHD flow schematic for RV (left) and pseudo-vacuum (PV) (right) BCs. . 80

5.28 $|\mathbf{B}^1|^2$ iso-surfaces at $Re = 400$, $Ha = 20$, $Re_m = 100$, $t_{wall} = 0.5$. . . . . 81

5.29 $|\mathbf{B}^1{}_{tangent}|$ at conductor surface for different BCs for $Re_m = 1$. . . . . 82

5.30 $|\mathbf{B}^1{}_{tangent}|$ at conductor surface for different BCs for $Re_m = 100$. . . . . 83

5.31 Our focused region in ITER tokamak. . . . . 85

5.32 Geometry and applied magnetic field configuration. . . . . 85

5.33 The applied magnetic field computed from the DINA plasma code. . . . . 86

5.34 Velocity streamlines for preliminary computations for the plasma disruption scenario. . . . . 86

5.35 The poloidal velocity at $t = 1$. . . . . 86

5.36 The poloidal magnetic field, Lorentz force, and kinetic energy vs. time. . . . . 87

5.37 Zoomed view in the time range $0 \leq t \leq 1$. . . . . 87

5.38 Solid bar: Lorentz force at $t = 0.4$. . . . . 87

LIST OF TABLES

3.1 Locations of input scalar fields and output derivatives when computed on the staggered computational cell. . . . . 33

4.1 Percent error of normalized flow rate $\tilde{Q}$ for 2D MHD duct flow for insulating walls (Shercliff) and conducting walls (Hunt) for $c_w = 0.01$. . . . . 43

5.1 Dimensional parameters for plasma disruption scenario. . . . . 84

5.2 Conversion to dimensional values. . . . . 85

# ACKNOWLEDGMENTS

The past six years have been a fantastic experience, and I am so privileged and grateful to have had the opportunity to pursue a doctoral degree. Now, I would like to take the opportunity to express how thankful I am for all of the support that I have had along the way.

First, I would like to thank my academic support. Namely, Professor Mohamed Abdou and Dr. Sergey Smolentsev for their mentoring, their guidance, and sharing their wisdom. Without them, none of this would have been possible. Professors Jeff Eldredge, Chris Anderson, Craig Schroeder, John Kim, Jonathan Aurnou and Joseph Teran were some of the most inspirational, highly technical, and knowledgeable people I have ever met. They all tolerated my unrelenting questions about computational fluid dynamics, numerical methods, and programming. I owe them great thanks for sharing their knowledge with me. Also, Drs. Peter Huang, Ramakanth Munipalli, and Raffaella D'Auria were extremely helpful with assisting me with using HIMAG and the Hoffman cluster.

Second, I would like to thank my friends and colleagues. Specifically, Dr. Jon Van Lew, Dr. Gautam Pulugundla, Jack Young, Tyler Rhodes, Mahmoud Mohammed, Yi Yan, and Marco Riva were epic lunch companions, invaluable friends, and very helpful technical experts. I found many lunch discussions with Gautam, Tyler, and Moe about machine learning incredibly fascinating and intellectually stimulating. Playing soccer with Jon and Marco helped kept me mentally refreshed. Also, Dr. Cyril Courtessole, Dr. Naveen Vetcha, Dr. Sheida Saeidi, Dr. Krsto Sbutega, and Damien Sutevski were all very encouraging, helpful, inspiring and gave me confidence that my research would eventually pull together.

Third, I would like to thank my family and loved ones. My parents, Sue and Mario, have supported and encouraged me ever since I used to construct elaborate K'NEX creations. They fostered an excellent environment for problem-solving, engineering, and creativity. I indeed would not have conducted this research without my brother, Matt, who encouraged

me to take a huge leap in my life and apply to graduate school in California. Lauren, my sister, was one of the most important role models for me while I grew up during my years in high school and college and she had a significant impact on me as a person. Gabriel, my younger brother, was the best childhood companion a brother could ask for, and he has grown to be an incredibly inspiring person. Drs. Gregory Swedberg and Winifred V. Quinn hold the award in my book for the most professional, respected, and wisest people I know. They are hugely responsible for my interest and motivation to pursue a doctoral degree in the first place, and they have shared invaluable advice with me along the way. Ted and Darlene Bradley have been the best parents-in-law a future husband could hope for, and our Vegas trips have been some of my favorite bonding experiences to date, and I look forward to many more in the future. Finally, I would like to thank Christa Bradley, my fiancé. I cannot imagine a better life partner. Our Las Vegas trips, wonderful discussion-filled walks at Runyon Canyon, and exploring the endless sea of Los Angeles restaurants has been unforgettable. Christa, you are my rock and the love of my life.

# VITA

| | |
|---|---|
| 2012–2018 | Ph.D. candidate in magnetohydrodynamic flows under Professor Mohamed Abdou and Dr. Sergey Smolentsev, mechanical engineering department, University of California Los Angeles, California, USA. |
| Winter 2017 | Teacher Assistant, University of California Los Angeles, Fluid-particle and fluid-structure interactions in microflows. |
| Summer 2017 | Engineering consultant for magnetohydrodynamic code development, Hypercomp Inc., California, USA. |
| Winter 2016 | M.S. (Mechnical Engineering), University of California Los Angeles, USA. |
| Fall 2016 | Teacher Assistant, University of California Los Angeles, Introduction to computer programming with MATLAB. |
| 2011–2012 | Research assistant in precision-controlled nano-structure fabrication under Professor Qingze Zou, mechanical engineering department, Rutgers University, New Jersey, USA. |
| Spring 2012 | B.S. (Mechnical Engineering), Rutgers University, New Jersey, USA. |
| 2010–2012 | Undergraduate researcher in radiative heat transfer under Professor Zhixiong Guo, mechanical engineering department, Rutgers University, New Jersey, USA. |
| Spring 2012 | Supplemental Instructor, Rutgers University, Calculus II. |
| Fall 2011 | JJ Slade Scholar, Rutgers University. |
| Summer 2011 | Fellowship, New Jersey Space Grant Consortium, New Jersey, USA. |
| Fall 2009 | Undergraduate researcher in flight mechanics and image processing under Professor Mitsunori Denda, mechanical engineering department, Rutgers University, New Jersey, USA. |

PUBLICATIONS AND PRESENTATIONS

**C. Kawczynski**, S. Smolentsev & M. Abdou, "Characterization of the Lid-Driven Cavity MHD Flow at Moderate Magnetic Reynolds Numbers using Far-Field Magnetic Boundary Conditions". Submitted.

S. Smolentsev, M. Abdou, C. Courtessole, G. Pulugundla, F-C. Li, N.B. Morley, R. Munipalli, P. Huang, **C. Kawczynski**, J. Young, T. Rhodes, Y. Yan, "Review of recent MHD activities for liquid metal blankets in the US", Proceedings of the 10th PAMIR Int. Conf. on Fundamental and Applied MHD, pp. 512-516, June 20-24, (2016), Cagliari, Italy.

**C. Kawczynski**, S. Smolentsev & M. Abdou, "An induction-based magnetohydrodynamic 3D code for finite magnetic Reynolds number liquid-metal flows in fusion blankets". Fusion Eng. Des. 25 (2016). doi:10.1016/j.fusengdes.2016.02.088

Poster presentation on "An induction-based MHD 3D code for finite magnetic Reynolds number liquid-metal flows in fusion blankets", International Symposium on Fusion Nuclear Technology (ISFNT), International Convention Center, Jeju Island, South Korea, Fall 2015.

G. Pulugundla, S. Smolentsev, T. Rhodes, **C. Kawczynski** & M. Abdou, "Transition To A Quasi-fully Developed Mhd Flow In An Electrically Conducting Pipe Under A Transverse Non-uniform Magnetic Field". Am. Nucl. Soc. 68, 684689 (2015).

Oral presentation on "Radiative heat transfer in mirror light pipes using Monte-Carlo method", Center for Advanced Infrastructure and Transportation, Rutgers University, New Jersey, USA, August 2011.

# CHAPTER 1

# Introduction

## 1.1 Background

Magnetohydrodynamic (MHD) flows are often categorized by the ratio of magnetic field ($\mathbf{B}$) convection to diffusion[1]. The magnetic Reynolds number ($Re_m$), an estimate for this ratio, is a dimensionless parameter in the magnetic induction equation. Astrophysical MHD flows (where $Re_m$ generally is on the order of $10^{10}$-$10^{20}$, Ref. [1]) and liquid metal (LM) MHD flows in engineering applications (where $Re_m$ is typically less than 1) have been studied for years. The $Re_m$ has traditionally been assumed to be small in engineering applications; however, Ref. [2] showed that $Re_m$ could be as high as five or ten in a fusion energy reactor blanket when computed using the long banana-shaped duct length. Additionally, $Re_m$ may be appreciably large in LM MHD flows during unsteady plasma events, such as major disruptions, edge-localized modes, and vertical displacements, when changes in plasmas occur on the order of [T/ms].

In a tokamak fusion reactor (Fig. 1.1), plasma circulates in the toroidal direction (Fig. 1.2) and, due to differential poloidal current wiring, rotates along the poloidal direction. The plasma is confined using a strong applied magnetic field ($\mathbf{B}^0$), and the plasma motion induces its own induced magnetic field ($\mathbf{B}^1$). Plasma disruptions are a sequence of events including a thermal quench, current quench and loss of vertical position, where the toroidal plasma current rapidly drops and, as a result, the poloidal applied magnetic field drops (Fig. 1.3). The order of these events determines the type of disruption, including major disruptions

[1]Technically, $\mathbf{H} = \mathbf{B}/\mu_m$ often denotes the magnetic field and $\mathbf{B}$ magnetic induction ($\mu_m$ is the magnetic permeability). However, many papers in the literature use $\mathbf{B}$ to denote the magnetic field and these variables are often interchanged as is done in the present work.

and vertical displacement events. During the current quench, the plasma current decreases, resulting in eddy currents in the structure. Plasma currents that collide with the wall, called halo currents, travel into the structure and interact with the constant toroidal magnetic field to induce electromagnetic (EM) forces on the structure during the loss of vertical position (see Ref. [3]). The intense EM forces will also interact with LM flows, exterior to the plasma-facing components, and will induce high velocities in the LM. These high LM velocities will interact with the applied magnetic field and induce their own magnetic field, not to be confused with the induced magnetic field by the plasma motion.

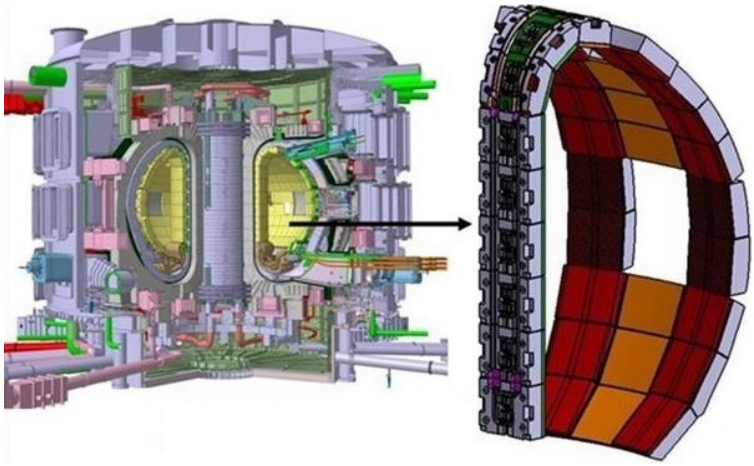

Figure 1.1: ITER design and blanket module.

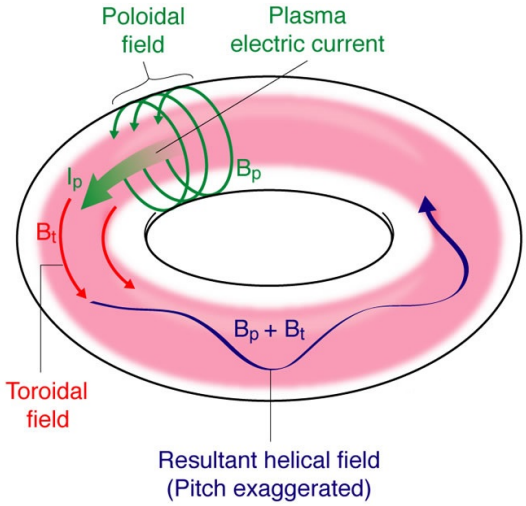


Figure 1.2: Plasma magnetic and electric current fields.

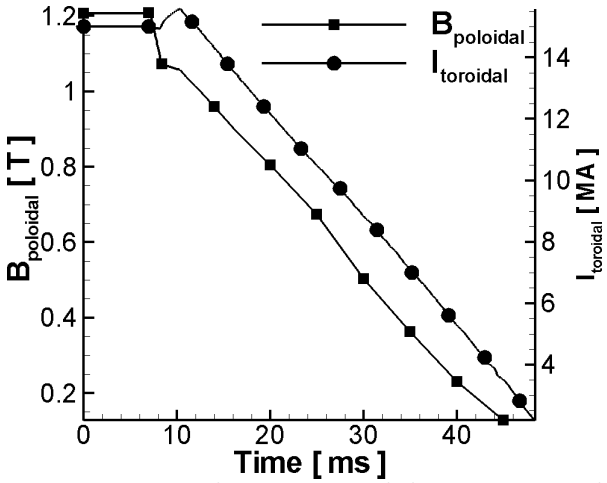


Figure 1.3: Plasma toroidal current and poloidal magnetic field.

Numerical codes play a crucial role in design and prediction for LM MHD flows. However, most numerical LM MHD flow studies in the past assumed $Re_m << 1$ and utilized electric potential ($\phi$) as the main EM variable. One limitation of the $\phi$-based formulation is that it does not apply to truly unsteady processes. In this study, we are interested in LM MHD flows in the presence of plasma disruption-similar applied magnetic fields (which fluctuate strongly in time). Modeling an MHD flow in the presence of a strongly unsteady applied magnetic field requires a numerical MHD code that does not assume low $Re_m$.

The LM velocity in an unsteady applied magnetic field was computed by Ref. [2] using an order of magnitude estimate, conducted by comparing terms in the induction and momentum equations. This zero-dimensional model lacks information about the magnetic and velocity field distributions. Therefore, to more concretely motivate our study, an analytic solution was derived [in § (A.1)] for a simplified 1D model of a steady and fully developed MHD channel flow with a constant $B_{toroidal}$ and time-varying $B_{poloidal}$ (Fig. 1.4) using material properties typical of a fusion blanket.

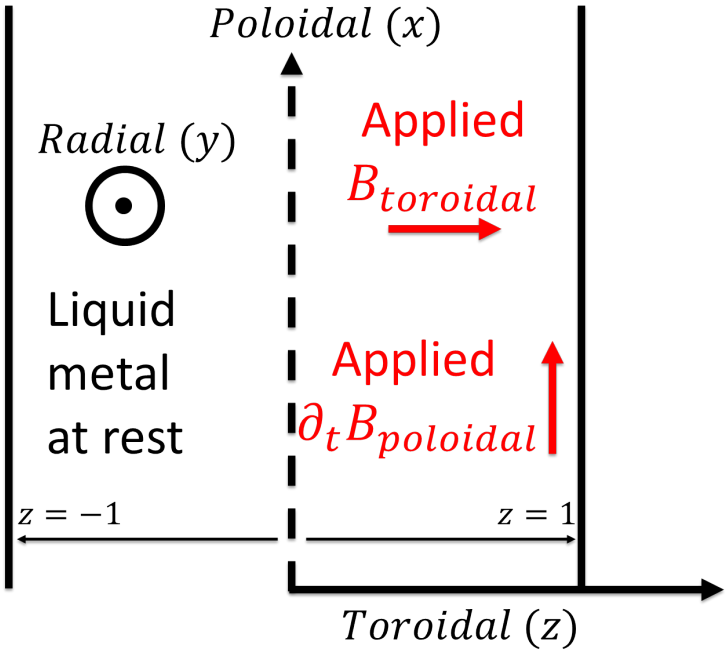

Figure 1.4: Simplified 1D model for unsteady applied magnetic field.

Based on this analysis, maximum LM velocities reach as high as 20 [m/s], depending on

the magnitude of the toroidal field and rate of the decreasing poloidal field. This simplified model provides quantitative evidence that LM flow induced from strongly time-varying applied magnetic fields in a fusion environment can result in $Re_m$ above unity.

It is worth noting that when $Re_m$ surpasses a critically large value under the right conditions, perturbations of the induced magnetic field grow and become self-sustained, i.e., a dynamo effect (Ref. [4]) occurs. This effect is responsible for the Earth's sustained magnetic field, as well as many other planetary and astrophysical magnetic fields from LM and plasma motion. To provide a quantitative idea of critical $Re_m$ values, the $Re_m$ of the Earth's outer core is of the order 100 (Ref. [5]). The conditions required for a given flow to demonstrate dynamo-type physics is an actively researched area today. Some necessary, but not sufficient, ingredients are known [e.g., sufficient dissymmetry and hydrodynamic helicity, see Ref. [1, 6]] and will be discussed later sections.

## 1.2 Literature review

### 1.2.1 Fusion LM blankets

Thermonuclear fusion reactor designs that utilize Deuterium-Tritium (DT) require a modular component, called the "blanket", exterior to the magnetically confined plasma. The blanket's primary role is to extract heat and breed Tritium which, in LM breeder designs, is achieved by pumping LM (e.g., lead Lithium) throughout the blanket, in a series of segments such as manifolds, bends, and straight ducts. Incoming 14 Mega electron-volt (MeV) neutrons ejected from the plasma interact (see Ref. [7]) with Lithium in the blanket resulting in Tritium and heating of the LM, which are extracted for fuel recycling and power respectively. Pumping LM fluids through the blanket pose difficult physical and engineering challenges because, in addition to difficulties with the harsh fusion environment, MHD flow pressure drops are typically much more significant compared to their hydrodynamic counterparts and may result in pressure stresses that exceed the allowable structural limits (Ref. [8]).

Reference [9] proposed an approach to further mature incompressible MHD codes via

collaborative numerical code verification and validation between researchers around the world for five selected MHD flows. The configuration of these suggested flows is briefly mentioned here. They include 1) a fully developed two-dimensional (2D) laminar steady MHD duct flow in a uniform and transversely applied magnetic field with conducting and non-conducting walls, 2) a three-dimensional (3D) laminar steady MHD square duct and pipe flow in an applied fringing magnetic field with conducting walls, 3) a quasi-two-dimensional (Q2D) turbulent MHD flow in a rectangular conducting duct with a transversely applied magnetic field, 4) a fully 3D MHD turbulent flow in a conducting duct with a uniform and transversely applied magnetic field and a magnetic obstacle and 5) a rectangular duct MHD flow with heat transfer.

Liquid metal MHD flows with heat transfer (mixed convection) in straight ducts were numerically studied (Ref. [10]) in the context of fusion blanket modules. Here, both buoyancy opposed and buoyancy assisted poloidal flows were considered. Details of the United States (US) Dual-Cooled liquid Lithium (DCLL) blanket and a qualitative description of the expected MHD flow phenomena were discussed. Analytic solutions for mixed convection were derived. They found that Q2D turbulence and convection effects were dominant. Also, they observed that locally reversed flows could exist and that moderate velocity and volumetric heating were favorable in the mixed flow regime, where buoyancy potentially dominates forced flow.

### 1.2.2 Hydrodynamic formulations

For hydrodynamic flows, the two most common formulations include using primitive variables of velocity-pressure ($\mathbf{u}$-$p$) and vorticity-stream function ($\omega$-$\psi$). The vorticity-stream function formulation was successfully used for a 3D hydrodynamic incompressible lid-driven cavity (LDC) flow (Ref. [11]) for Reynolds numbers ($Re$) between 400 and 2000. Reynolds number estimates the ratio of inertial to viscous forces. They found the formulation to provide computationally efficient and accurate results. This formulation was also used in a 2D hydrodynamic LDC flow (Ref. [12]) for $Re$ up to 10,000. Here, streamlines were plotted for

different $Re$ and vortex locations were reported. The $\omega$-$\psi$ formulation is especially useful when only two components of the velocity exist because the resulting system of equations simplifies to a scalar transport equation, which both decreasing the required computational effort by a factor of three and automatically enforces incompressibility.

### 1.2.3 Electromagnetic formulations

Several EM formulations have been developed over the years. EM formulations are derived from Maxwell equations, consisting of 1) Gauss's law of electric charge, 2) Faraday's law of electromagnetic induction, 3) the conservation of magnetic flux (i.e., the experimental absence of magnetic monopoles), and 4) the Ampére-Maxwell law of electric current and magnetic flux. In addition, Ohm's law is an important equation that relates the induced electric currents to the electric field ($\mathbf{E}$) and the velocity of conducting fluid in the presence of a magnetic field. The EM formulations have different mathematical properties, computational advantages, disadvantages, and require different boundary condition (BC) considerations. The most commonly used EM formulations include the electric potential ($\phi$), vector potential ($\mathbf{A}$), electric current density ($\mathbf{j}$), low $Re_m$ induction, and finite $Re_m$ induction formulations. Here, we discuss them in more detail.

First, a brief discussion on terminology is warranted. We define the word "finite" as a fixed amount that is not infinitely small and not infinitely large. This definition indicates that convection and diffusion both contribute to the induction equation for finite $Re_m$ MHD flows. Finite is occasionally used in place of "moderate" for a variety of vocabulary and because both are used in the literature.

#### 1.2.3.1 Electric potential formulation

The $\phi$-formulation is based on the assumption that time-changes in the magnetic field are negligible. By Faraday's law, this means that the electric field ($\mathbf{E}$) is curl-free and may be recast, using a vector identity, as the gradient of a scalar field ($\phi$). The result is that $\phi$ is governed by a Poisson equation, obtained by taking the divergence of Ohm's law. The

$\phi$-formulation has been successfully used in a myriad of low $Re_m$ MHD flows and is a popular choice for good reasons. This formulation requires only the solution of a scalar field, governed by a Poisson equation, with BCs that easily relate to electric current. Here, a few studies that used the $\phi$-formulation are briefly described.

Linear stability analysis of an MHD square duct flow with conducting and insulating walls with a transversely applied magnetic field was investigated using the $\phi$-formulation (Ref. [13]). Here, perturbation equations were solved using a vector stream-function formulation with a spectral collocation method. Disturbance amplitudes were analyzed and reported. They found the most dangerous instability modes, near $Ha \sim 6$, resulted from the vorticity component along the applied magnetic field direction.

MHD flow instabilities and transition in ducts with conducting walls in the presence of a transversely applied magnetic field were numerically investigated by Ref. [14]. Here, the flow was unsteady and spatially periodic, with Shercliff jet detachment from the walls. They found perturbations in kinetic energy increased two orders of magnitude past a critical Reynolds number, which resulted in a reduction of the mean velocity and Shercliff jet thickening.

#### 1.2.3.2 Vector potential formulation

The vector potential ($\mathbf{A}$) formulation involves mathematically relating $\mathbf{A}$ to the magnetic field via $\mathbf{B} = \nabla \times \mathbf{A}$. One glaring advantage of this formulation is that it automatically enforces $\nabla \bullet \mathbf{B} = 0$ by a vector identity, a non-trivial difficulty, which is easily confirmed by taking the divergence of both sides of $\mathbf{B} = \nabla \times \mathbf{A}$. This is especially useful when only two components of $\mathbf{B}$ exist because, similar to the 2D vorticity-stream function formulation, this results in only a scalar transport equation instead of a vector transport equation. Here, a few studies that used the $\mathbf{A}$-formulation are described.

The $\mathbf{A}$-formulation was successfully used in studying magnetic flux expulsion (Ref. [15]) in a kinematic 2D MHD unsteady flow with a prescribed velocity field. Here, several flow configurations were analyzed, including an isolated eddy, a single eddy and single and double band of eddies with vertical and horizontal applied magnetic field. Here, a fourth-order

finite-difference method (FDM) was used to approximate spatial and temporal derivatives. The induced magnetic field energy was monitored as a function of time and plotted for several $Re_m$ up to 1000. The induced magnetic field energy was analyzed with respect to the timescales in terms of $Re_m$. They found that the time for induced magnetic field energy to reach a steady-state could be estimated by $\tau \sim Re_m^{1/3} L/U$. For large $Re_m$, they found the magnetic resistive time to be $\tau_\eta \sim Re_m L/U$.

A spherical shell dynamo was numerically studied using pseudo-vacuum (PV) magnetic BCs (Ref. [16]) to provide a benchmark for numerical dynamos. In this study, codes from several authors were compared with various formulations and numerical methods. Here, authors used the induction and vector potential formulations. The numerical procedures used by the authors ranged from spectral and pseudo-spectral codes with spherical harmonics, Chebyshev polynomials to FDM, finite-volume method (FVM), and finite-element method (FEM).

#### 1.2.3.3 Electric current formulation

The electric current density formulation was applied in Ref. [17] and applied to several low $Re_m$ MHD wall-bounded flows. The clear advantage of this formulation is that a natural use of Dirichlet BCs can be used to ensure no currents escape the conducting boundary. The disadvantage of the **j**-formulation is that it requires the solution of a vector field, opposed to a scalar field as in the $\phi$-formulation. Here, the formulation was applied to numerically study an MHD flow duct flow in a transversely applied magnetic field, an MHD duct flow in a transversely applied fringing magnetic field and an MHD flow past a magnetic obstacle. Here, a FDM was used to solve the governing equations. A fair agreement was found in comparison with analytic solutions and numerical data using the **B**-formulation.

#### 1.2.3.4 Low $Re_m$ induction formulation

The low $Re_m$ induction formulation is mathematically equivalent to the $\phi$-formulation. There are differences, however. The $\phi$-formulation involves computing the transport of a scalar field,

while the low $Re_m$ induction formulation involves computing the transport of a vector field ($\tilde{\mathbf{B}} = Re_m^{-1}\mathbf{B}^1$). Here, $\tilde{\mathbf{B}}$ is a scaled (by $Re_m^{-1}$) induced magnetic field such that $\mathbf{B}^1$ will have the same *distribution* as $\tilde{\mathbf{B}}$ in the asymptotic limit as $Re_m$ approaches zero. Furthermore, the currents computed for the low $Re_m$ induction formulation, $\mathbf{j} = \nabla \times \tilde{\mathbf{B}}$, and finite $Re_m$ formulation, $\mathbf{j} = Re_m^{-1}\nabla \times \mathbf{B}^1$, become equal as $Re_m$ approaches zero. Examples of this formulation used in the literature are discussed in the next section.

#### 1.2.3.5 Finite $Re_m$ induction formulation

The finite $Re_m$ induction formulation, or **B**-formulation, is used in our study and has been used in many MHD studies at high $Re_m$ but appears far less in the literature for low $Re_m$ MHD studies, where the $\phi$-formulation is often used. The formulation is derived by combining the Ampére-Maxwell equation, Faraday's law, Ohm's law, and eliminating the electric current and electric fields. The result is a single equation in terms of the magnetic field. Here, a few studies that used the **B**-formulation will be described.

The validity of the low $Re_m$ approximation was investigated (Ref. [18]) in the context of a natural convection MHD flow in a 2D square cavity using the **B**-formulation. In this study, the flow was driven by a temperature gradient between two walls with a uniformly applied magnetic field along the temperature gradient direction. Here, the **B**-formulation was compared with the low $Re_m$ formulation and solved the governing equations using a FVM for $Re_m$ up to 1. The distinction between the velocity and magnetic field length scales used in the $Re_m$ definition was discussed. This distinction can result in significant magnetic convection, even at low $Re_m$, if the magnetic length scale is significantly larger than the velocity scale. They found a significant difference between low and moderate $Re_m$ MHD flows, but especially at high Grashof ($Gr$) and Hartmann numbers ($Ha$). The Grashof number estimates the ratio of buoyancy to viscous forces and Hartmann number squared estimates the ratio of EM to viscous forces respectively.

Numerical computations of a 3D LDC moderate $Re_m$ MHD flow were performed (Ref. [19]) using the **B**-formulation for $Re_m$ up to 1000. BCs in this study were inappropriately applied

at the fluid boundary domain, however. Induced magnetic fields in conducting fluids are free to pass beyond the conducting fluid, solid material, and even vacuum. Hence, results here are unphysical and unsuited as a benchmark for experiments and numerical studies.

### 1.2.4 Low $Re_m$ MHD flows

Due to the non-linear nature of the MHD equations, analytic solutions are known for only a small set of simplified flows. Analytic solutions to steady-state fully developed low $Re_m$ MHD duct flows with a transversely applied magnetic field for insulating (Ref. [20]) and conducting (Ref. [21]) walls were found respectively. Here, solutions were formed by Fourier series expansions, which simplify to hyperbolic functions after applying BCs. These analytic solutions are an excellent first step for numerical code benchmarks.

Fully developed LM MHD rectangular duct flows with flow channel inserts (FCIs) were studied by Ref. [22] using materials with different physical properties. Here, a code was developed using the low $Re_m$ formulation along with a FVM to solve the steady MHD equations. The resulting code was accurate up to $Ha \sim 10^4$ and could be used to simulate flows with FCIs.

Liquid metal MHD flow in rectangular conducting and non-conducting ducts with heat transfer and a transversely applied magnetic field were experimentally and numerically analyzed under fusion relevant conditions by Ref. [23]. Advantages and disadvantages of laminar and turbulent regimes were addressed. They found that turbulent mixing enhanced heat transfer without significantly increasing the pressure drop. They also suggested that 1) poloidal ducts near plasma-facing walls are flat along the toroidal direction and 2) circular cross-section for toroidal flow in plasma-facing cooling ducts is preferable.

Instabilities of LM MHD flows with inflectional velocity profiles were experimentally and numerically investigated in Ref. [24]. Here, the induced flow results from current injection into an enclosed cavity, where the flow circulates. Experiments were compared with numerical computations using a Q2D model and a full 3D model.

Two-dimensionality was experimentally investigated (Ref. [25]), where electric current was injected into a cubic container on one side of the container with an applied magnetic field. Flow velocity was measured on both sides. Flow velocities matched well on both sides of the cubic container as the applied magnetic field increased, demonstrating two-dimensionality.

A Q2D turbulent MHD flow model, assuming low $Re_m$, was developed (Ref. [26]) for electrically insulating walls. The Q2D equations, obtained by integrating along the applied magnetic field direction (where the flow is 2D except for the thin Hartmann layers), are adopted and modified to account for turbulent fluctuations. Here, they applied the model to the MATUR experiment (Ref. [27]) and found an excellent match.

Direct numerical simulation (DNS) computations of a turbulent 3D square duct MHD pressure-driven flow with a transversely applied magnetic field was performed (Ref. [28]). Here, the $\phi$-formulation was used, and the incompressible momentum equations were solved using a fractional-step method. Reynolds stresses were reported at several Reynolds numbers, and the turbulent kinetic energy budget was analyzed. They found that the magnetic field significantly affects the secondary flow and that the magnetic field produces both a source and a sink to the turbulent kinetic energy.

### 1.2.5 Moderate $Re_m$ MHD flows

An induction-based EM formulation was used to numerically study LM MHD flow in a square duct with heat transfer in Ref. [29] (1979). Here, the effect of wall conductivity was investigated in terms of axial velocity, pressure drop, and mean Nusselt number.

The $Re_m$ effect was studied for a steady kinematic MHD flow in the context of dynamo action (Ref. [30]) using an iterative scheme to compute the induced magnetic field using a series expansion as a function of $Re_m$. Here, a prescribed velocity profile was used in a cylindrical geometry, and the steady induction equation was solved in orders of $Re_m$, each requiring its own set of BCs based on the physics of the specific order of the induced magnetic field. This decomposition permitted the analysis for each order of the induction mechanism.

They found that magnetic BCs may be important when the magnetic dissipation length is not small compared to the flow integral scale. They also found that external layers of conducting materials behave very differently compared to an infinite conducting medium.

The first numerical demonstration of the Earth's magnetic field reversal was conducted by Ref. [31] in 1995. Here, the full incompressible MHD and thermal energy equations are solved in a rapidly rotating spherical shell with a finite electrically conducting inner core. All conditions are similar to that of Earth, except the inner core boundary heat flux, which was slightly higher. The induced magnetic field is maintained for over 40,000 years and has energy at least three orders greater than the kinetic energy.

A turbulent MHD channel flow was numerically studied (Ref. [32]), using large eddy simulation (LES) to investigate the growth of the mean streamwise magnetic field generated from turbulent fluctuations using a Reynolds-averaged Navier-Stokes (RANS) model. They found that cross-helicity caused the primary production term in the growth of the mean streamwise magnetic field.

The growth of magnetic field self-excitation was first observed in the Riga Dynamo facility (Ref. [5]), where a molten sodium flow was induced in a cylindrical container by propellers. They found that the magnetic field excitation changed from a slow decay to slow growth when increasing the flow velocity beyond a critical value. This result was independently confirmed (Ref. [33]). Later, the magnetic field saturation regime was studied (Ref. [34]).

Numerical simulations of a turbulent magnetic dynamo, closely mimicking the Riga-dynamo experiment, were conducted by Ref. [35]. A hybrid RANS/DNS approach is used to solve the coupled induction and momentum equations in a cylindrically contained flow, induced with propellers. The induced magnetic field frequencies and amplitudes were analyzed and compared with the original experiment.

A fluctuating dynamo, where the growth of magnetic fluctuation energy is equal to or less than the largest length scale, was numerically studied at low, but finite, magnetic Prandtl number in Ref. [36]. Here, a non-helical randomly forced flow results in a homogeneous

turbulent conducting fluid in a periodic cube. They found that the growth rate of the magnetic fluctuation energy asymptotes as the Reynolds number increases.

The unsteady Lorentz Force response at moderate $Re_m$ was studied in Ref. [37]. Here, a solid conducting bar was prescribed a velocity in the presence of an applied fringing magnetic field, akin to a permanent magnet. They found a linear response for the Lorentz force at low $Re_m$ values and saturation at higher values.

Several kinematic dynamo studies were conducted (see Refs. [38, 39]) to study the effect of electrical conductivity on the critical $Re_m$ at which magnetic reconnection, a process where induced magnetic field line reconfiguration releases thermal energy, occurs.

The effect of $Re_m$ was numerically studied on a 2D MHD flow around a circular cylinder in Ref. [40]. Here, the **A**-formulation was used to enforce the divergence-free constraint, a FDM was used to approximate derivatives, and a multigrid method was used to solve the resulting system of equations. They found that flow separation is nearly independent of the fluid conductivity when the low interaction number ($N$) is low. The interaction number estimates the ratio of electromagnetic to inertial forces. At high interaction number, however, flow separation is significantly affected by the fluid conductivity.

Numerical computations were performed to analyze the decay homogeneous turbulent MHD flow low $Re_m$ and at moderate $Re_m$ up to 20 (Ref. [41]). Computations were performed in a periodic box using spectral codes. Kinetic energy was monitored as a function of time and a quasi-linear (QL) model was suggested for MHD flows where $Re_m$ is moderate. Their suggested model neglects the nonlinear term in the induction equation while retaining the unsteady term, maintaining the linearity of the induction equation. Results were reported based on this QL model in comparison to the low and moderate $Re_m$ formulations.

A 2D channel moderate $Re_m$ pressure-driven periodic MHD flow was semi-analytically studied first by Ref. [42], and then numerically (using DNS) by Ref. [43]. This study was also used as a benchmark in our previous paper (see Ref. [44]). Here, a 2D non-uniformly applied magnetic field imposed a periodic Lorentz force on a pressure-driven fluid. Ref. [43]

performed simulations in two flow regimes, a steady Hartmann regime, and an unsteady Poiseuille regime. Here, they used a well tested FDM with 2nd-order-accurate central difference scheme in space and 2nd-order-accurate time-marching. Magnetic flux conservation is enforced by solving for the magnetic field in Fourier space and reconstructing the last component from the $\nabla \bullet \mathbf{B} = 0$. They analyzed the effect of $Re_m$ on the transition and compared Q2D models with full induction formulations. They found that increasing $Re_m$ significantly increased the kinetic energy of the Poiseuille regime, where magnetic reconnection occurred. This MHD flow is a very attractive benchmark problem because the computational domain is 2D, allowing for fast computations and moderate $Re_m$ effects. Its unfavorable feature, however, is that electrical currents are assumed to be infinitely long and, therefore, do not close.

Numerical computations of a turbulent duct moderate $Re_m$ MHD flow were performed (Ref. [45]), where the effect of $Re_m$ on turbulent kinetic energy and flow relaminarization was analyzed. Here, the same numerical code as in Ref. [43], with new implicit schemes implemented, was used. A boundary element method (BEM) was utilized to implement real-vacuum (RV) magnetic BCs, discussed more in § (2.16). They found that increasing $Re_m$ tended to destabilize the flow if near the laminarization threshold. They also found that turbulent kinetic energy was significantly larger at high $Re_m$ compared to low $Re_m$ for the same $Re$ and $Ha$ near the laminarization threshold.

### 1.2.6 Magnetic boundary conditions

An integro-differential formulation was developed (Ref. [46]) to enforce non-local magnetic BCs ($\mathbf{B}^1 = \mathbf{0}$ very far from the conducting domain) by solving an integral equation at the conductor boundary. This approach is elegant and does not require extending the computational domain. However, it requires the solution of a dense and non-symmetric partial integro-differential equation. The component of $\mathbf{B}$ orthogonal to the surface presents no severe difficulty and can be computed from Faraday's law. The tangential components of $\mathbf{B}$,

however, are computed[2] using the linear transformation $\mathbf{n} \times \mathbf{B} = G(\mathbf{B} \bullet \mathbf{n})$ on the conductor boundary. Here, $\mathbf{n}$ is the outward normal unit vector, and $G$ is a non-symmetric dense matrix and may be computed once if the computational mesh does not change with time (see Refs. [47, 36]).

Reference [48] numerically studied kinematic dynamos to compare PV BCs and magnetic permeability jump conditions ($\mathbf{B}^1 = \mathbf{0}$) against RV BCs in a cylindrical system, similar but simplified compared to the Riga experiments. They found that the magnetic eigenmodes in the fluid were similar with both PV and magnetic permeability jump conditions and that high magnetic permeability jump conditions always decreases the critical $Re_m$.

Magnetic BCs of turbulent incompressible MHD flow of an infinite layer of fluid, heated from below, were numerically studied in Ref. [49]. The compared magnetic BCs included 1) PV BCs, 2) vanishingly small induced magnetic field and 3) RV BCs. Here, a 6th-order compact FDM is used to approximate spatial derivatives. Crank-Nicholson and Adams-Bashforth schemes are used for time-marching and $\mathbf{u}$, and $\mathbf{B}^1$ are enforced to be solenoidal by a projection method. They found that fluctuations in the induced magnetic field energy using RV BCs was consistently less compared to the other two BCs for all values of $|\mathbf{B}^1|$ above a critical value.

Thin wall magnetic BCs, first used as far back as 1956 (Ref. [50]), are applied at the *fluid* boundary and are based on the assumption that currents in the wall are approximately uniform. This BC has the advantage of further truncating the computational domain, compared to PV BCs. The wall conductance ratio ($c_w$) is a parameter in the thin wall BCs that roughly estimates the ratio of electric currents in the wall to the Hartmann layer. If $c_w = 0$, then the walls are electrically insulating. PV BCs have been used extensively for low $Re_m$ MHD studies, but are not valid for moderate $Re_m$ MHD flows and their accuracy in moderate $Re_m$ MHD flows has not yet been studied. These magnetic BCs can be readily applied in the context of the magnetic field and electric current formulations (Ref. [17]).

[2]Assuming the no-flow through velocity BC.

Boundary conditions used for low $Re_m$ MHD flows with thin Hartmann layers were suggested in Ref. [51]. Here, these BCs are based on the observation that flow entering and leaving the boundary layer (the wall-normal component) is small. This method allows numerical computations to avoid meshing in the very fine region where the boundary layer exists.

The effect of magnetic BCs on the onset of dynamo action (Ref. [52]) was analyzed in the context of the Riga and Karlsruhe experiments. Here the kinematic MHD equations are solved by an expansion of Bessel functions. Here, walls of different thickness and material properties (electrical conductivity and magnetic permeability) were added to conditions similar to the Riga and Karlsruhe experiments to analyze their sensitivity to the onset of dynamo physics. They found that adding an external conducting wall results in a reduction of the dynamo instability threshold, which they claim to be the result of a change in electric current paths.

### 1.2.7 Enforcing $\nabla \bullet \mathbf{B} = 0$

A projection method was first proposed to enforce magnetic flux conservation ($\nabla \bullet \mathbf{B} = 0$) (Ref. [53]) because neglecting errors in this constraint can lead to unphysical forces in the momentum equation. This method is insensitive to initial conditions (ICs) and BCs but requires a Poisson equation solution for a scalar correction field. This method will enforce $\nabla \bullet \mathbf{B} = 0$, in a discrete sense, within machine accuracy given certain conditions are met (Ref. [54]).

A unique spatial discretization scheme was developed (Ref. [55]) that exploits the Gauss' divergence theorem to automatically enforce $\nabla \bullet \mathbf{B} = 0$ within machine accuracy at every time-step. This method does not require the solution of a Poisson equation but is subject to time-marching restrictions associated with magnetic diffusion, which can be prohibitively strict. This method is practical, and many astrophysical MHD flow studies utilize this technique, where the flow is compressible and magnetic diffusion is *negligible*— rather than dominant as in our case.

A hyperbolic-parabolic hybrid correction procedure was proposed by Ref. [56]. In these cases, the $\phi$ is transported with different wave speeds and can be solved using explicit time-marching, alleviating expensive matrix inversions. A Courant-Friedrichs-Lewy (CFL)-type time-marching restriction limits this approach, however.

### 1.2.8 Plasma disruptions

A significant concern of plasma disruptions is that they can cause unacceptable damage to the reactor itself due to EM forces. Therefore, many studies performed analyzed eddy and halo currents to compute forces on solid components in the structure. No studies that focused on LM MHD effects that occur during plasma disruptions were found in the literature. A comparison of eddy current codes, developed by groups around the world, was discussed in Ref. [57].

Criteria of when tokamak disruption predictions and their destructive effects are discussed in Ref. [58]. They used a theoretical and numerical approach to provide plasma disruption avoidance guidelines and estimation effects. One difficulty is that the physics have a broad range of certainty, which should affect the solution strategy. They suggest that numerical codes should disentangle the physics, but also point out that the resource demands to resolve the broad range in timescales are too high.

Electromagnetic loads, due to eddy and halo currents, were computed (Ref. [3]) in ITER blanket module designs. Calculations were performed using the Opera-3D software. Disruption events were modeled using the DINA code. Eddy and halo currents were computed using separate techniques. Radial torques, the largest torque component, are plotted as a function of time for different components and different types of disruptions. Fundamental contributions to the EM loads on several blanket module components were identified and discussed.

## 1.3 Objectives and scope

The primary objective of this work is to address LM MHD flow physics in the presence of strongly unsteady applied magnetic fields, akin to unsteady plasma events. To do this, we defined our secondary and tertiary objectives as stepping stones to our primary goal. Our second objective is to develop a numerical methodology and code to model MHD flows at moderate $Re_m$ and use this code to study moderate $Re_m$ MHD flows. Also, magnetic BCs for moderate $Re_m$ MHD flows is non-trivial and requires special care. At moderate $Re_m$, electric currents stay trapped within the conductor while the magnetic field can penetrate into the air (or vacuum) and naturally decay to zero far away. RV BCs are notoriously difficult to enforce, therefore PV BCs, despite controversy over their suitability at moderate $Re_m$, are still widely used. Therefore, our third objective is to compare approximate PV and RV magnetic BCs as a function in terms of the energy budget.

We developed a code, magnetohydrodynamic object-oriented numerical solver (MOONS), that uses the induced magnetic field as the main EM variable to relax the low $Re_m$ assumption. We have successfully benchmarked MOONS for several hydrodynamic LDC flows, low $Re_m$ MHD LDC and duct flows and moderate $Re_m$ MHD channel flows. We have addressed objectives one and two by simulating LDC MHD flows with a transversely applied magnetic field using both RV and PV magnetic BCs. For our primary objective, we consider a simplified geometry, a long rectangular enclosure, with an unsteady applied magnetic field computed from a plasma code (DINA), used for plasma disruptions in the ITER.

# CHAPTER 2

# Physical and Mathematical Model

## 2.1 Governing equations

We consider a total domain ($\Omega_t$) composed of a conducting fluid ($\Omega_f$), conducting solid wall ($\Omega_w$) and vacuum ($\Omega_v$) domains. Let $\Omega_c, \Gamma_f, \Gamma_c$, and $\Gamma_t$ denote the conducting domain (including both $\Omega_f$ and $\Omega_w$) and fluid, conductor and total boundaries respectively (Fig. 2.1).

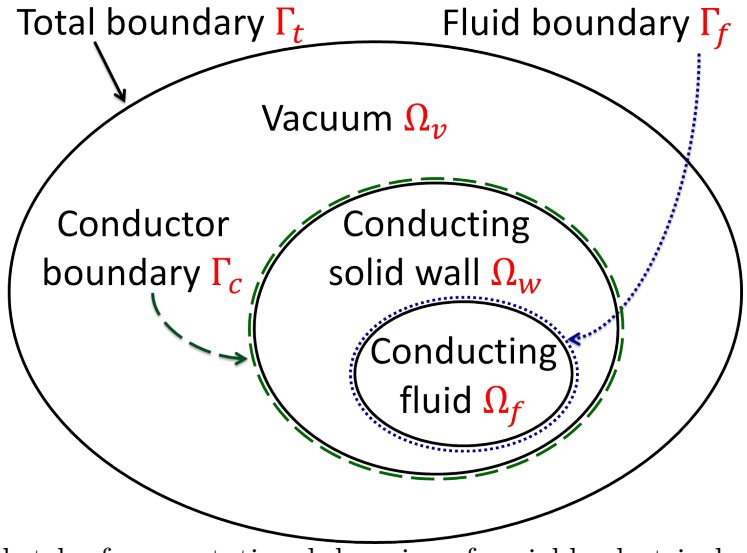


Figure 2.1: Sketch of computational domains of variable electrical conductivity.

The dimensional equations governing the flow of electrically conducting and incompressible fluid of uniform material properties, except electrical conductivity, are:

$$\rho_l \left[ \frac{\partial \mathbf{u}^\dagger}{\partial t^\dagger} + (\mathbf{u}^\dagger \bullet \nabla)\mathbf{u}^\dagger \right] = \mu_l \nabla^2 \mathbf{u}^\dagger - \nabla p^\dagger + \mathbf{j}^\dagger \times \mathbf{B}^\dagger, \quad \text{in } \Omega_f, \tag{2.1}$$

$$\mathbf{j}^\dagger = \frac{1}{\mu_{ml}} \nabla \times \mathbf{B}^\dagger, \quad \text{in } \Omega_c, \tag{2.2}$$

$$\frac{\partial \mathbf{B}^\dagger}{\partial t^\dagger} + \frac{1}{\mu_{ml}} \nabla \times \left[ \frac{1}{\sigma} \nabla \times \mathbf{B}^\dagger \right] = \nabla \times (\mathbf{u}^\dagger \times \mathbf{B}^\dagger), \quad \text{in } \Omega_t, \tag{2.3}$$

$$\nabla \bullet \mathbf{u}^\dagger = 0, \quad \text{in } \Omega_f, \tag{2.4}$$

$$\nabla \bullet \mathbf{B}^\dagger = 0, \quad \text{in } \Omega_t. \tag{2.5}$$

Here, $\mathbf{u}^\dagger$, $\mathbf{B}^\dagger$, $\mathbf{j}^\dagger$, $p^\dagger$, $t^\dagger$, $\rho_l$, $\mu_l$, $\mu_{ml}$, $\sigma$ are the dimensional velocity, total magnetic field, electric current density, pressure, time, liquid density, dynamic viscosity, magnetic permeability, and local electrical conductivity respectively. Equations (2.4) and (2.5) are constraints on Eqs. (2.1) and (2.3) respectively, which enforce mass and magnetic flux conservation.

Using length $L$, velocity $U$, time $L/U$, pressure $\rho_l U^2$, magnetic field $B^0$ and electric current density $\sigma_l U B^0$ for scales, the governing fluid flow equations can be transformed into a dimensionless form. Using these defined scales, the dimensionless incompressible and isothermal momentum, induction, mass continuity and magnetic field continuity equations for uniform material properties (except electrical conductivity) are:

$$\frac{\partial \mathbf{u}}{\partial t} + (\mathbf{u} \bullet \nabla)\mathbf{u} + \nabla p = \frac{1}{Re} \nabla^2 \mathbf{u} + \frac{Ha^2}{Re} \mathbf{j} \times \mathbf{B}, \quad \text{in } \Omega_f, \tag{2.6}$$

$$\mathbf{j} = \frac{1}{Re_m} \nabla \times \mathbf{B}, \quad \text{in } \Omega_c, \tag{2.7}$$

$$\frac{\partial \mathbf{B}}{\partial t} + Re_m^{-1} \nabla \times \left( \frac{1}{\overline{\sigma}} \nabla \times \mathbf{B} \right) = \nabla \times \mathbf{u} \times \mathbf{B}, \quad \text{in } \Omega_t, \tag{2.8}$$

$$\nabla \bullet \mathbf{u} = 0, \quad \text{in } \Omega_f, \tag{2.9}$$

$$\nabla \bullet \mathbf{B} = 0, \quad \text{in } \Omega_t. \tag{2.10}$$

Here, $\mathbf{u}$, $\mathbf{B} = \mathbf{B}^0 + \mathbf{B}^1$, $\mathbf{j}$, $p$ are dimensionless velocity, total magnetic field (composed of the

applied and induced field), electric current density, and pressure respectively. The Reynolds number ($Re$), Hartmann number ($Ha$), magnetic Reynolds number ($Re_m$), and dimensionless ratios of electrical conductivity are defined as

$$Re = \frac{UL}{\nu_l}, \qquad Ha = B^0 L\sqrt{\frac{\sigma_l}{\rho_l \nu_l}}, \qquad Re_m = \mu_{ml}\sigma_l UL, \qquad \overline{\sigma} = \frac{\sigma}{\sigma_l}.$$

Here, $\nu_l$ is the kinematic viscosity of the liquid. As mentioned, the $Re$, $Ha^2$ and $Re_m$ estimate the ratio of inertial to viscous forces, electromagnetic to viscous forces and magnetic field convection to diffusion respectively. Additional convenient dimensionless parameters may be defined from combinations of those above. They are:

$$N = \frac{Ha^2}{Re} = \frac{\sigma_l B^{0^2} L}{\rho_l U}, \qquad Al = \frac{N}{Re_m} = \frac{B^{0^2}}{\rho_l \mu_{ml} U^2}.$$

Here, $N$ and $Al$ are the interaction and Alfven numbers respectively. The interaction number estimates the ratio of EM to inertial forces and Alfven number estimates the ratio of magnetic to kinetic energies.

There is no guarantee that Eq. (2.10) will be satisfied when integrating Eq. (2.8), especially over long periods. Mathematically, Eq. (2.10) does not need to be satisfied when solving Eq. (2.8); however, this may lead to unphysical forces in the momentum equation (Ref. [59, 53]). Several methods can be used to enforce Eq. (2.8) and will be discussed in § (3.1.2.1) and (3.1.2).

### 2.1.1 Discussion of dimensionless parameters

Non-dimensionalization minimizes the number of parameters to define a given flow uniquely. The emergent dimensionless parameters are very useful when characterizing and comparing flows. In hydrodynamic flows, low $Re$ are typically laminar and smooth, whereas high $Re$ flows are typically turbulent and chaotic. In low $Re_m$ MHD flows, $Ha$ can drastically change the flow features and even laminarize flows. Increasing $Re_m$ for such flows results in increased convection of the induced magnetic field and can again change the flow regime. Increasing $Re_m$ above a critical limit can result in the dynamo-type physics.

The concept of boundary layers (BLs) dramatically impacted the field of fluid dynamics. BLs in purely hydrodynamic flows are thin regions near solid objects (e.g., walls or flow obstacles) where viscous forces dominate. The proportion of the largest flow scales to the BL scale is generally related to the Reynolds number. The BL is also useful in determining the required resolution needed to resolve the physically important scales in the flow. In low $Re_m$ MHD flows, additional BLs can form, called Hartmann layers. For moderate $Re_m$ MHD flows, there is an additional BL, the magnetic BL, that plays a role in determining the flow regime. The dimensionless momentum, Hartmann, and magnetic BLs are rough estimates:

$$\begin{aligned} \frac{\delta}{L} &\sim Re^{-1/2}, \quad \text{Momentum boundary layer} \\ \frac{\delta_{Ha}}{L_{||}} &\sim \frac{1}{Ha}, \quad \text{Hartmann boundary layer} \\ \frac{\delta_m}{L} &\sim Re_m^{-1/2}, \quad \text{Magnetic boundary layer} \end{aligned} \tag{2.11}$$

Here, $L_{||}$ is the characteristic length scale parallel to the magnetic field. In low $Re_m$ MHD flows, the viscous to Hartmann BL ratio, $Ha/Re^{1/2}$, is an important flow characterizing parameter that estimates the onset of laminarization and two-dimensionalization (see Ref. [60]). There are many more flow regimes in moderate $Re_m$ flows because more possible combinations of $\delta$, $\delta_{Ha}$ and $\delta_m$ ratios exist. The magnetic field is organized in length scales $L$ while electric current occupies the magnetic BL (Ref. [1]). The square of viscous to magnetic BL ratio, $Re_m/Re$ (Prandtl number), influences the critical $Re_m$ at which self-generated magnetic field occur (see Ref. [61]).

The concept of timescales is also very useful. The proportion of the physical timescale to the characteristic timescale is generally related to the dimensionless parameters. The dimensionless convective, diffusive, Hartmann damping, and magnetic diffusion times can

be roughly estimated by:

$$\begin{aligned} \frac{t_\nu}{t_c} &\sim Re, && \text{Momentum diffusive time} \\ \frac{t_j}{t_c} &\sim Re/Ha^2, && \text{Hartmann damping time} \\ \frac{t_m}{t_c} &\sim Re_m, && \text{Magnetic diffusion time} \end{aligned} \tag{2.12}$$

Here, $t_c = L/U$ is the convective timescale. Being that this study is focused on the magnetic Reynolds number, the magnetic diffusion time is of most interest to us. The effect of increasing $t_m$, by increasing $Re_m$, was observed in our study (see § 5.2.1) and agrees with trends observed in kinematic MHD studies at $Re_m = 1000$ by Ref. [15].

### 2.1.2 Magnetic induction equation in vacuum

Equation (2.8) is valid everywhere in space, but inspecting how it simplifies in the vacuum is insightful. In the vacuum, Eq. (2.8) may be written in the following form

$$\nabla \times (\nabla \times \mathbf{B}) = \mathbf{0} \qquad \text{in } \Omega_v. \tag{2.13}$$

The convection term has vanished because $\mathbf{u} = \mathbf{0}$ and the unsteady term has vanished because $\overline{\sigma}_v$ ($\overline{\sigma}$ in $\Omega_v$) is zero, resulting in the absence of $Re_m$. The absence of the unsteady term implies that the magnetic field travels infinitely fast in vacuum. This equation may be cast into the form of a Poisson equation, which is more convenient for solving, using the vector identity $\nabla \times \nabla \times \mathbf{B} = \nabla(\nabla \bullet \mathbf{B}) - \nabla^2\mathbf{B}$ and the divergence-free constraint, such that:

$$\nabla^2\mathbf{B} = \mathbf{0} \qquad \text{in } \Omega_v. \tag{2.14}$$

Electric currents are not permitted in the vacuum, and while the magnetic field permeates into the vacuum, its strength decreases with distance from the conductor. Providing that the electric current is known, the magnetic field at any point in space can be computed using the Biot-Savart law (Ref. [62]). The Biot-Savart law can be written, using the scales defined

in this study, as:

$$\mathbf{B}(\mathbf{x}) = \frac{Re_m}{4\pi} \int_{\Omega_c} \mathbf{j}(\mathbf{x}') \times \frac{\mathbf{r}}{|\mathbf{r}|^3} d^3\mathbf{x}', \quad \mathbf{r} = \mathbf{x} - \mathbf{x}'. \tag{2.15}$$

Here, $\mathbf{x}, \mathbf{x}', \mathbf{r}$ are the dimensionless spatial coordinate vector, dummy variable for integration and distance vector from $\mathbf{x}$ to $\mathbf{x}'$ respectively. According to Eq. (2.15), the magnetic field strength decreases with $1/|\mathbf{r}|^3$ in the vacuum domain. This is a useful result to help determine the size of a sufficiently large vacuum domain that such the magnetic field approximately satisfies $\mathbf{B} = \mathbf{0}$ naturally.

## 2.2 Magnetic boundary conditions

### 2.2.1 Real vacuum boundary conditions

The most physically reliable, and widely applicable, magnetic BCs are:

$$\mathbf{B} = \mathbf{0}, \qquad \text{at } \Gamma \to \infty. \tag{2.16}$$

We refer to these BCs as "real-vacuum" (RV) in homage to the commonly phrased "pseudo-vacuum" magnetic BCs. To simulate MHD flows using RV BCs in general geometric domains is a formidable task because they are non-local BCs and require special care. Several tactics have been used over the years to apply RV BCs. Several are discussed here.

For simple geometries, these BCs can be applied analytically using poloidal-toroidal decomposition (Ref. [63]) and spherical harmonics (Ref. [31]). For non-simple geometries, we discuss three typical methods. They are, simulate $\mathbf{B}$ in the vacuum and apply $\mathbf{B} = \mathbf{0}$ far from $\Omega_c$ using 1) continuous equations and 2) separate equations and apply an iterative matching condition and 3) BEM formulation.

Method one: $\mathbf{B} = \mathbf{0}$ far with continuous equations. In practice, Eq. (2.16) is applied at a moderate distance sufficiently far from the conductor to resolve the magnetic field decay in the vacuum accurately. For example, Ref. [64] demonstrated that truncation errors reduce to less than $\frac{1}{2}\%$ for a $\Omega_v$ five times larger than the $\Omega_c$. There are several advantages and disadvantages to this method. The first advantage is that the implementation is simple.

Only one equation must be solved in a continuous domain at each time-step, as opposed to method two where multiple and separate equations must be solved in separate domains (and iteratively matched) at each time-step. Second, sophisticated numerical methods (e.g., multigrid, conjugate gradient (CG)) can be applied to solve the continuous equations. The first disadvantage is that a prohibitive time-step restriction must be satisfied to treat magnetic field diffusion explicitly, so it must be treated implicitly. A consequence of implicit magnetic field diffusion treatment is that Eq. (2.10) is not naturally satisfied and therefore requires a correction procedure be used. Also, the magnetic diffusion operator for variable $\overline{\sigma}$ is complicated. Second, $\overline{\sigma}$ in $\Omega_v$ cannot be set to zero exactly, because it appears in the denominator in Eq. (2.8), therefore a sufficiently small $\overline{\sigma}$ in vacuum must be determined to prevent electrical current density from leaving $\Omega_c$ and entering $\Omega_v$ such that the solution $(\mathbf{u}, \mathbf{B})$ stops changing. Finding a sufficiently small $\overline{\sigma}$ is a difficult task because Eq. (2.8) becomes more poorly conditioned as $\overline{\sigma}$ becomes more discontinuous across $\Gamma_c$.

Method two: $\mathbf{B} = \mathbf{0}$ far with separate equations. This method is nearly the same as method one; however, uniform properties are used in Eqs. (2.6) and (2.8), and they are solved in $\Omega_c$ and $\Omega_v$ separately and match the conditions at $\Gamma_c$ between the domains. In particular, the magnetic field in the vacuum can be solved using Eq. (2.13) or (2.14). An iterative procedure must be used to ensure that fluxes between the $\Omega_c$ and $\Omega_v$ are consistent. There are several advantages and disadvantages of this method. The first advantage is that the electrical conductivity of $\Omega_v$ can be set to zero exactly; this is not possible in method one. Second, sophisticated numerical methods (e.g., multigrid, CG) can be applied to solve the equations in each domain. Third, the condition number of the induction equations (in $\Omega_v$ and $\Omega_c$) are not increased due to highly discontinuous $\overline{\sigma}$ across $\Gamma_c$. The first disadvantage of this method is that it adds programmatic complexity because domains must be decomposed spatially *and* by the equations solved. This disadvantage is more of a technical issue than one of the increased computational efforts. Second, this flux matching process must be performed iteratively, and the convergence of this process may not compensate the gain from more favorable condition numbers in the induction equations.

Method three: Near-Field Boundary Condition Formulation. It is possible to formulate magnetic BCs at the conductor boundary when the magnetic field in vacuum is of no interest. This formulation, while elegant and does not require extending the computational domain, requires the solution of a dense and non-symmetric partial integro-differential equation on the conductor boundary—i.e., it is very complicated. This complex set of equations can be solved, e.g., using BEM on general geometric domains (see Refs. [36, 46, 47]). Alternative BCs have been developed to approximate RV BCs and circumvent many of the difficulties mentioned above.

### 2.2.2 Pseudo vacuum boundary conditions

Pseudo-vacuum BCs, which force magnetic field lines perpendicular to the conductor boundary, are an approximation to RV BCs and are accurate when $Re_m << 1$. They are mathematically represented as:

$$(\mathbf{n} \bullet \nabla)(\mathbf{B} \bullet \mathbf{n}) = 0, \qquad \mathbf{n} \times \mathbf{B} = \mathbf{0}, \qquad \text{at } \Gamma = \Gamma_c. \tag{2.17}$$

It is noteworthy that Eq. (2.17) is a particular case of ensuring $\nabla \bullet \mathbf{B} = 0$ at the boundary and that they are physically justified when dealing with ferromagnetic materials, where the magnetic permeability dramatically changes across the boundary (Ref. [48]). PV BCs have been used for many years and, although no MHD flows in nature occur at $Re_m = 0$ exactly, a wide range of MHD flows have been successfully described using PV BCs (see, e.g., Refs. [65, 45, 48]). The first, obvious advantage of PV BCs is that the large computational domain associated with RV BCs is truncated to $\Omega_c$ only. The second advantage is that the elliptic behavior of $\mathbf{B}$ in $\Omega_v$, resulting in $\mathbf{B}$ at every point on $\Gamma_c$ depending on $\mathbf{B}$ at every other point on $\Gamma_c$, and its drastic difference in timescale due to the parabolic behavior of $\mathbf{B}$ in $\Omega_c$ is resolved. Also, this approximation enforces electric current ($\mathbf{j}$) insulation on the boundary ($\mathbf{j} \bullet \mathbf{n} = 0$), which is attractive for applications. The disadvantages of PV BCs is that, while it is equivalent to RV BCs when $Re_m << 1$, it forces $\mathbf{n} \times \mathbf{B} = \mathbf{0}$, which is not valid in the case of moderate $Re_m$ and may be especially problematic for large $Re_m$.

PV BCs have been used extensively for low $Re_m$ MHD studies, but are not valid for moderate $Re_m$ MHD flows and their accuracy in moderate $Re_m$ MHD flows has not yet been studied. These magnetic BCs can be easily applied in the context of the **B** and **j** formulations (Ref. [17]).

### 2.2.3 Thin wall boundary conditions

Thin wall magnetic BCs, applied at the *fluid* boundary, allow electric currents to exit the fluid domain by an amount controlled by a parameter called wall conductance ratio ($c_w$). They are mathematically expressed as:

$$(\mathbf{n} \bullet \nabla)(\mathbf{B} \bullet \mathbf{n}) = 0, \qquad \mathbf{n} \times \mathbf{B} + c_w^{-1}(\mathbf{n} \bullet \nabla)(\mathbf{n} \times \mathbf{B}) = \mathbf{0}, \qquad \text{at } \Gamma = \Gamma_f. \tag{2.18}$$

The $c_w$ appears in the thin wall BC equations and roughly estimates the ratio of electric currents in the wall to the Hartmann layer. If $c_w = 0$, then the walls are electrically insulating. thin wall (TW) BCs are based on the assumption that currents in the wall are approximately uniform and has the advantage of further truncating the computational domain, compared to PV BCs.

### 2.2.4 Decay function boundary conditions

The last BC we discuss is that of a decay function approximation. The idea of this BC is to strike a balance between the RV and PV BCs at some finite distance, but not as far, from the conductor:

$$\mathbf{B} \sim \mathbf{r}^{-n}, \qquad \text{at } \Gamma = \Gamma_*. \tag{2.19}$$

Here, $\mathbf{r}, n, \Gamma_*$ is a position vector, a tuning parameter to estimate the decaying order of **B** from the conductor, and the location that the boundary condition is applied. While this approach is attractive in that it does not require as large a computational domain as RV BCs, virtually no exploitable information is known at the location that this BC is applied.

## 2.3 Computational challenges

Several numerical challenges were faced when developing a suitable numerical methodology. Almost all of the difficulties were entangled and had to be addressed simultaneously.

### 2.3.1 Enforcing $\nabla \bullet \mathbf{B} = 0$

The first challenge involved enforcing Eq. (2.10), an important constraint in the MHD equations (Ref. [53]). This constraint is not naturally satisfied and therefore requires special treatment. First, the constrained transport (CT) method was adopted because it enforces Eq. (2.10) within machine accuracy at every time-step if Eq. (2.10) is satisfied initially and are compatible with the boundary conditions. This method is consistent with PV BCs, which automatically enforces Eq. (2.10) on the boundary, but RV BCs will only be compatible with the CT method (enforce Eq. (2.10)) if the magnetic field happens to also satisfy $\partial_n B_n = 0$ at the boundary. The drawback of the CT method, however, is that it relies on explicit time-marching (Ref. [54]), which is computationally inefficient for solving diffusion dominant (elliptic) equations. Therefore, implicit time-marching was adopted. The drawback of using an implicit scheme, however, is that Eq. (2.10) is not automatically satisfied. Ref. [53] suggested a projection method be used to enforce Eq. (2.10). This method involves solving a Poisson equation (elliptic), akin to the projection method used to enforce $\nabla \bullet \mathbf{u} = 0$. Recent methods have been suggested (Ref. [56]) to use a hyperbolic-parabolic hybrid correction procedures to enforce Eq. (2.10) for high $Re_m$ MHD flows.

### 2.3.2 Applying real vacuum boundary conditions

The second challenge was applying proper magnetic BCs. The computational domain must be very large to both apply RV BCs and have sufficient resolution to resolve Hartman layers, resulting in a vast range of length scales. Furthermore, the low $\overline{\sigma}_v$ results in the nearly elliptic behavior of $\mathbf{B}$ in the vacuum, leading to a broad range of timescales. Strongly stretched grids and discontinuous $\overline{\sigma}$ increases the condition number of the diffusion operator in the

magnetic induction equation. RV BCs are not strictly compatible with specific numerical methods. For example, when using the CT method with RV BCs, electric currents can exit the computational domain, resulting in growth of $\nabla \bullet \mathbf{B}$. The allowable growth of $\nabla \bullet \mathbf{B}$ when using RV BCs is because these BCs are not strictly compatible with the Eq. (2.10). If the domain is sufficiently large, and the boundaries separated by sufficiently insulating vacuum, then the magnetic field will decay enough to satisfy both $\mathbf{B} = \mathbf{0}$ and $\partial_n B_n = 0$. Similarly, $\mathbf{B} = \mathbf{0}$ is a particular case of PV BCs when they are applied sufficiently far from the conducting domain— when *both* BCs are satisfied.

### 2.3.3 Challenges with low and variable $\overline{\sigma}$

. The third challenge was dealing with low and variable $\overline{\sigma}$. The use of implicit schemes is necessary when explicit time-marching prohibitively restricts $\Delta t$, which occurs for low $\overline{\sigma}$, low $Re_m$ and fine grids. A consequence of the implicit scheme is that $\nabla \bullet \mathbf{B}$ growth is not prevented (especially when $\overline{\sigma}$ varies), so an additional Poisson equation must be solved to enforce Eq. (2.10). Furthermore, the diffusion operator is a complicated matrix for non-uniform grids, staggered $\mathbf{B}$ and variable $\overline{\sigma}$ (see Fig. 2.2) with *slanted* diagonals.

It is worth noting that the diffusion operator is not symmetric if $\mathbf{B}$ is collocated at the computational cell centers. The symmetry of the diffusion operator affects which the applicability of numerical algorithms that can be applied. For example, the CG method is derived assuming $A$ in $Ax = b$ is symmetric. Due to low $\overline{\sigma}_v$ requirements, we adopted an implicit scheme. A matrix-free preconditioned conjugate gradient (PCG) was implemented, using diagonal preconditioning, to solve the induction equation. A diagonal preconditioner was used to improve the condition number.

### 2.3.4 Determining a sufficiently large computational domain size

The fourth challenge was to answer: How large should the computational domain be for the magnetic field to sufficiently decay to zero? To address this, we adopted the computational domain size, $\Omega_t \sim 5\Omega_c$, suggested by Ref. [64]. They solved 2D MHD equations using

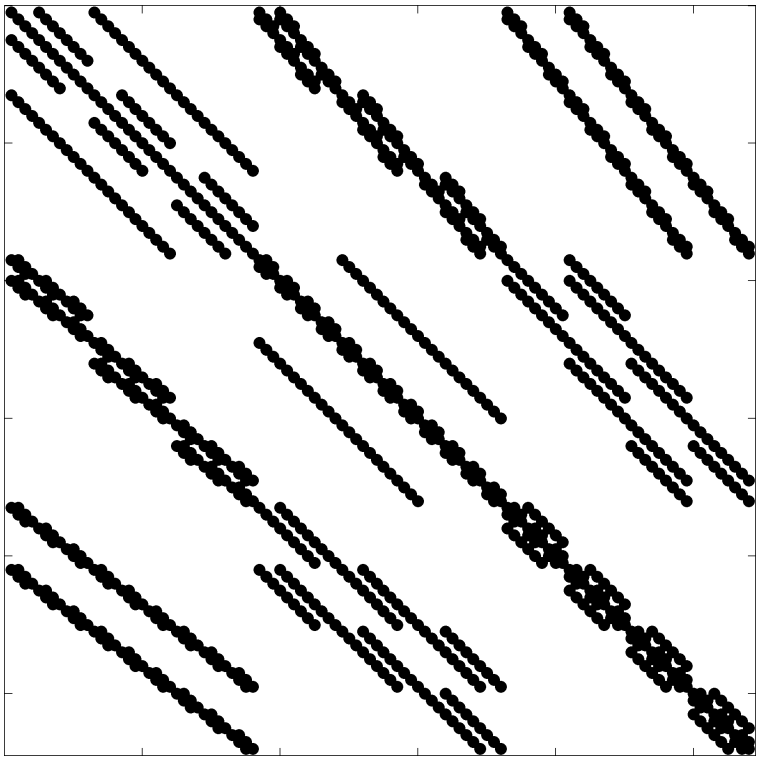

Figure 2.2: Non-zeros of matrix structure for curl-curl operator, when solved implicitly, for staggered $\mathbf{B}$, variable $\overline{\sigma}$ and mesh $N_{cells} = (3, 3, 3)$.

the B-formulation in conducting and perfectly insulating domains. The change in electrical conductivity was addressed separately by using an iterative matching condition.

### 2.3.5 Determining a sufficiently small vacuum $\overline{\sigma}$ value

The fifth challenge was to answer: At what $\overline{\sigma}_v$ does the solution stop changing? As the $\overline{\sigma}_v$ decreases, the computational difficulty increases. This challenge most significantly motivated the change in use of the CT method, which used explicit time-marching, to the diffusion-implicit time-marching method to simulate highly insulating domains. The most insulating $\overline{\sigma}_v$ used would have taken several years to finish using explicit time-marching. To address this, a diffusion-implicit time-marching scheme was adopted. What was found, ultimately, was that we could use $\overline{\sigma}_v = 10^{-3}$ by simulating several LDC MHD flows with decreasing $\overline{\sigma}_v$. We monitored the induced magnetic field energy over time until the flow reached a steady-state and compared changes in the induced magnetic field with respect to changes in

$\overline{\sigma}_v = 10^{-3}$.

# CHAPTER 3

# Code Development

## 3.1 Numerical methodology

### 3.1.1 Spatial discretization

A non-uniform rectilinear grid is adopted (Ref. [66]) to ensure a sufficient number of points in the BL, including the Hartmann layer at the cavity walls perpendicular to the applied magnetic field and the side layer at the walls parallel to the magnetic field and to efficiently address the large computational domain. Each variable is approximated on a fully staggered mesh system as shown in Fig. 3.1. Velocity and magnetic fields are staggered on the face of the computational cell to avoid checkerboard-type instabilities and to enforce flux conservation. The electric current and electrical conductivity are located at the computational cell edges. Pressure is located in the center of the computational cell. Second-order spatial accuracy is applied to approximate derivatives using central finite difference schemes and to compute the interpolations between different meshes.

Derivatives are computed in the following systematic way. The derivative of a field, positioned on a given location on the computational cell, is always calculated from neighboring data. The result is that a field and its first derivative are never collocated [see Table (3.1)]. The same type of rule is followed with interpolations along the x,y and z directions. Ghost points are used as a means to enforce BCs and allow derivative and interpolation operators to behave equivalently in the domain interior as they do in the domain boundaries, which provides operators with beneficial commutative properties (Ref. [67]). Unknowns are decomposed into interior and boundary values. Second order boundary treatment is recovered from first order derivative stencils by adding the remaining derivative stencils, required to recover 2nd-order accuracy, to the right-hand side of the equation (where all source terms

are known).

| **Location of input scalar field** $(f)$ | **Location of output vector field** $\{\partial_x f, \partial_y f, \partial_z f\}$ |
|---|---|
| cell center | {x-face,y-face,z-face} |
| cell corner | {x-edge,y-edge,z-edge} |
| x-face | {cell center,z-edge,y-edge} |
| y-face | {z-edge,cell center,x-edge} |
| z-face | {y-edge,x-edge,cell center} |
| x-edge | {cell corner,z-face,y-face} |
| y-edge | {z-face,cell corner,x-face} |
| z-edge | {y-face,x-face,cell corner} |

Table 3.1: Locations of input scalar fields and output derivatives when computed on the staggered computational cell.

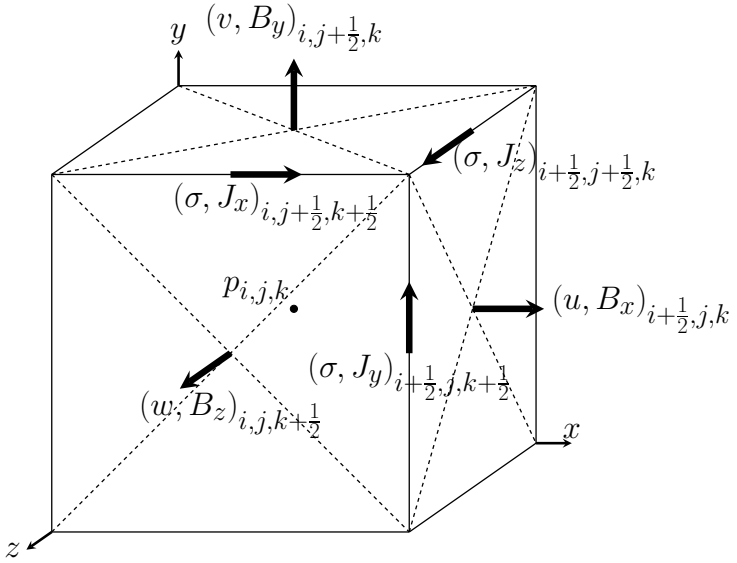


Figure 3.1: Staggered variables on computational cell.

The momentum and induction equations are computed on the computational cell face, while the pressure and correction equations [discussed in § (3.1.3.1)] are computed on the computational cell center. Computations were performed using staggered and collocated grids. The following general rules were found to produce consistent results between the staggered and collocated grid configurations. First, the number of interpolations performed to compute terms is minimized— interpolations are only performed when necessary. Second,

interpolations are performed such that terms naturally land on the location of the governing equation. For example, the advection term in the induction equation is calculated as follows: 1) The velocity and magnetic fields are interpolated from the cell face to the cell edges 2) $\mathbf{u} \times \mathbf{B}$ is then computed on the cell edge and 3) the curl of $\mathbf{u} \times \mathbf{B}$ is computed from the cell edges, the result of which is naturally located on the cell face (where the induction equation is computed).

### 3.1.2 Correction procedure to assure $\nabla \bullet \mathbf{B} = 0$

Enforcing Eq. (2.10) can be accomplished using one of several techniques. Two such methods, the CT and projection methods, are discussed here. The projection method enforces Eq. (2.10) by estimating a solution and then "projecting" the estimate onto a divergence-free space.

A projection method was first proposed to enforce Eq. (2.10) (Ref. [53]) to avoid unphysical forces in the momentum equation. One advantage of this approach is its insensitivity to initial and BCs, so long the BCs satisfy the magnetic compatibility constraint. The difficulty is that it requires the solution of a Poisson equation for a scalar field $\phi$. The procedure is outlined mathematically as:

$$\begin{aligned} \nabla^2 \phi^{n+1} &= \nabla \bullet \mathbf{B}^*, \\ \mathbf{B}^{n+1} &= \mathbf{B}^* - \nabla \phi^{n+1}. \end{aligned} \tag{3.1}$$

Here, $\phi, \mathbf{B}^*$ are the correction scalar field and intermediate magnetic field, which may not necessarily satisfy Eq. (2.10). This method will enforce Eq. (2.10) within machine accuracy of $\mathbf{B}^{n+1}$ so long the Laplacian operator is computed using the same discrete operators as the gradient operator in the correction step and the divergence of the magnetic field. These conditions and discussions about direct vs. iterative solvers are well discussed in Ref. [54].

Dirichlet BCs are typically used for $\phi$ (e.g., $\phi|_{\Gamma_t} = 0$) so that the magnetic field can be adjusted on the boundaries to satisfy the magnetic compatibility constraint:

$$\int_{\Gamma_t} \mathbf{B} \bullet \mathbf{n} dA = 0. \tag{3.2}$$

Here, the integral is computed over the magnetic boundary $\Gamma_t$, which is simply a global statement of magnetic flux conservation.

The projection method relieves the diffusion-explicit time-step restriction with time-implicit diffusion treatment and is insensitive to initial $\nabla \bullet \mathbf{B}$ conditions. While the projection method requires matrix inversion, due to implicit diffusion treatment, its computational efficiency was found to be superior to the CT method in most cases. Therefore the projection method was used for all computations in the present research. Both method formulations are discussed in more detail below.

#### 3.1.2.1 An explicit method using Constrained Transport method

The CT method, initially proposed by Ref. [68], prevents the growth of $\nabla \bullet \mathbf{B}$ intrinsically through a staggered variable conservation scheme (a thorough review is given in Ref. [59]). In this discretization, the electric field, magnetic field, and electric current are staggered on the computational cell edge, face and edge respectively. A simple proof of how the CT method enforces $\nabla \bullet \mathbf{B} = 0$ can be derived by writing Faraday's law, using the mentioned spatial discretization, and updating the magnetic field in time (see § (4.1) in Ref. [59]). This derivation reveals a perfect cancellation in the discrete form of $\nabla \bullet \mathbf{B}$. This scheme relies on diffusion-explicit treatment, limiting the time-step as mentioned above. For the $Re_m$ range considered in the present work, the CT method was found to require a very small time-step, especially with the presence of an outer vacuum region.

The CT method ensures Eq. (2.10) within machine accuracy at each time-step ($\Delta t$) but requires that the magnetic BCs and initial magnetic field distribution are compatible with Eq. (2.10). The CT method is fast because it requires a single explicit time update, but suffers from a diffusion-explicit time-step restriction. This restriction becomes prohibitively severe for insulating domains, low $Re_m$ flows, and very fine grids.

### 3.1.3 Temporal discretization

Equations (2.6) and (2.8) are solved separately at each time-step. A $\theta$-implicit Crank-Nicholson-type method is used for the diffusion terms, a second order Adams-Bashforth method is used for the advection terms, and pressure is treated purely implicitly. The momentum and induction time-discretized equations, from time level $n$ to $n+1$ are:

$$\begin{aligned} \frac{\mathbf{u}^{n+1}-\mathbf{u}^{n}}{\Delta t} - \theta_u Re^{-1}\nabla^2\mathbf{u}^{n+1} &= -\nabla p^{n+1} + \frac{3}{2}\mathbf{K}^{n} - \frac{1}{2}\mathbf{K}^{n-1}, \\ \mathbf{K}^{n} &= (1-\theta_u)Re^{-1}\nabla^2\mathbf{u}^{n} + (\mathbf{u}^{n}\bullet\nabla)\mathbf{u}^{n} + \frac{Ha^2}{Re}\mathbf{j}^{n}\times\mathbf{B}^{n}, \end{aligned} \tag{3.3}$$

$$\begin{aligned} \frac{\mathbf{B}^{n+1}-\mathbf{B}^{n}}{\Delta t} + \theta_B Re_m^{-1}\nabla\times(\overline{\sigma}^{-1}\nabla\times\mathbf{B}^{n+1}) &= \frac{3}{2}\mathbf{T}^{n} - \frac{1}{2}\mathbf{T}^{n-1}, \\ \mathbf{T}^{n} &= -(1-\theta_B)Re_m^{-1}\nabla\times(\overline{\sigma}^{-1}\nabla\times\mathbf{B}^{n}) + \nabla\times(\mathbf{u}^{n}\times\mathbf{B}^{n}). \end{aligned} \tag{3.4}$$

Here, $\theta$ is a parameter that controls the degree of explicit-to-implicit treatment of the diffusion terms. Diffusion is treated purely explicitly, centered in time, and purely implicitly for $\theta = 0, 0.5, 1$ respectively. Equation (3.3) was demonstrated to be 2nd-order accurate in time Ref. [45]. Equations (3.3-3.4) closely resemble the time discretization used in Ref. [45].

#### 3.1.3.1 Fractional-step method

The fractional-step method, or more generally projection method, is a technique used to solve coupled equations—e.g., velocity and pressure—by decoupling them. The fractional-step method is common in CFD literature (see, e.g., Refs. [69, 70, 67, 45]) and was first proposed by Chorin in 1968 (see Ref. [71]).

A brief overview of how the fractional-step method is applied to Eqs. (3.3-3.4) and the resulting time-marching procedure is given here. The following discussion is similar to that in Ref. [67], except that the coupled MHD equations are considered here rather than the purely hydrodynamic equations. Therefore, in applying the projection method to the MHD equations, a new scalar field ($\xi$) is introduced to the induction equation to enforce magnetic field conservation.

Equations (3.3-3.4) can be exactly cast into matrix form. The matrix operator, which includes the diffusion terms and operates on the unknowns ($\mathbf{u}, \mathbf{B}, p$, and $\xi$), can be approximated with a 2nd-order time accurate approximation (see Ref. [67]). The advantage of applying this approximation is that the approximated matrix can be factorized, which permits the system of equations to be solved as a sequence of operations. Using discrete gradient ($G$), divergence ($D$), Laplacian ($\mathcal{L}$) and curl ($C$) operators, this sequence of operations may be written as:

$$\begin{aligned}\left(I - \Delta t \theta_u Re^{-1}\mathcal{L}\right)\hat{\mathbf{u}} = \mathbf{u}^n + \\ \Delta t\left(\frac{3}{2}\bar{\mathbf{K}}^n - \frac{1}{2}\bar{\mathbf{K}}^{n-1} + BC_1\right),\end{aligned} \tag{3.5}$$

$$\Delta t \mathcal{L}\zeta^{n+1} = D\hat{\mathbf{u}} - BC_2, \tag{3.6}$$

$$\mathbf{u}^{n+1} = \hat{\mathbf{u}} - \Delta t G\zeta^{n+1}, \tag{3.7}$$

$$\begin{aligned}\left(I + \Delta t \theta_B Re_m^{-1} C(\overline{\sigma}^{-1}C)\right)\hat{\mathbf{B}} = \mathbf{B}^n + \\ \Delta t\left(\frac{3}{2}\bar{\mathbf{T}}^n - \frac{1}{2}\bar{\mathbf{T}}^{n-1} + BC_3\right),\end{aligned} \tag{3.8}$$

$$\Delta t \mathcal{L}\xi^{n+1} = D\hat{\mathbf{B}} - BC_4, \tag{3.9}$$

$$\mathbf{B}^{n+1} = \hat{\mathbf{B}} - \Delta t G\xi^{n+1}. \tag{3.10}$$

Here, $I, \hat{\mathbf{u}}$, $\hat{\mathbf{B}}$, $\bar{\mathbf{K}}$, $\bar{\mathbf{T}}$, $BC_i, (i = 1, 2, 3, 4)$ are the identity matrix, intermediate fields for $\mathbf{u}$ and $\mathbf{B}$, spatially discrete forms of $\mathbf{K}$ and $\mathbf{T}$ in Eqs. (3.3) and (3.4), and BCs for $\mathbf{u}^{n+1}$, $p^{n+1}$, $\mathbf{B}^{n+1}$, $\xi^{n+1}$ respectively. The scalar field $\zeta$ enters the equations as a result of the time-splitting error, due to the previously mentioned matrix approximation, and relates to pressure via $p = \zeta - \theta_u \Delta t Re^{-1}\nabla^2\zeta$ (see Ref. [67]). The $p$-$\zeta$ relation holds only in the case that the gradient and Laplacian operators are commutative, which is valid for continuous operators but is not guaranteed for discrete operators. Note that there are no requirements for BCs on $\hat{\mathbf{u}}$ and $\hat{\mathbf{B}}$, since BCs for the unknowns have already been absorbed into $BC_i$, $i = 1, ..., 4$ (see Ref. [67]).

Our procedure in Eqs. (3.5-3.10) resembles the popular fractional-step method, proposed

by Ref. [69], applied to the incompressible momentum and solenoidal induction equations separately. A matrix-free diagonally-preconditioned CG method is used to iteratively solve Eqs. (3.5-3.10), using 20 iterations for Eqs. (3.5) and (3.8) and 5 iterations for Eqs. (3.6) and (3.9) at each time level respectively. If Eq. (3.8) is solved by a matrix inversion, then the matrix to be inverted has a complicated structure due to the non-uniform grid, variable electrical conductivity, and staggered magnetic field configuration, resulting in *slanted* non-zero elements (see Fig. 2.2). The advantages of the matrix-free method include ease of implementation and less memory consumption compared to storing the entire curl-curl operator. The disadvantage, however, is that the matrix-free method is less computationally efficient as storing the curl-curl operator— one test performed resulted in a $\sim 5\%$ difference in computational time.

Due to the stiffness in Eq. (3.8) and tests yielding faster and more stable computations for time-implicit diffusion treatment, $\theta_u = 1$, $\theta_u = 1$ and $\theta_B = 1$ were used exclusively in this study.

# CHAPTER 4

# Testing the Code

## 4.1 Hydrodynamic flows

A LDC flow is a standard benchmark for fluid dynamic codes due to the complex flow features including a transition to turbulence at high Reynolds numbers, development of vortex structures and singularities between the moving lid and the top walls.

This test was to address spatial order of accuracy as suggested in Refs. [72, 73]. A 3D LDC flow was simulated for grid resolutions $N_{cells} = \{32^3\}$, $\{64^3\}$, and $\{128^3\}$ in a domain size ($0 \leq x, y, z \leq 1$) for $Re = 400$. Neumann BCs were used for pressure, and all walls were stationary except the driven lid at $y = 1$. Solutions were compared on all coinciding cell corners of the coarsest grid. The spatial order of accuracy, $p$, and a parameter, $\alpha$ (estimates how far the solution is from the asymptotic range, Ref. [72]), were computed from

$$p = \frac{\ln \frac{|f^{h_3} - f^{h_2}|}{|f^{h_2} - f^{h_1}|}}{\ln(2)}, \quad \alpha = \frac{|f^{h_1}|}{|f^{h_2}|} \frac{|f^{h_3} - f^{h_2}|}{|f^{h_2} - f^{h_1}|}. \tag{4.1}$$

Here, $f^{h_1}$, $f^{h_2}$ and $f^{h_3}$ are solutions for finest $h_1$, moderate $h_2$ and coarsest $h_3$ grids respectively. The solution is in the asymptotic range when $\alpha/2^p$ is near unity. Spatial order of accuracy and $\alpha/2^p$ for $x$, $y$ and $z$ components of velocity were 1.72, 1.63, 1.85 and 1.0026, 1.021, 1.014 respectively using $L_2$ norms.

The computed values of $p$ and $\alpha/2^p$ are a good indication that the expected order of accuracy is being achieved and that results are in the asymptotic range respectively when taking singularities in the flow into consideration.

After confirming that the expected order of accuracy was achieved, further computations were performed for $Re = 400$ and $Re = 1000$ and compared with numerical data in Ref. [11].

From rest, both solutions reach a steady-state, and Fig. 4.1 shows an excellent match between numerical data for both $Re$. The match with numerical data demonstrates the versatility of MOONS because these two flows have different features. The large centralized vortex, and a second small vortex near $x = 1$ and $y = 0$, have different shapes for each $Re$ and a third vortex develops in the $x = 0$ and $y = 0$ corner for $Re = 1000$.

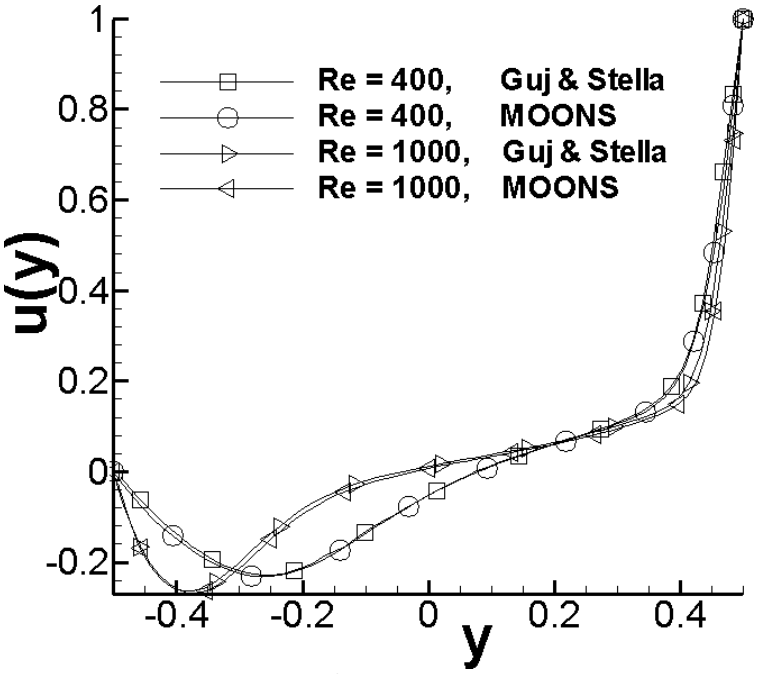


Figure 4.1: u-component velocity comparison in cavity center.

## 4.2 Low $Re_m$ MHD flows

Low $Re_m$ MHD flows are presented in this section for a LDC flow, conducting duct flow (Hunt, see Ref. [74]) and insulating duct flow (Shercliff, see Ref. [20]).

First, a 3D LDC MHD flow with a transversely applied magnetic field (Fig. 4.2) was simulated and compared with numerical data in Ref. [75] for $Re = 10$ and $Ha = 45$ in a domain size ($0 \leq x, y, z \leq 1$) with $N_{cells} = (64, 64, 64)$. The applied magnetic field, directed along the $z$-axis (Fig. 4.2), suppresses motion along its axis and, as a result, the flow tends to a 2D configuration in the $z$-plane except in the Hartmann layers near $z = 0$ and $z = 1$. The damping effect associated with the Hartmann layers results in more localized motion near

the moving lid (Fig. 4.3) and accelerates temporal flow development. Again, an excellent match is seen between numerical data and present computations in Fig. 4.3. Interestingly, high velocity and high magnetic field zones roughly coincide (Fig. 4.2).

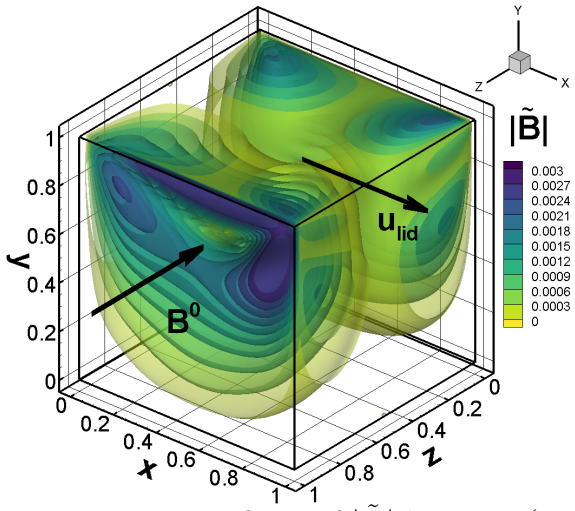


Figure 4.2: Iso-surfaces of $|\tilde{\mathbf{B}}|$ between ($0 \leq z \leq 0.94$) for a LDC flow.

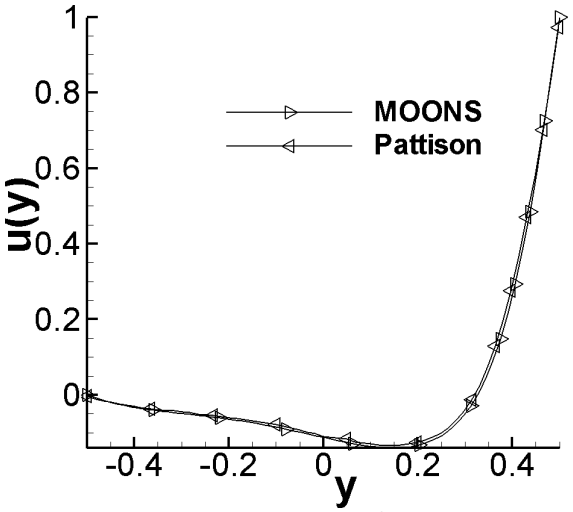


Figure 4.3: u-component velocity comparison in cavity center at $Re = 400$, $Ha = 45$.

Conducting and insulating duct MHD flows at low $Re_m$ were simulated for $Re = 10$ and $Ha = 500$ in a fully 3D geometry. These tests, among others, were suggested by Ref. [9] to validate MHD codes. A finite length duct was considered to simulate these fully developed flows. In the computations, the duct length was 40 with a cross-section of $2 \times 2$ and $N_{cells} = (45, 45, 45)$. The inlet and outlet velocity was uniform and fully developed respectively with no-slip walls. Neumann BCs were used for pressure. Hyperbolic tangent functions defined a transversely applied magnetic field with a uniform region of length 30 and fringes at $x = 5$ and $x = 35$ along the duct. In the case of Hunt's flow, the thickness of the Hartmann walls was 0.01, and the liquid and wall electrical conductivities were equal.

Expected flow characteristics are well captured in both flows. Thin Hartmann boundary layers are observed near the walls perpendicular to the magnetic field with nearly uniform core flow and side wall jets develop in Hunt's flow (Fig. 4.4). Accurate current and velocity distributions are captured in all flows, unlike non-conservative schemes used by Ref. [76].

Error, $\varepsilon$, was computed by comparing dimensionless flow rates, $\tilde{Q}$, with an analytic

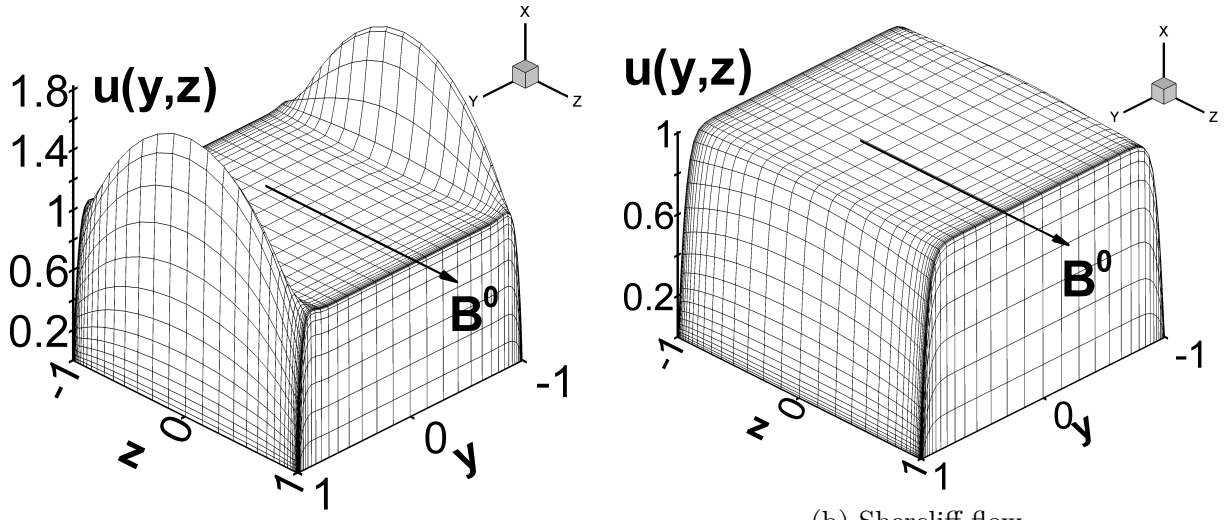


(a) Hunt flow at $Ha = 500$ and $c_w = 0.01$.

(b) Shercliff flow.

Figure 4.4: Normalized streamwise-component of velocity vs $z$ and $y$ for Hunt (a) and Shercliff (b) flows.

solution as suggested in Ref. [22]:

$$\varepsilon = \left| \frac{\tilde{Q}_{MOONS} - \tilde{Q}_{analytic}}{\tilde{Q}_{analytic}} \right| \times 100\%. \tag{4.2}$$

The parameter $\tilde{Q}$ was computed in the uniform magnetic field region, far from axial currents generated near the flow inlet and outlet in the fringing field zones. Errors computed from Eq. (4.2) for Hunt and Shercliff flows were 0.33% and 1.2% respectively.

More recently, 2D duct flows with insulating walls (Shercliff) and conducting walls (Hunt) and a uniform and transversely applied magnetic field were simulated up to $Ha = 15000$ for $Re = 100$. A very good match with analytic solutions was found, by computing the error of the normalized flow rate, and summarized in Table (4.1). All percent errors are less than 0.2%.

| | $Ha$ | Mesh size | $\frac{\tilde{Q}_{analytic}-\tilde{Q}_{MOONS}}{\tilde{Q}_{analytic}} \times 100\%$ |
|---|---|---|---|
| Insulating | 500 | $50 \times 50$ | $-0.036\,07$ |
| | 5000 | $60 \times 60$ | $-0.012\,47$ |
| | 10000 | $80 \times 80$ | $-0.018\,91$ |
| | 15000 | $100 \times 100$ | $-0.001\,12$ |
| Conducting | 500 | $50 \times 50$ | $-0.080\,93$ |
| | 5000 | $60 \times 60$ | $-0.127\,21$ |
| | 10000 | $80 \times 80$ | $-0.157\,56$ |
| | 15000 | $100 \times 100$ | $-0.083\,79$ |

Table 4.1: Percent error of normalized flow rate $\tilde{Q}$ for 2D MHD duct flow for insulating walls (Shercliff) and conducting walls (Hunt) for $c_w = 0.01$.

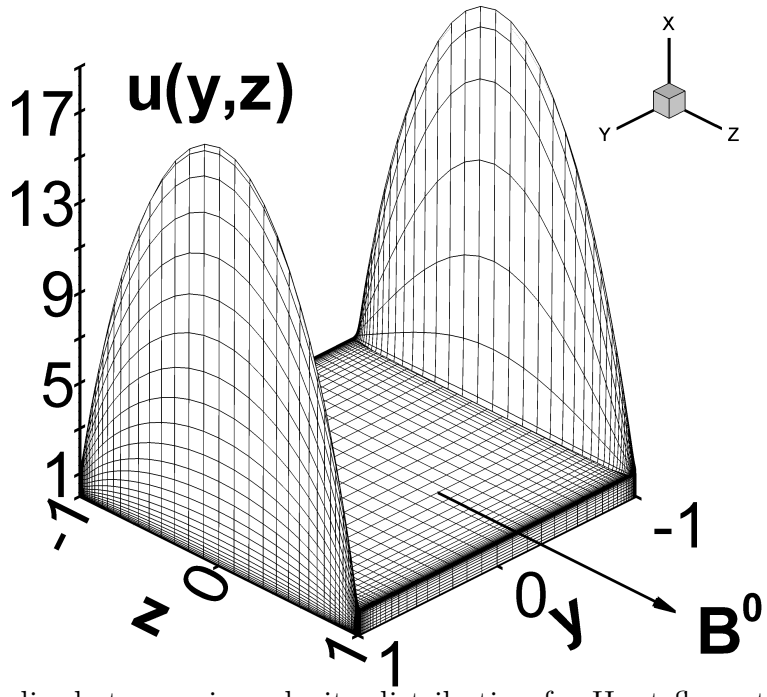


Figure 4.5: Normalized streamwise velocity distribution for Hunt flow at $Ha = 15000$ and $c_w = 0.01$.

Thin Hartmann BLs are observed near the walls perpendicular to the applied magnetic field and uniform core flow and side wall jets in Hunt's flow (Fig. 4.5). The velocity profiles in Figs. 4.4b, 4.4a and 4.5 were normalized by $Re(c_w + 1)/(Ha[c_w Ha + \tanh(Ha)])$. Ensuring the divergence-free magnetic field constraint and using the flux conserving scheme results in accurate current and velocity distributions.

## 4.3 Moderate $Re_m$ MHD flows

### 4.3.1 A 2D pressure-driven moderate $Re_m$ MHD flow

To verify the moderate $Re_m$ capabilities of MOONS, a 2D pressure-driven MHD channel flow was simulated and compared with numerical data in Ref. [43] for $Re = 200, Ha = 25.82$ and $Re_m = 1$. The channel was assumed to be infinitely long and periodic in $y$ and $x$ directions respectively with dimensions $(0 \leq x \leq 2\pi, -1 \leq z \leq 1)$ and $N_{cells} = (64, 64)$. Velocity and induced magnetic field BCs on $z = \pm 1$ were no slip and $\mathrm{B}_z = 0, \partial \mathrm{B}_x/\partial z = 0$, enforcing zero current.

The applied magnetic field resembles one of opposing magnets with opposite sign (Fig. 4.6a). The fluid drags the magnetic field lines (Fig. 4.6b), resulting in a distorted overall magnetic field. Similarly, the magnetic field retards fluid motion with spatial periodicity, resulting in periodic fluid motion (Fig. 4.6a). An excellent match between numerical data is seen in Fig. 4.6c, where axial velocity distributions are shown at different locations along the channel.

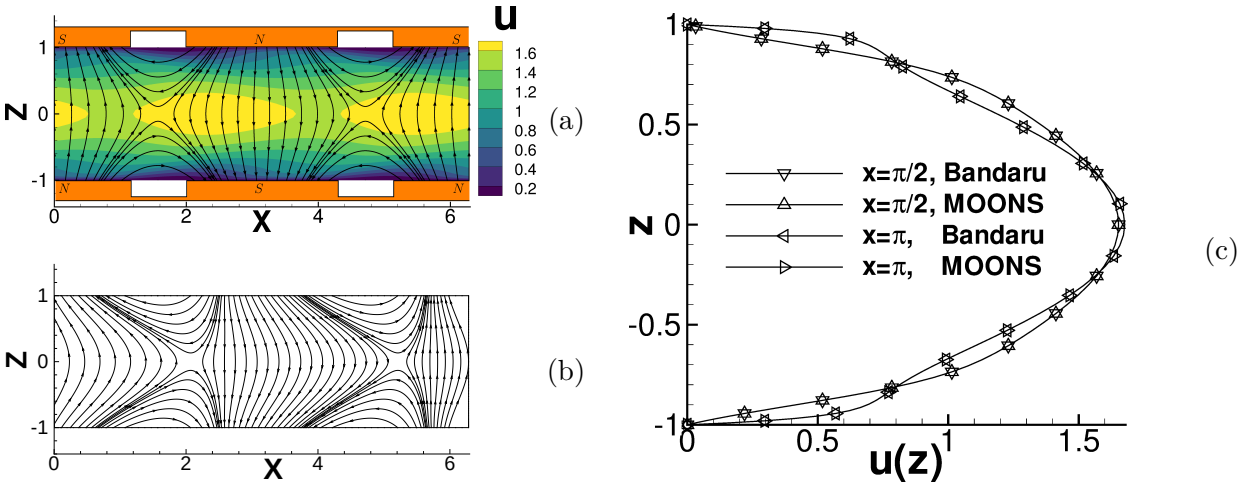


Figure 4.6: (a) axial velocity and lines of $\mathbf{B}^0$. (b) lines of $\mathbf{B}^0 + \mathbf{B}^1$. (c) axial velocity comparison at $x = \pi/2, \pi$.

Additional computations were carried out at $Re = 200$, $Re_m = 1$ and $Re_m = 10$ and several Hartmann numbers using the same scaling in Ref. [43], which includes $Re_m$ in the convective terms in the momentum equation. A good match of the transition from Hartmann

to Poiseuille regimes is observed (Fig. 4.7) by the time-averaged the streamwise core velocity plotted as a function of the inverse interaction number, $Q = Re/Ha^2$. The core velocity is defined as

$$U_{core} = \frac{1}{(t_2 - t_1)L} \int_{t_1}^{t_2} \int_{0}^{2\pi} u|_{z=0} dx dt. \tag{4.3}$$

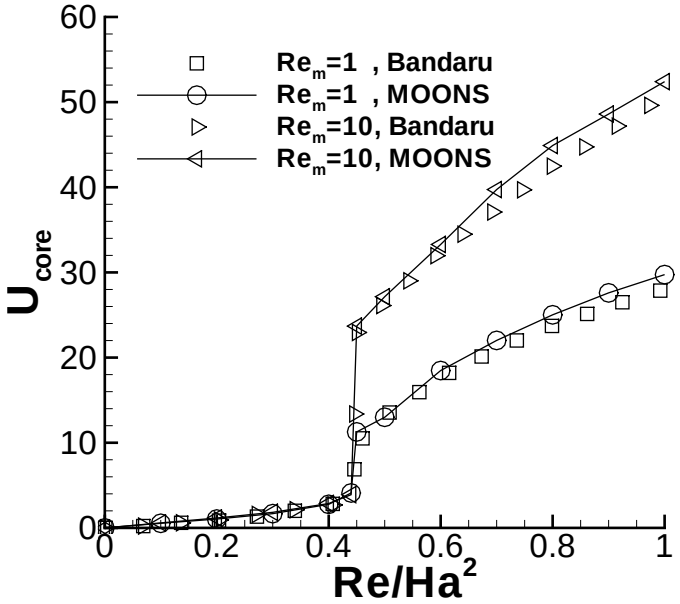


Figure 4.7: Effect of $Re_m$ on Hartmann to Poiseuille transition, visualized by the streamwise core velocity, as a function of inverse interaction number $Q$.

### 4.3.2 An unsteady, time-varying applied magnetic field-driven moderate $Re_m$ MHD flow

An analytic solution was derived [in § (A.1)] for a simplified 1D model steady fully developed MHD channel flow with a constant $B_{toroidal}$ and time-varying $B_{poloidal}$ (Fig. 1.4) with material properties typical of a fusion blanket. Solutions were plotted in Figs. 4.8a and 4.8b for several Hartmann numbers.

Interestingly, this closely resembles an "inverse"-type Hartmann solution. Specifically, our velocity field resembles the induced magnetic field for the Hartmann solution, and our induced magnetic field resembles the Hartmann velocity solution. Looking at the symmetry

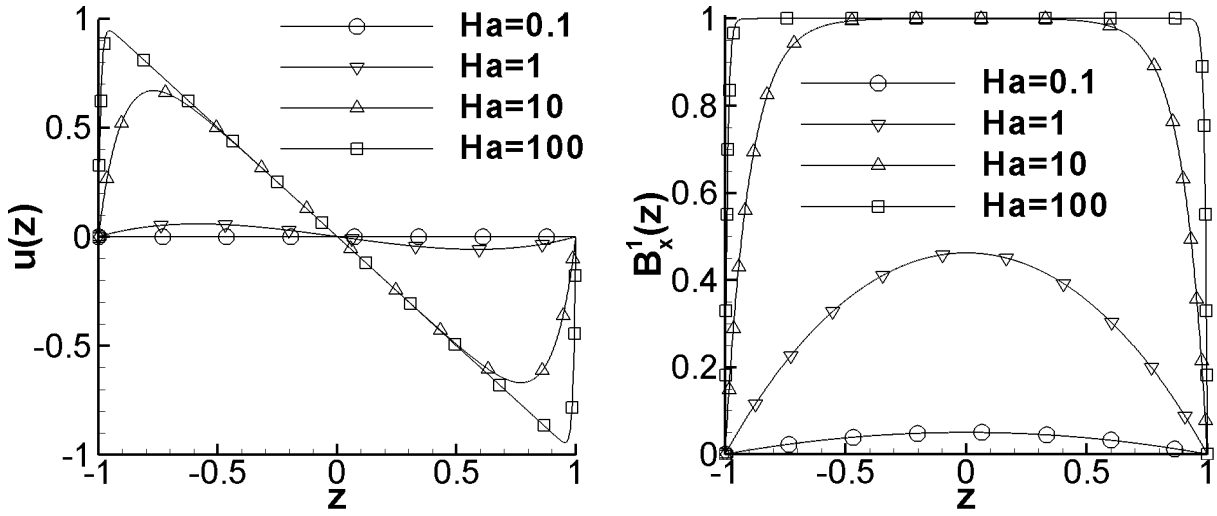


(a) $u$ vs $z$.

(b) $B_x^1$ vs $z$.

Figure 4.8: Dimensionless velocity and induced magnetic field solutions for a simplified 1D plasma disruption scenario for several Hartmann numbers.

of the governing equations, we can see that the time-varying applied magnetic field acts as an analog pressure gradient for the induced magnetic field, and the velocity field reacts to the applied and induced magnetic field.

A comparison was conducted between MOONS and the analytic solution for $Ha = 100, Re_m = 100$. The dimensionless velocity and induced magnetic field agree extremely well.

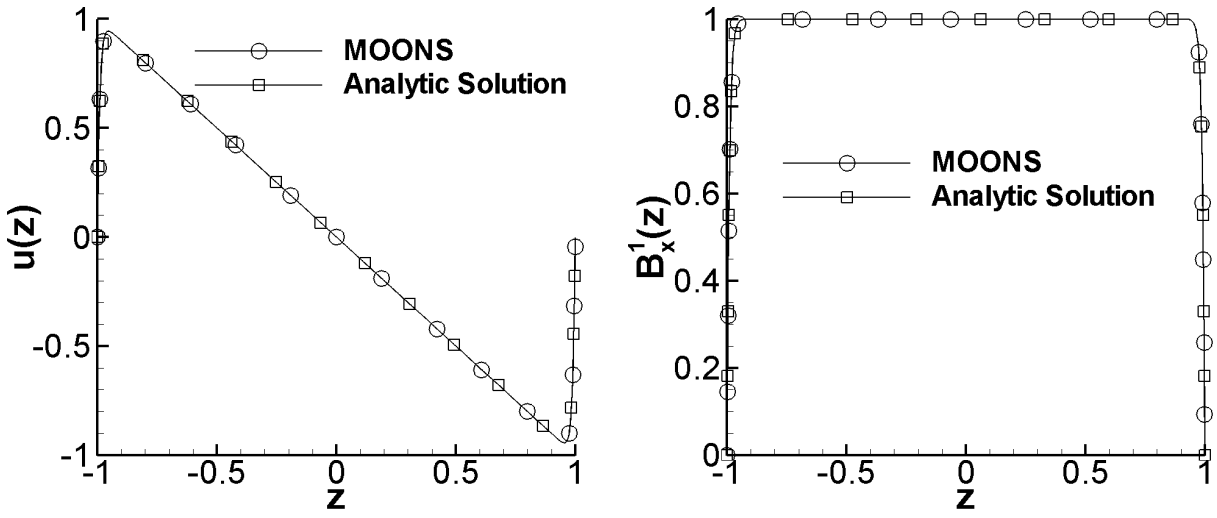


(a) $u$ vs $z$.

(b) $B_x^1$ vs $z$.

Figure 4.9: Comparison of MOONS computation with a simplified 1D plasma disruption-driven moderate $Re_m$ MHD flow.

# CHAPTER 5

# Applications

## 5.1 Preliminary tests

### 5.1.1 Selecting the electrical conductivity of the insulating outer domain

The electrical conductivity of the outer domain, $\overline{\sigma}_v$, is ideally zero but, because Eq. (2.8) is solved continuously across $\Gamma_c$, $\overline{\sigma}_v$ cannot be set to zero because it appears in the denominator. Moreover, the computational effort is increased as $\overline{\sigma}$ becomes more discontinuous across $\Gamma_c$. Therefore, the largest $\overline{\sigma}_v$ approaching zero must be determined such that the solution no longer significantly changes as $\overline{\sigma}_v$ is further decreased. The preliminary study to determine a suitable $\overline{\sigma}_v$ was performed at $Re_m = 1000$. The high $Re_m$ case was used because the induced magnetic field would likely reach far into $\Omega_v$. Performing computations at very low $\overline{\sigma}_v$ would not have been possible with explicit time-marching because the stiffness of the matrix to be inverted in Eq. (3.8) becomes too severe. It is worth noting that as $\overline{\sigma}$ becomes more discontinuous across $\Gamma_c$, the matrix inversion in Eq. (3.8) becomes increasingly ill-conditioned, dramatically benefits from preconditioning, and requires tens of iterations to converge. Changing from the implicit to explicit marching still requires tens of iterations to solve Eq. (3.8) at each time-step but the time-step restriction can be significantly relieved. For example, a reduction of four orders of magnitude was demonstrated for $\overline{\sigma}_v = 10^{-4}$, and results in considerably faster computations.

Equations (3.5-3.10) were solved until the velocity and magnetic fields reached a steady-state. To determine when steady-state is reached, the integral dimensionless kinetic energy $E_{\mathbf{u}}$ and induced magnetic field energy $E_{\mathbf{B}^1}$ were monitored as a function of time:

$$E_{\mathbf{u}}(t) = \int_{\Omega_f} E_K d\Omega, \qquad E_K = \frac{1}{2}\mathbf{u} \bullet \mathbf{u}, \tag{5.1}$$

$$E_{\mathbf{B}^1}(\Omega^*, t) = \int_{\Omega^*} E_M d\Omega, \qquad E_M = \frac{1}{2} Al\mathbf{B}^1 \bullet \mathbf{B}^1. \tag{5.2}$$

Here, $\Omega^*$, $E_K$, $E_M$ are the domain of integration, and local dimensionless kinetic and magnetic energy respectively. In addition, the integral dimensionless Joule heating was computed:

$$E_{\mathbf{j}}(\Omega^*, t) = \int_{\Omega^*} E_J d\Omega, \qquad E_J = \frac{Ha^2}{Re} \frac{\mathbf{j}^2}{\overline{\sigma}}. \tag{5.3}$$

Here, $E_J$ is the Joule-heating. $E_{\mathbf{u}}$, $E_{\mathbf{B}^1}$, and $E_{\mathbf{j}}$ can be directly compared because they all require the multiplication of the same physical scale, $\rho U^2 L^3$, to recover energy in Joules. The steady-state percent difference between $E_{\mathbf{B}^1}(\Omega_f, t)$ at $\overline{\sigma}_v = 4 \times 10^{-3}$, $2 \times 10^{-3}$, $1 \times 10^{-3}$, and $5 \times 10^{-4}$ were 2.3%, 1.2%, and 0.4% respectively (see Fig. 5.1). From here on, $\overline{\sigma}_v = 10^{-3}$ was used for the vacuum domain.

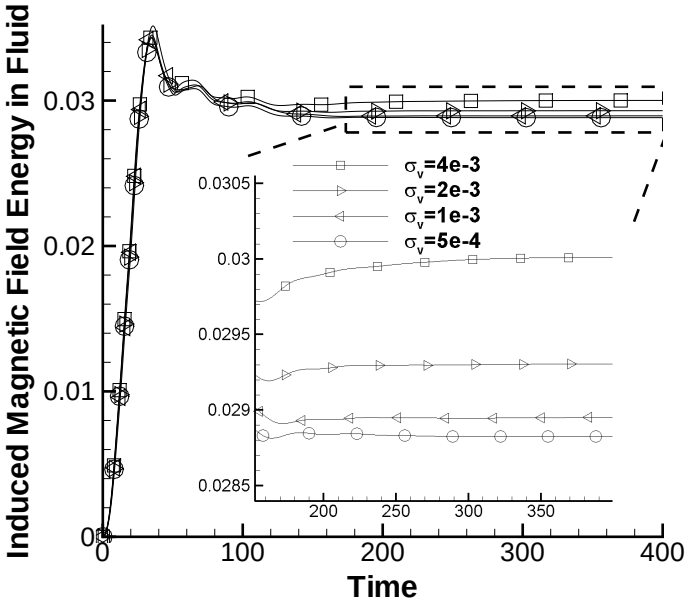


Figure 5.1: Effect of the electrical conductivity of the insulating outer domain on the computed magnetic energy.

### 5.1.2 Mesh independence study

Additionally, a mesh refinement study has been conducted to ensure that sufficient grid points were used to resolve the flow and accurately depict the energy of the system. Computations were carried out at $Re_m = 200$ with four grid resolutions: $N_{cells} = \{51,840\}$, $\{278,528\}$, $\{1,614,720\}$, and $\{10,264,320\}$. Cells were concentrated near the cavity side walls and moving lid, due to the velocity discontinuity. The steady-state percent difference of integral kinetic and magnetic energies between the second finest and finest grids are 0.66% and 1.1% (see Fig. 5.2) respectively. The second finest grid was used for the remainder of this study.

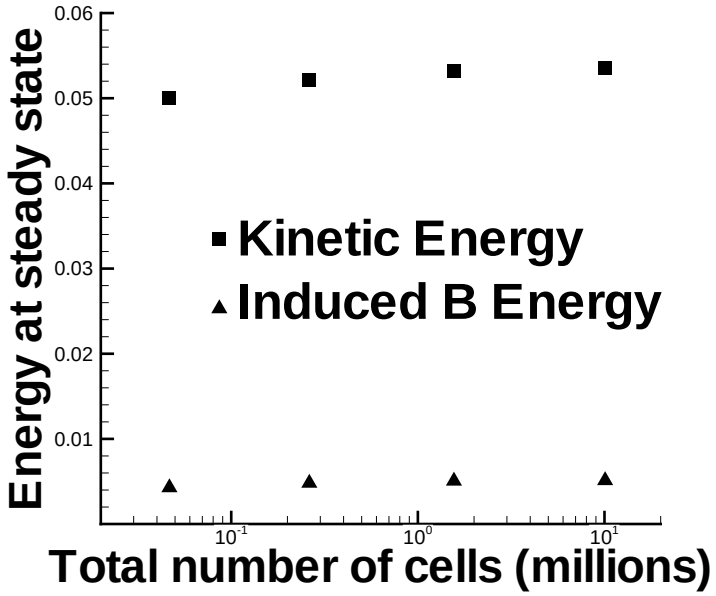


Figure 5.2: Grid independence study at $Re_m = 200$.

### 5.1.3 Selecting the computational domain size

The computational domain consists of the conducting LM, conducting wall and vacuum domains. In the present study, a sufficiently large computational vacuum domain is used to model an infinitely large one. The size is large enough when, as the domain is further increased in size, the solution no longer significantly changes. The size of the vacuum domain can be estimated using Eq. (2.15). The equation reveals that the induced magnetic field

strength decays proportionally to $Re_m/|\mathbf{r}|^3$ in vacuum sufficiently far from the conductor. So, the size of the domain should be roughly proportional to $Re_m$. In this work, the domain size was tested for $Re_m = 1000$ in light of this information.

The MHD LDC flow was simulated at $Re_m = 1000$ using total domain sizes of volumes $\{\Omega_{t,1}, \Omega_{t,2}, \Omega_{t,3}, \Omega_{t,4}\} = \{3.5^3, 7^3, 14^3, 28^3\}$. The percent difference in the total kinetic energy between $\Omega_{t,1}$ and $\Omega_{t,2}$, $\Omega_{t,2}$ and $\Omega_{t,3}$, and $\Omega_{t,3}$ and $\Omega_{t,4}$ was $0.31\%, 5.4\times10^{-4}\%$ and $6.5\times10^{-5}\%$ respectively. The final chosen total domain size was that of volume $14^3$, and is used for the remainder of this study.

## 5.2 Moderate $Re_m$ MHD flow characterization

### 5.2.1 Steady to unsteady flow comparison

Initially, the flow is at rest, and the induced magnetic field is zero everywhere. As the driven lid shears the fluid, the fluid is stirred and circulates the cavity until the velocity and induced magnetic fields reach steady conditions. A steady velocity and induced magnetic field distribution will exist, or not exist, depending on $Re_m$, $Ha$, $Re$ and $c_w$. Also, we caution that due to the possibility of hysteresis (see Ref. [45]), the uniqueness of the solution should be checked for moderate $Re_m$ MHD flows. Steady-state solutions are more likely to exist at lower $Re$, lower $Re_m$ and higher $Ha$, where the fluid is typically characterized as being dominated by viscous forces, with a negligible induced magnetic field and strong magnetic field damping.

There are three and four timescales for low and moderate $Re_m$ MHD flows respectively. The characteristic convective time, or eddy turn-over time, estimates the time for the largest scale eddy to perform a full 360-degree revolution. The diffusion time is the time for momentum to diffuse a distance $L$ in a single diffusive time unit. The Hartmann damping time is the time for the magnetic field to damp the flow to a two-dimensional configuration. The magnetic diffusive time, or resistive decay time, is the time for the magnetic field to diffuse a distance $L$ in a single magnetic diffusive time unit.

The effect of increasing $t_m$, by increasing $Re_m$ (or, more specifically, $\mu_m$), is seen in Figs. 5.3a and 5.3b. The integral kinetic energy is more damped and reaches a steady-state more quickly at low $Re_m$ and the steady-state integral induced magnetic field energy is proportional to $Re_m$. The time required for the solution to reach a steady-state, increases as $Re_m$ increases (Fig. 5.3a), which agrees with observations seen in kinematic MHD studies at $Re_m = 1000$ by Ref. [15]. The integral steady-state induced magnetic field energy is plotted in Fig. 5.4, which demonstrates that the scaling is nearly linear in a range of $Re_m$ up to roughly 500, at which point the scaling begins to resemble an exponential growth. Interestingly, the steady-state kinetic energy is nearly the same across all $Re_m$ despite an increasing difference in kinetic energy with increasing $Re_m$ during the unsteady period. Despite having nearly the same integral kinetic energy, the velocity and magnetic field distributions vary across the range of $Re_m$, as will be shown in later sections. The energy balance will be further analyzed in § (5.2.6).

The temporally asymptotic integral induced magnetic field energy in the fluid and its components are plotted in Fig. 5.4 versus $Re_m$ in the form of a Root-Mean-Square (RMS) scaled by either the total or applied magnetic field. The RMS is computed using the following formula:

$$RMS(\chi, \Upsilon) = \frac{\sqrt{\int_{\Omega_f} \chi d\Omega}}{\sqrt{\int_{\Omega_f} \Upsilon d\Omega}}. \tag{5.4}$$

Here, $\chi$ and $\Upsilon$ are dummy scalar fields. Figure 5.4 clearly demonstrates that the magnetic field behavior is nearly linear in a range of $Re_m$ up to roughly 500, and then begins to resemble an exponential growth. Another useful observation is that the induced magnetic field reaches the magnitude of the applied one at $Re_m \approx 850$. Interestingly, the non-linear behavior and unsteadiness also become pronounced at about the same $Re_m$, possibly indicating that the strongest modifications of the flow start as soon as the induced and applied magnetic field become nearly equal.

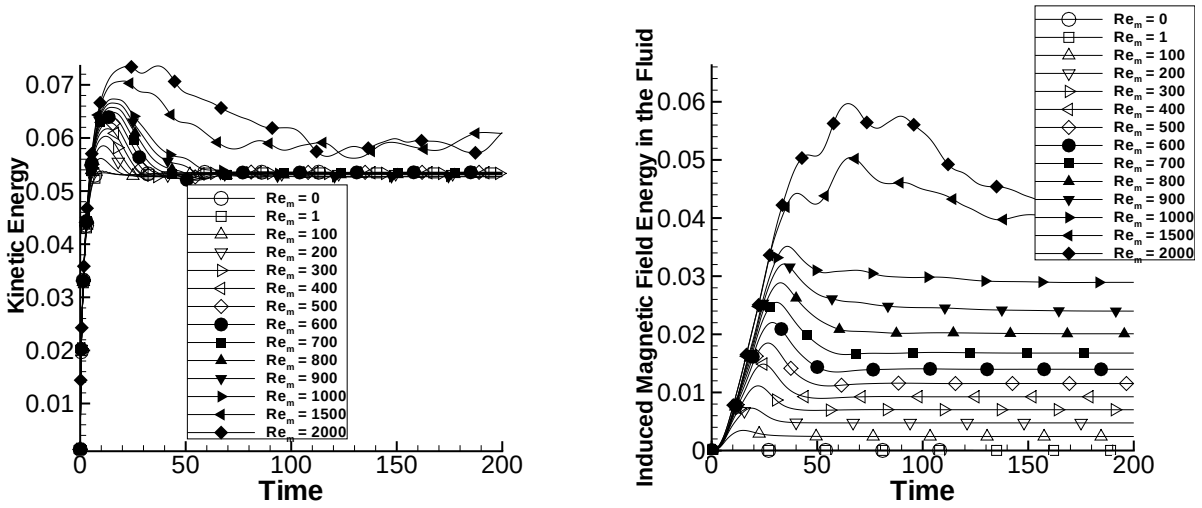


(a) (b)

Figure 5.3: Kinetic energy (a) and induced magnetic field energy (b) over time.

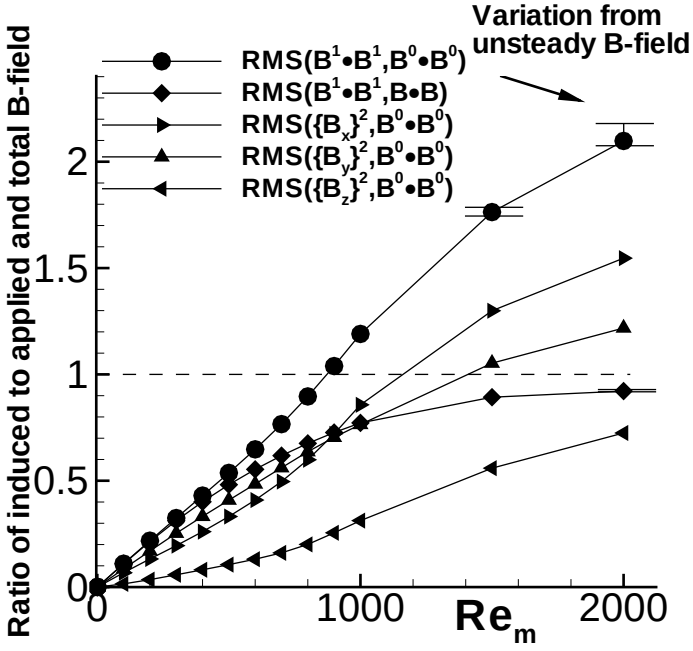


Figure 5.4: Ratio of the steady-state induced to applied magnetic field energy vs. $Re_m$.

### 5.2.2 Applicability of the inductionless approximation

In the MHD flows where the $Re_m$ is small, the induced magnetic field is small and can be neglected compared to the applied one. Also, convection of the magnetic field is negligibly small compared to diffusion and can be neglected. In such conditions, the governing equations

are simplified to the inductionless form as briefly discussed in § (1). The applicability of the inductionless approximation depends on the magnitude of $Re_m$. Typically, the inductionless approximation is valid if $Re_m << 1$ (see Refs. [41, 45]). However, some authors claim that accurate results can be obtained using the inductionless approximation even for $Re_m$ of the order of unity (see Refs. [41, 18]). The results of the present study demonstrate that for the reference MHD LDC flow, the range of applicability of the inductionless approximation depends on whether or not the flow is in a steady-state. For unsteady flows, as shown in § (5.2.1), the effect of $Re_m$ on the flow can be neglected only if $Re_m << 1$. If the flow reaches the steady-state, the situation is different. Namely, the steady-state integral kinetic energy becomes independent of the $Re_m$ for even high $Re_m \sim 10^2$, while the induced magnetic field changes linearly with $Re_m$ for $Re_m$ up to $\sim 500$. The seemingly invariant integral kinetic energy in this range may suggest that the inductionless approximation is still valid, but this idea cannot be fully justified without looking carefully at the distributions of the velocity, induced magnetic field and induced currents. This verification was performed in the present section for $Re_m = 0, 1, 100, 500$ and 1000, for which the solution had converged to the steady-state.

The effect of $Re_m$ on the steady-state velocity distributions as a function of $x$ and $y$ is illustrated in Fig. 5.5. Clearly, for $0 < Re_m < 100$, the effect of $Re_m$ is very small. In fact, a difference between three velocity curves plotted at $Re_m = 0$, 1 and 100 is not visually seen. Significant changes in both $u$ and $v$ velocity components are however seen at $Re_m = 500$ and 1000. The $u$ component has a larger overshoot at higher $Re_m$ compared to lower $Re_m$ near the lid (Fig. 5.5a). The $v$-component of velocity along the $x$-direction (Fig. 5.5c) is more oscillatory at higher $Re_m$.

A normalized induced magnetic field was computed, $\beta^1 = \frac{\mathbf{B}^1 - \min(\mathbf{B}^1)}{\max(\mathbf{B}^1) - \min(\mathbf{B}^1)}$, in order to compare the relative values of the distributions at various $Re_m$. Due to symmetries in the $x$ and $y$-components of the magnetic field, and the existence of a steady solution, the min and max are equal with opposite sign ($\min(B_x, B_y) = -\max(B_x, B_y)$). The shape of the magnetic field distribution does not significantly change between $Re_m = 0$ and $Re_m =$

100 (Figs. 5.6a, 5.7a, 5.8a, 5.6b, 5.7b, and 5.8b) suggesting a solution with pronounced self-similarity. However, the magnetic field distribution does change shape at larger $Re_m$ (Figs. 5.6c, 5.7c, 5.8c, 5.6d, 5.7d, and 5.8d), indicating a change in electric current paths and no self-similar solution anymore.

Similar trends can be observed in the distributions of the induced electric current in Fig. 5.9. The current distributions appear nearly the same for the $0 < Re_m < 100$ cases (see Figs. 5.9a, 5.9b, 5.9c, 5.9d). The $x$ and $y$ components of electric current along the $x$ and $y$ directions have very complicated distributions (Figs. 5.9a, 5.9c, 5.9b, and 5.9d). They are nearly zero in the fluid domain along the $z$ direction but significantly larger in the conducting walls (Figs. 5.10a and 5.10b). The $z$-component of electric current varies quite rapidly even between $Re_m = 0$ and $Re_m = 100$ along the $z$-direction (Fig. 5.10c) demonstrating one or two inflection points depending on $Re_m$.

To conclude this section, it appears that in the range $0 < Re_m \lesssim 100$, the inductionless approximation is applicable. In this range, the $Re_m$ has almost no effect on the velocity field and the induced electric current, while the induced magnetic field demonstrates similarity and changes linearly in magnitude with $Re_m$.

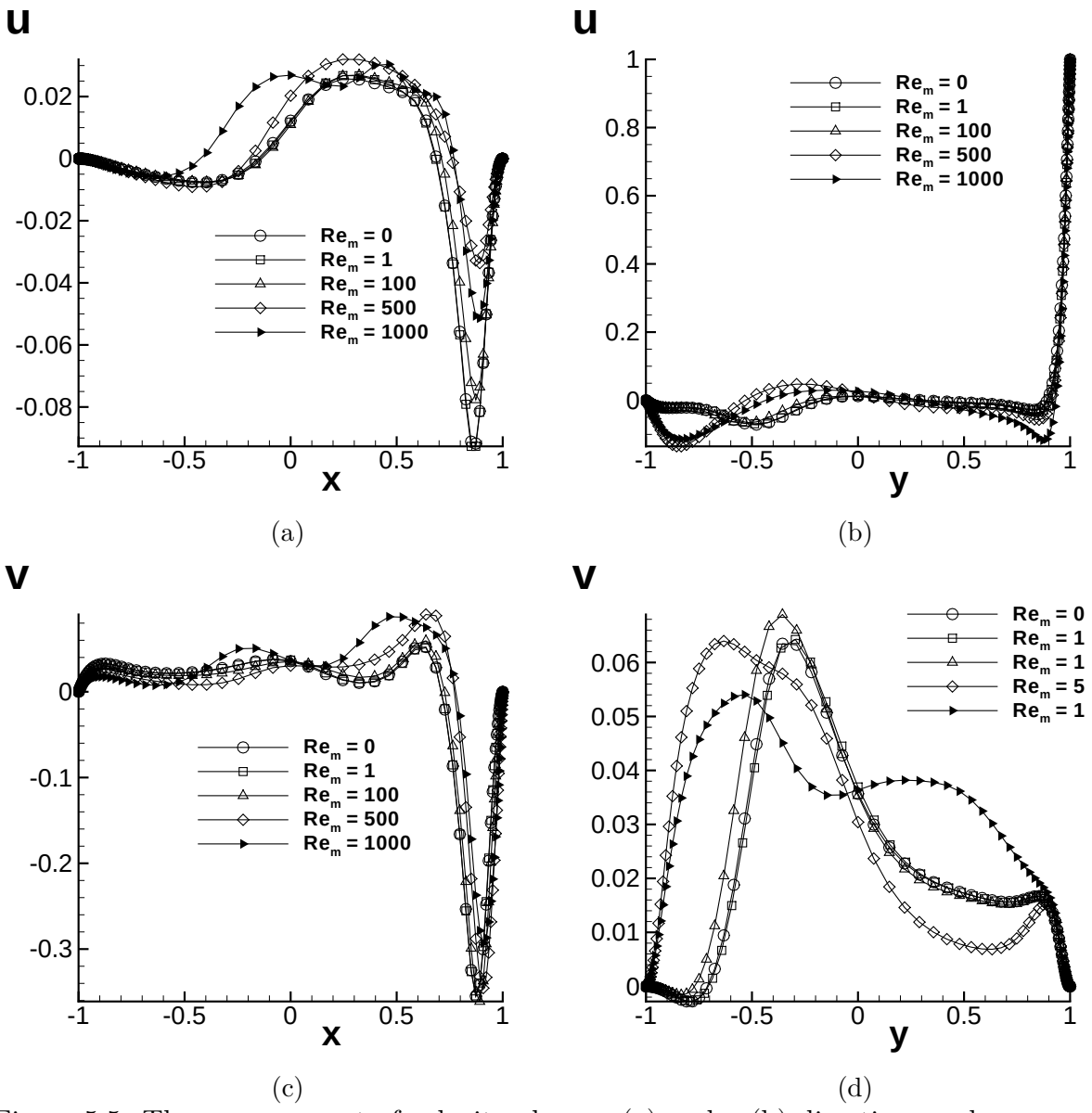


(a) (b)

(c) (d)

Figure 5.5: The $u$-component of velocity along $x$ (a) and $y$ (b) directions and $v$-component of velocity along $x$ (c) and $y$ (d) directions in the cavity center.

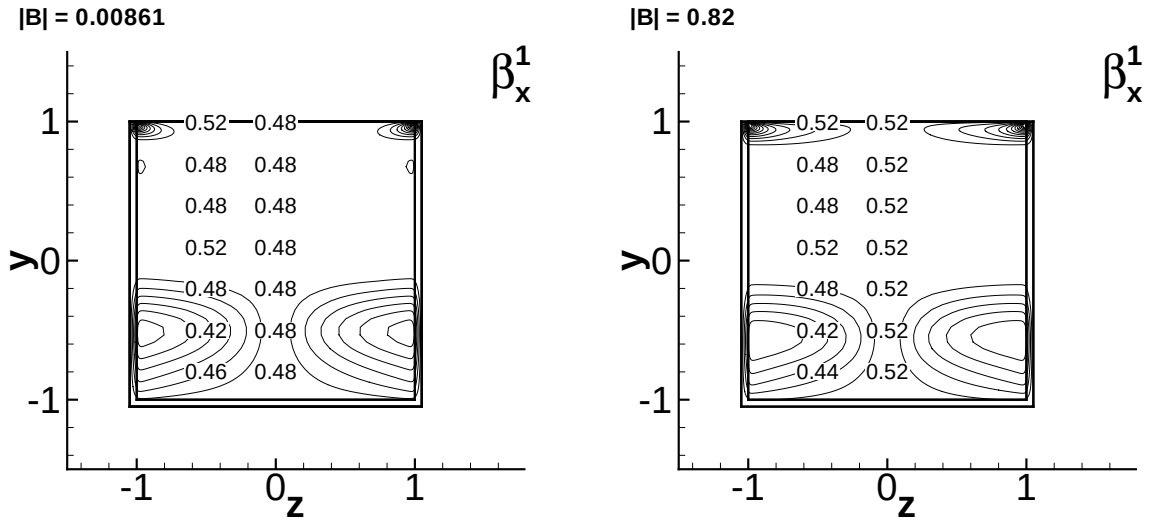


(a) $Re_m = 0$




(b) $Re_m = 100$

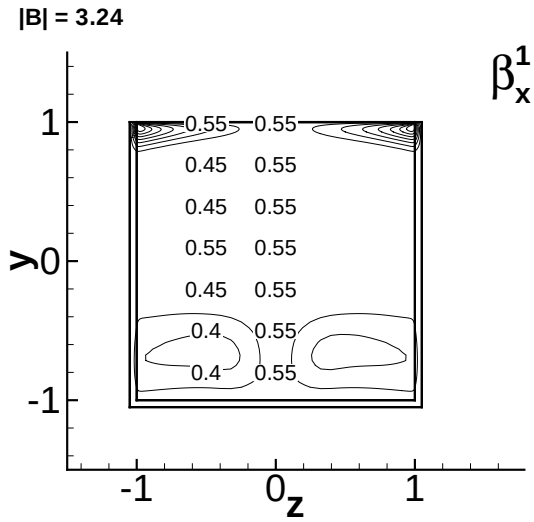


(c) $Re_m = 500$

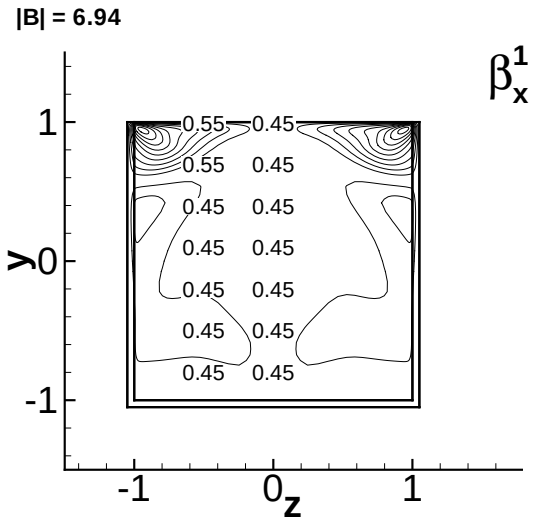


(d) $Re_m = 1000$

Figure 5.6: The $x$ component of induced magnetic field contours from $x$ direction in the cavity center.

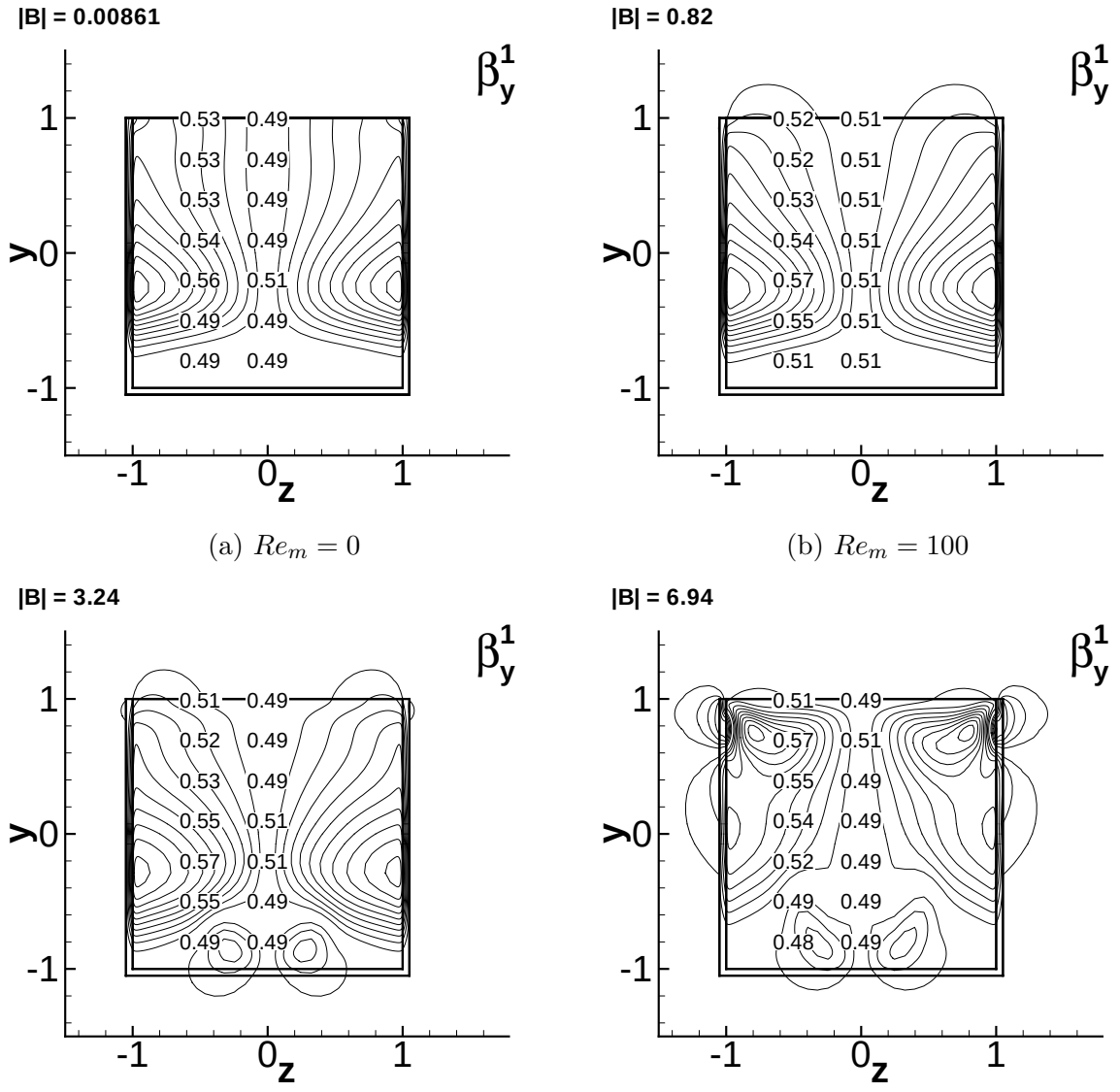


(a) $Re_m = 0$ (b) $Re_m = 100$

(c) $Re_m = 500$ (d) $Re_m = 1000$

Figure 5.7: The $y$ component of induced magnetic field contours from $x$ direction in the cavity center.

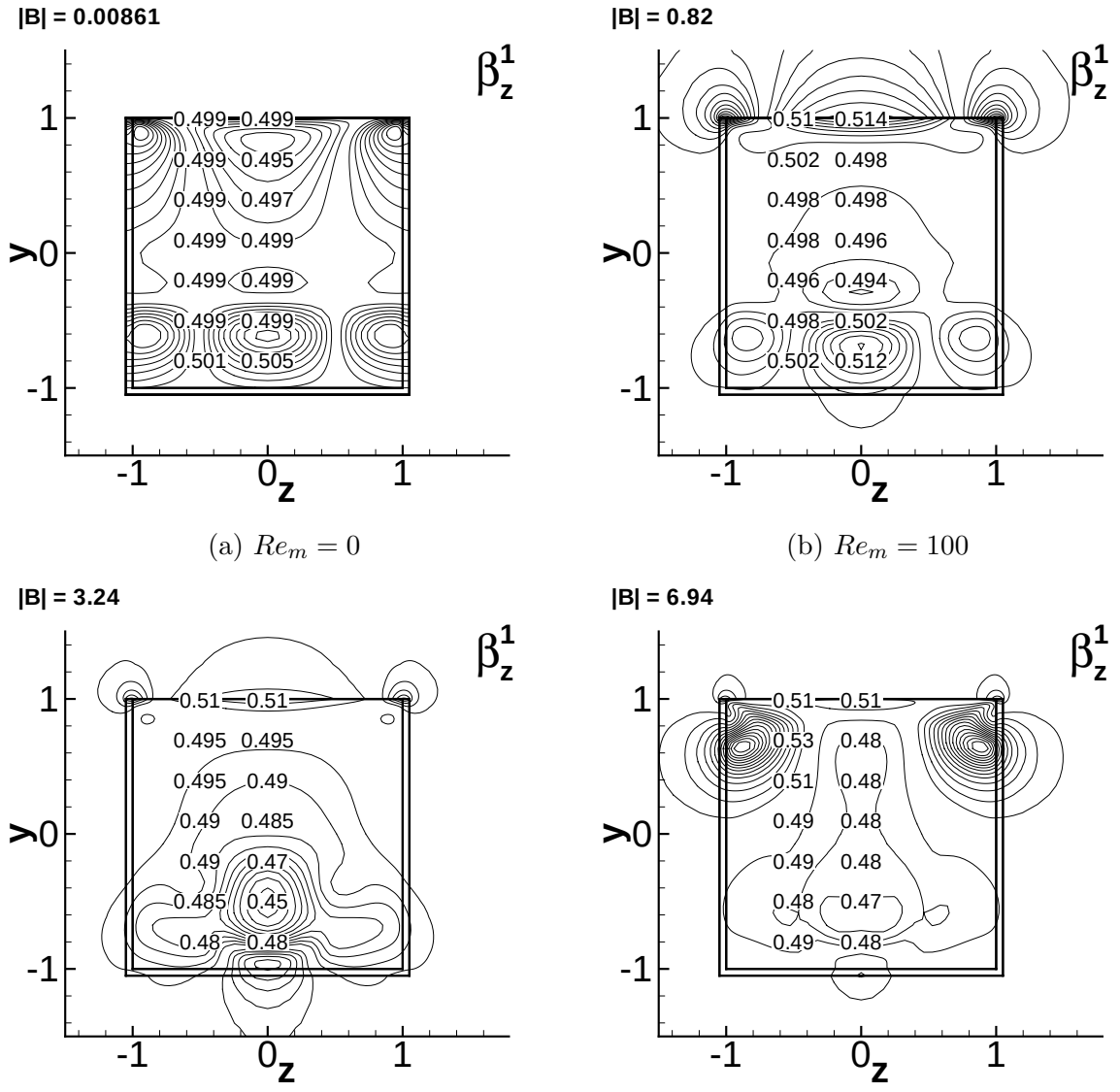


(a) $Re_m = 0$

(b) $Re_m = 100$

(c) $Re_m = 500$

(d) $Re_m = 1000$

Figure 5.8: The $z$ component of induced magnetic field contours from $x$ direction in the cavity center.

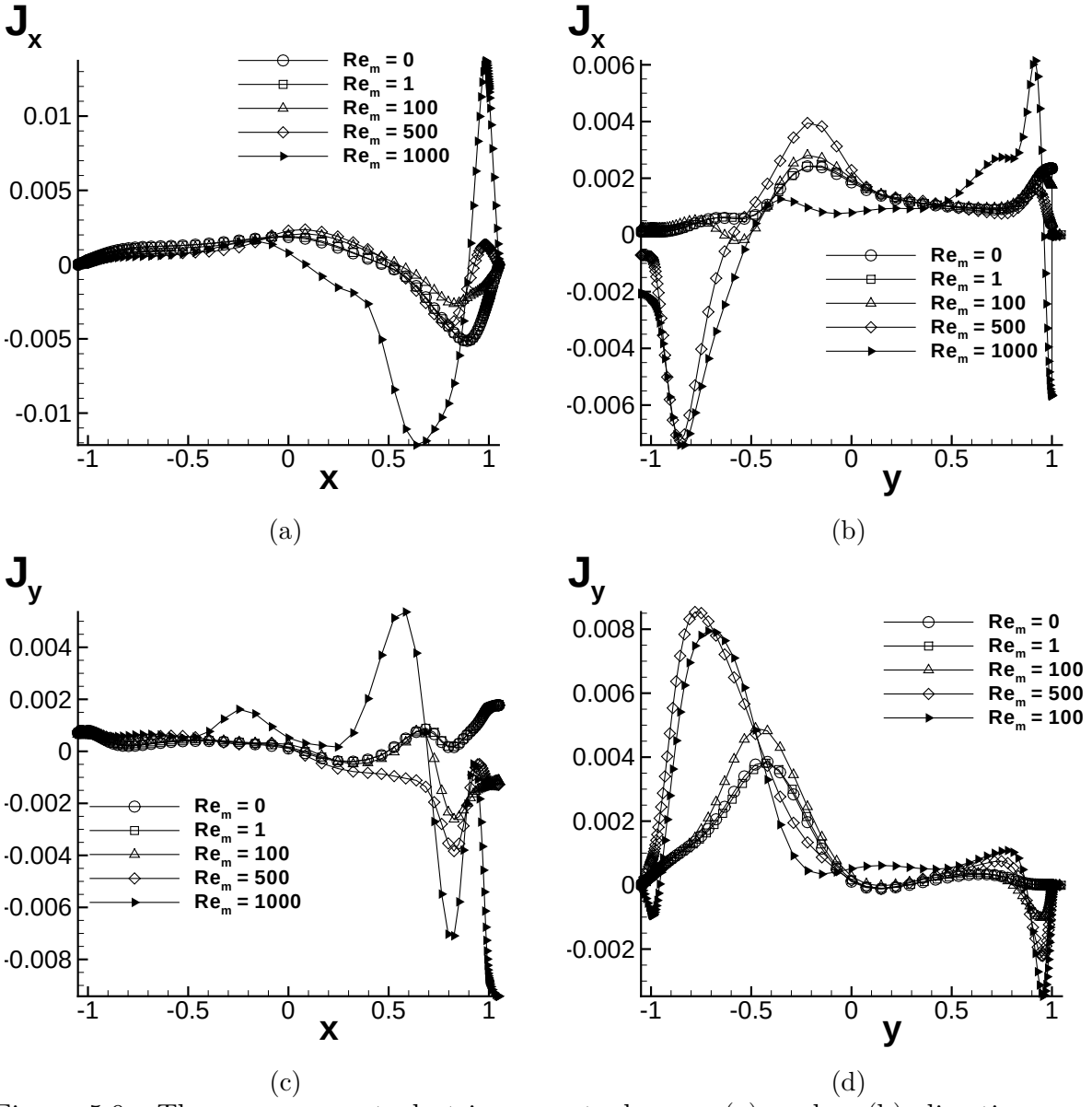


Figure 5.9: The $x$-component electric current along $x$ (a) and $y$ (b) directions and $y$-component electric current along $x$ (c) and $y$ (d) directions in the cavity center.

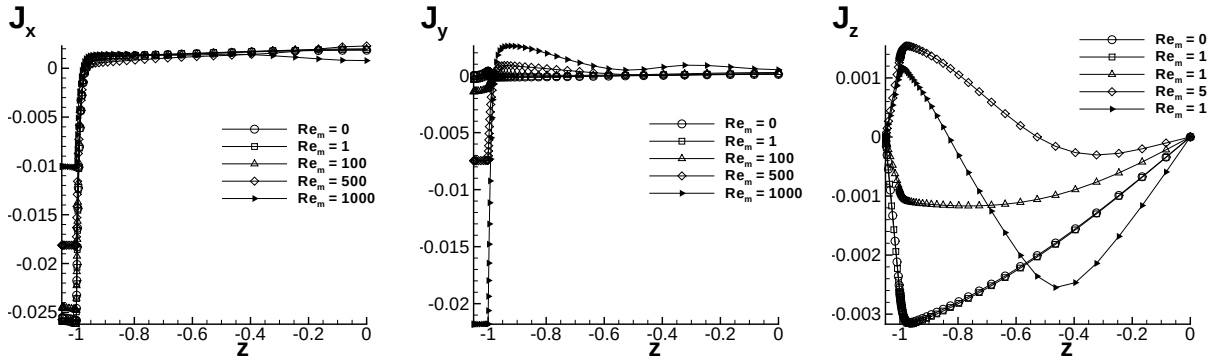


(a) (b) (c)

Figure 5.10: The $x$ (a), $y$ (b) and $z$ components of electric current along the $z$ direction in the cavity center for half of the domain.

### 5.2.3 Two-dimensionality

The Lorentz force decelerates the flow and, as a result, suppresses motion along the applied magnetic field direction leading to flow two-dimensionalization at low $Re_m$ except in a small BL (the Hartmann layer) near $z = \pm 1$.

This effect is clearly observed in the velocity, seen in Figs. 5.11a, 5.12a, and 5.13a). As $Re_m$ increases, the flow becomes more three-dimensional (Figs. 5.11c-5.11d, 5.12c-5.12d, and 5.13c-5.13d). This effect is in agreement with laminarization and two-dimensionalization due to decreasing $Re_m$ for turbulent duct MHD flow at moderate $Re_m$ seen in Ref. [45].

The local two-dimensionality was measured by computing $P_{2D} = |\mathbf{u} - \mathbf{u}_{center}|$, where $\mathbf{u}_{center}$ is the velocity at the cavity center. $P_{2D}$ was plotted as a function of $z$ at $x = 0, y = 0$ in Figs. 5.15a, 5.15b, and 5.15c. Results show that the flow is mostly two-dimensional when $Re_m = 0$, and becomes more three-dimensional as $Re_m$ increases. While it was expected that the most three-dimensional flows, according to this metric, occur at higher $Re_m$, the magnitude at which the flow becomes three-dimensional is much higher than was originally anticipated, hence why our parameter space was increased to $Re_m = 1000$.

The two-dimensionality at low $Re_m$ can also be observed via the induced magnetic field. From the central plane in the x-direction of the driven cavity flow, the induced magnetic field appears similar to two duct flows in opposing directions (Figs. 5.6a and 5.6b), and from

this, the two-dimensionality can be observed. Similarly, the induced magnetic field shows three-dimensionality (Figs. 5.6c and 5.6d) at higher $Re_m$.

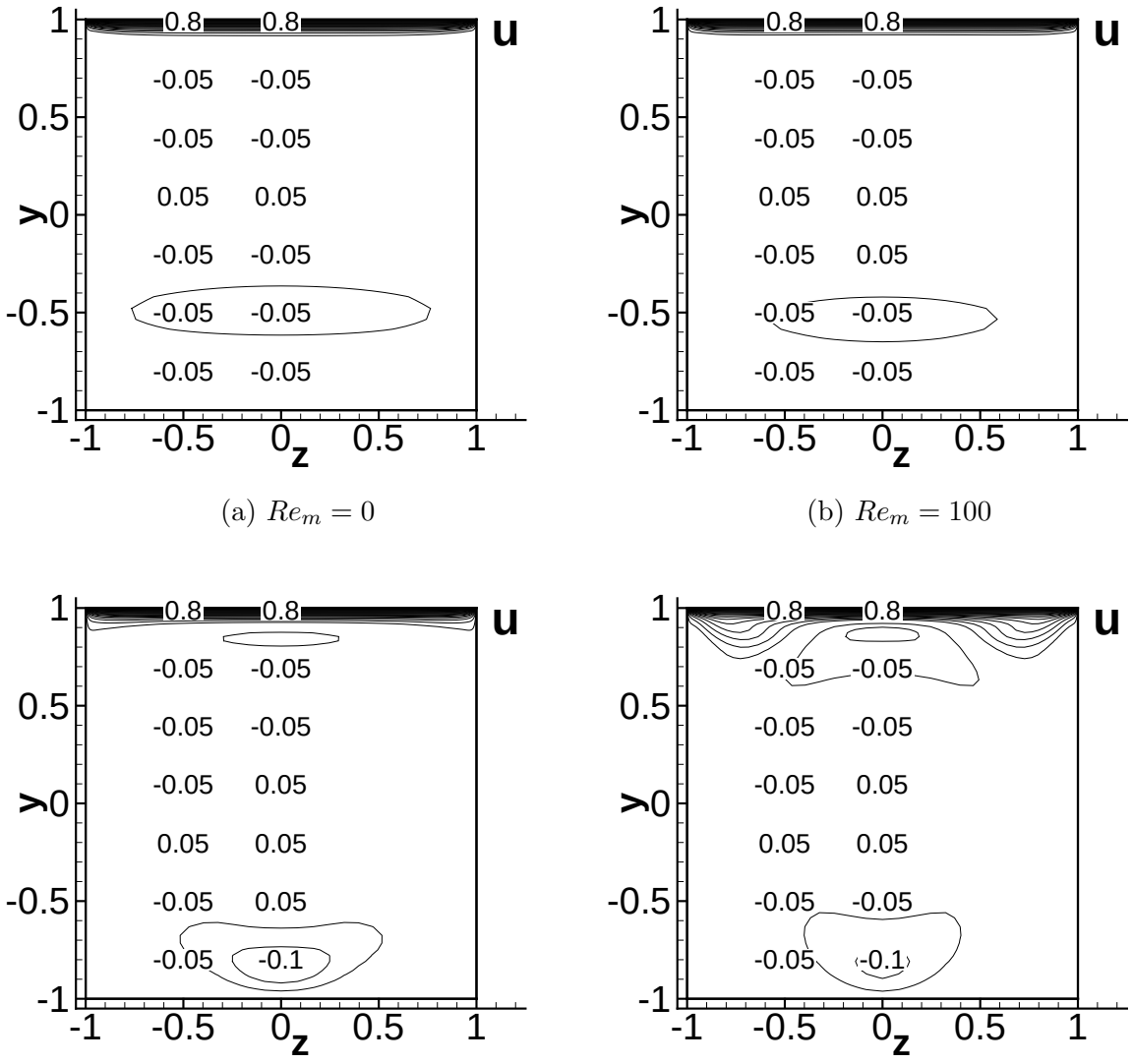


(a) $Re_m = 0$

(b) $Re_m = 100$

(c) $Re_m = 500$

(d) $Re_m = 1000$

Figure 5.11: $u$ component velocity contours from $x$ direction in cavity center.

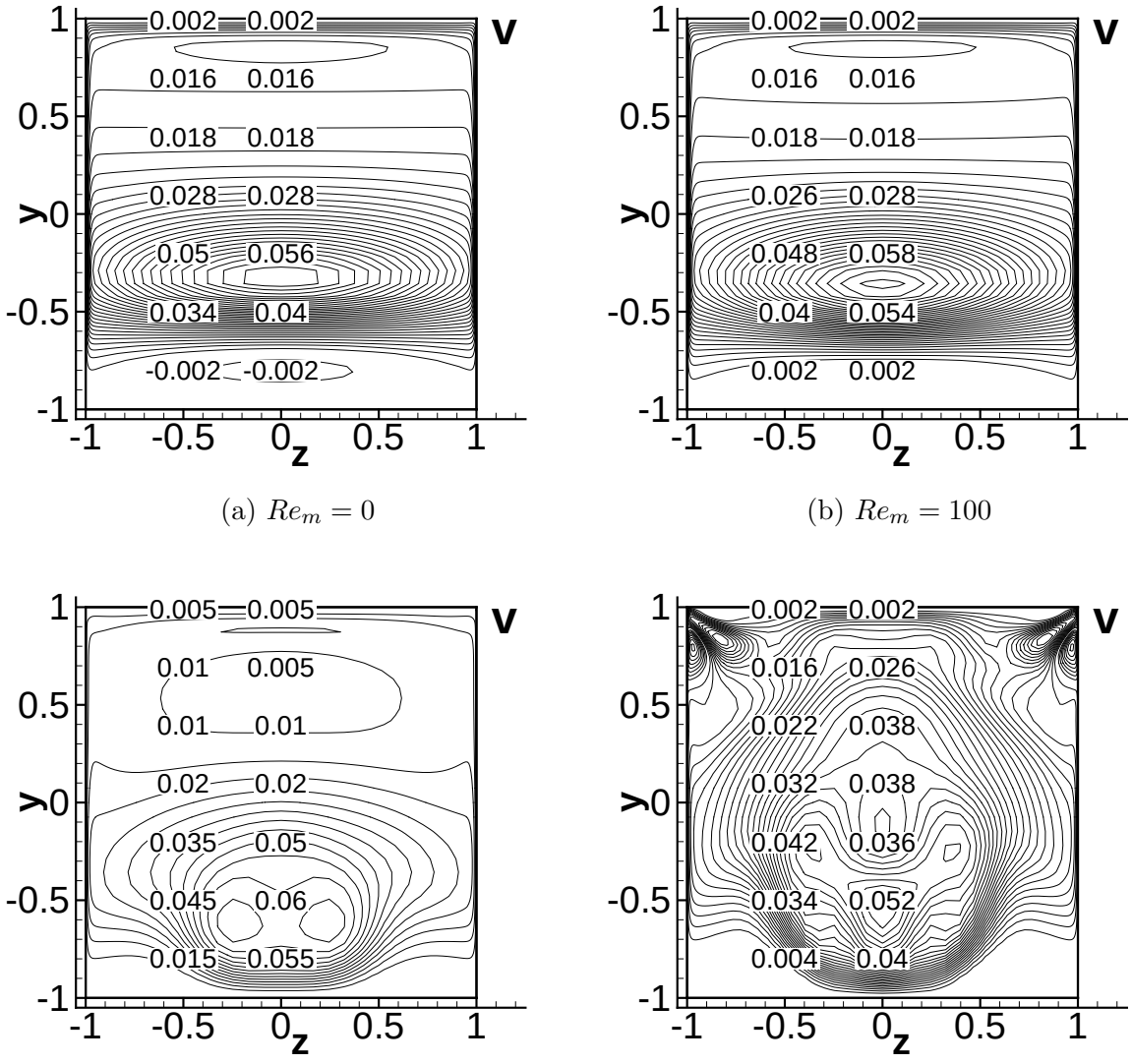


(a) $Re_m = 0$

(b) $Re_m = 100$

(c) $Re_m = 500$

(d) $Re_m = 1000$

Figure 5.12: $v$ component velocity contours from $x$ direction in cavity center.

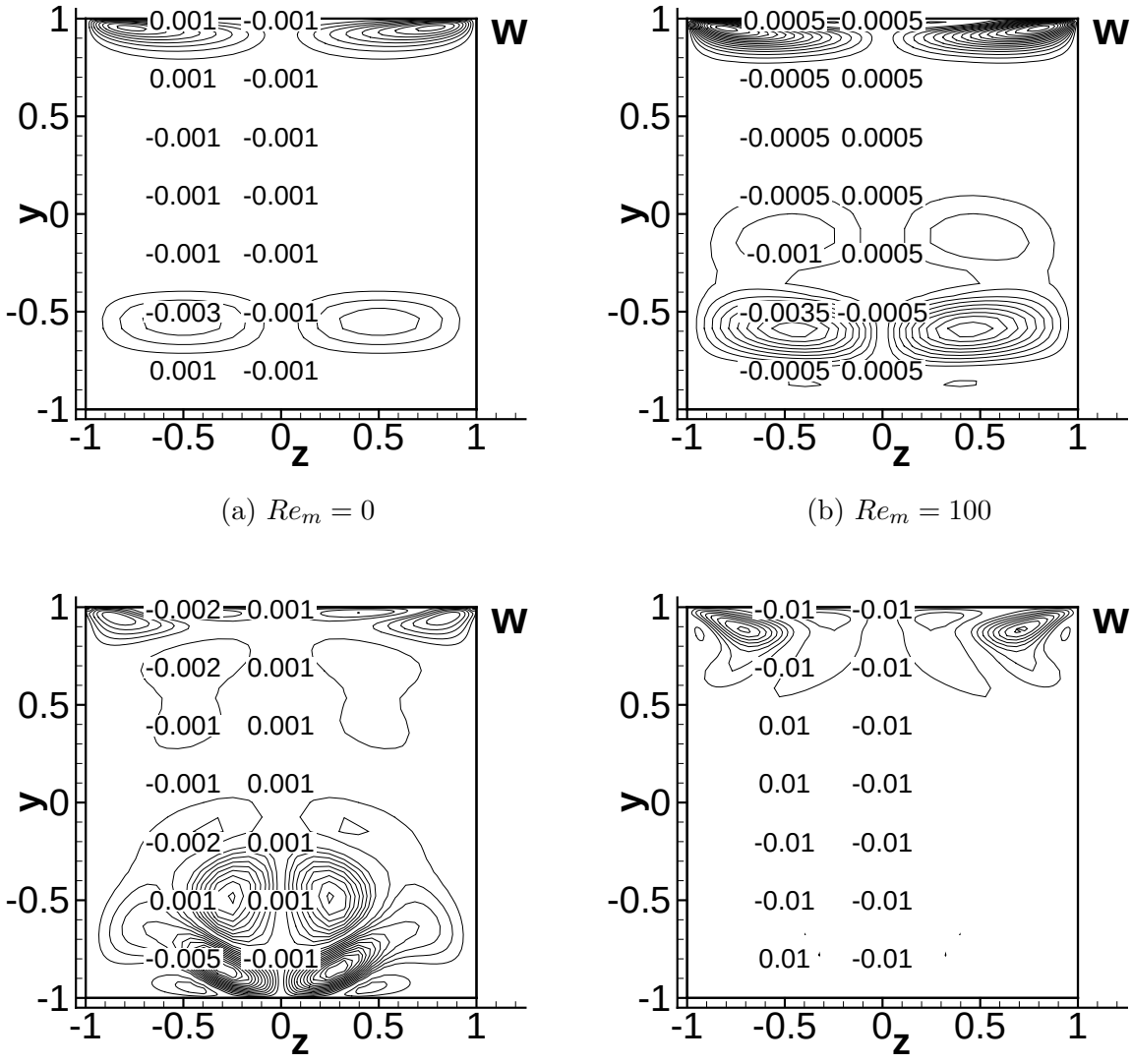


(a) $Re_m = 0$ (b) $Re_m = 100$

(c) $Re_m = 500$ (d) $Re_m = 1000$

Figure 5.13: $w$ component velocity contours from $x$ direction in cavity center.

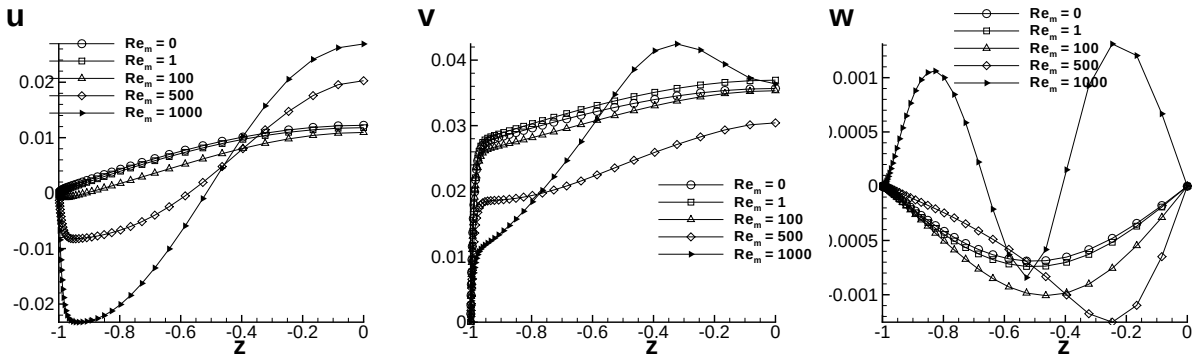


(a) (b) (c)

Figure 5.14: Velocity distributions along $z$ direction in cavity center in half domain.

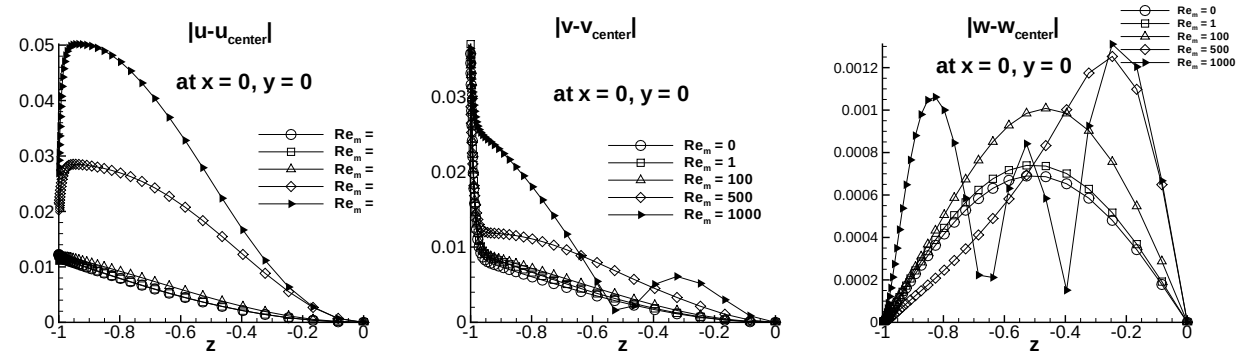


(a) (b) (c)

Figure 5.15: Velocity distributions along $z$ direction in cavity center in half domain.

### 5.2.4 Frozen magnetic field lines and flux expulsion

In the high $Re_m$ limit, the total magnetic field becomes *frozen* to the velocity field and, therefore, magnetic field lines become purely tangential at the driven lid (see Ref. [1]). This trend is clearly observed in the present computations as shown in Fig. 5.16, where total magnetic field lines are traced in a grid of 10 by 10 points at $z = -1.05$, and follow the path to the other end of the cavity at $z = 1.05$. Naturally, in Fig. 5.16a, at $Re_m = 0$ the induced magnetic field strength is negligible, so the total applied magnetic field lines pass straight through the cavity. Alternatively, at higher $Re_m$, in Figs. 5.16b, 5.16c, and 5.16d, the induced magnetic field is non-zero and distort the total magnetic field lines as they pass through the cavity. Expectedly, the severity of the magnetic field line stretching is

proportional to $Re_m$. Interestingly, stretching of the total magnetic field lines appear to be most apparent near the $(x, y) = (1, -1)$ corner at $Re_m = 100$, rather than regions of largest velocity (near the lid).

It is noteworthy that the $z$-component of the induced magnetic field is primarily negative in the fluid domain (Figs. 5.17a, 5.17b, and 5.18c). This conceptually agrees with the magnetic flux expulsion at high $Re_m$, where the total magnetic field is expelled from the moving conductor. Even at high $Re_m$, the $z$-component of the induced magnetic field only reaches about $-0.2$, which is just 20% of full expulsion (of $B_z^1 = -1$) in the fluid domain.

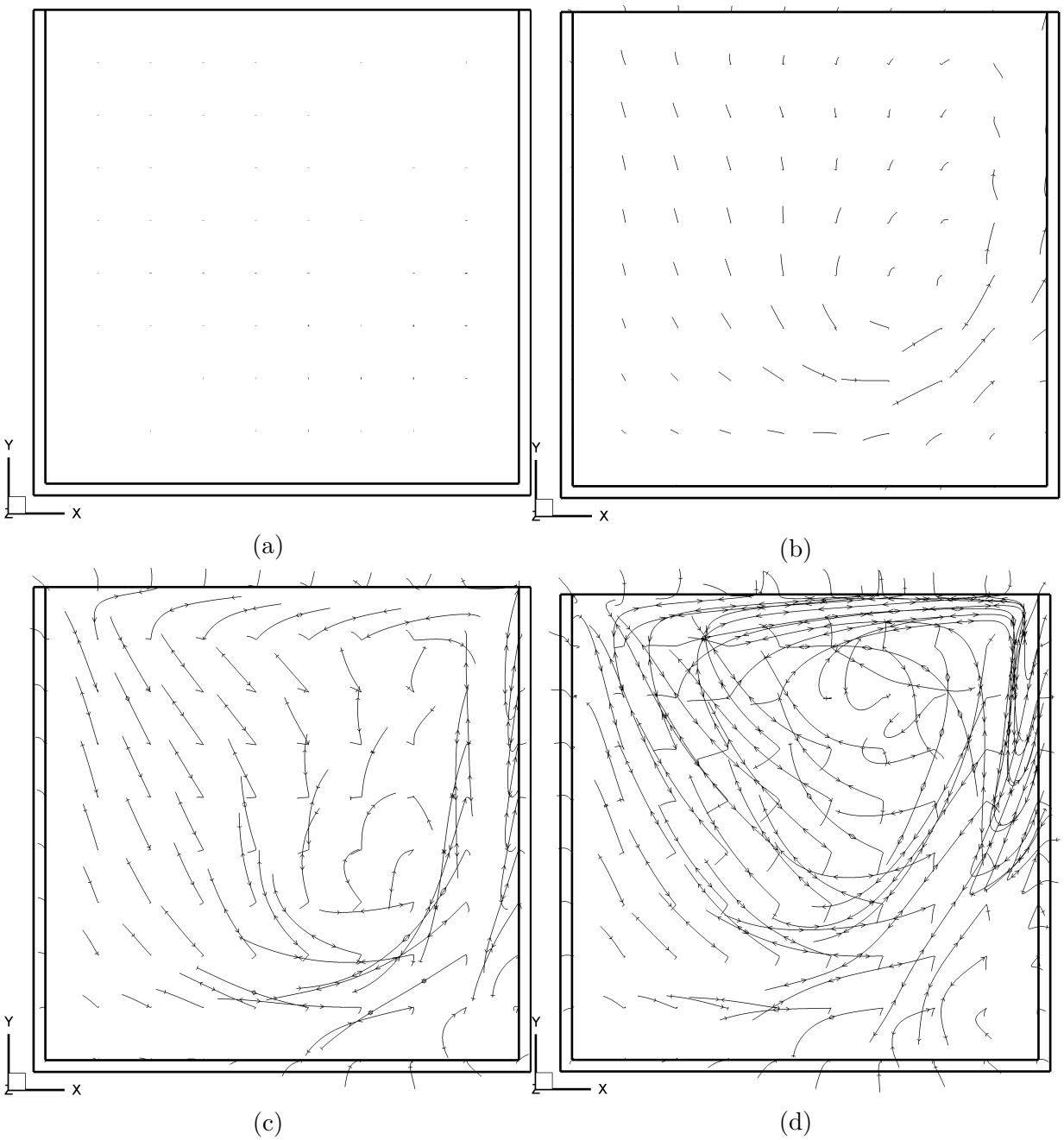


Figure 5.16: Total magnetic field lines traced in a grid of 10 by 10 points from $z = -1.05$ to $z = 1.05$, along the applied magnetic field direction for (a) $Re_m << 1$, (b) $Re_m = 100$, (c) $Re_m = 500$, and (d) $Re_m = 1000$. The magnetic field lines begin to become frozen to the flow as $Re_m$ increases.

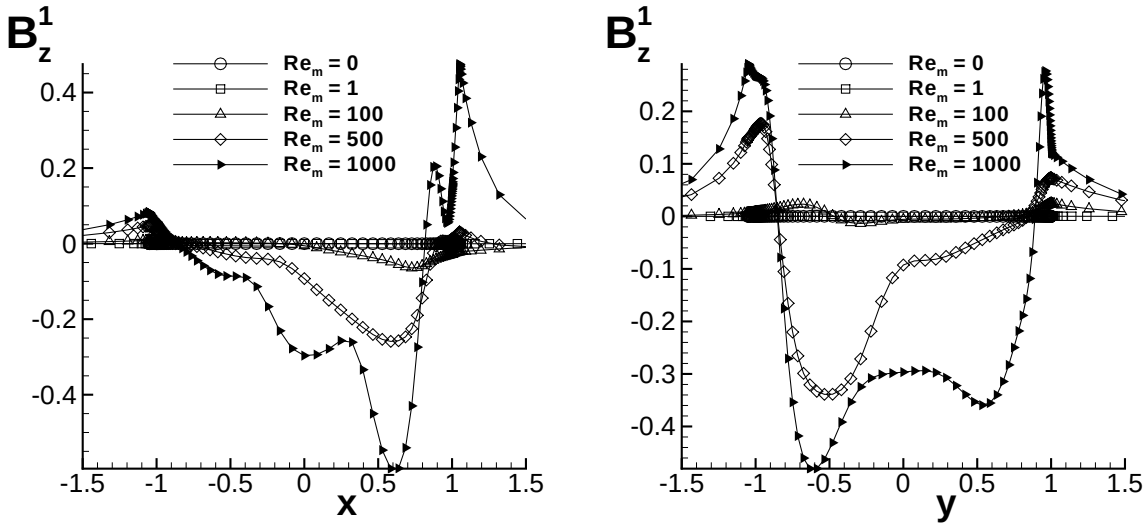


(a) (b)

Figure 5.17: Magnetic field distributions along $x$ (a) and $y$ (b) directions in the cavity center.

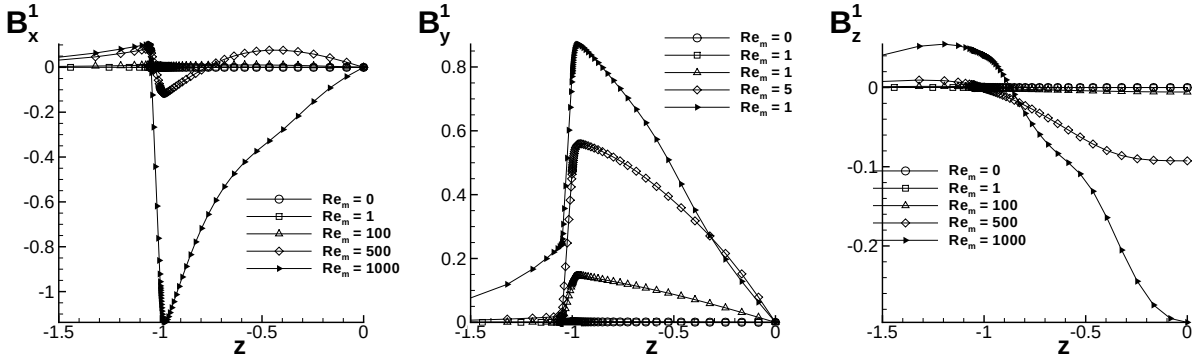


(a) (b) (c)

Figure 5.18: The $x$ (a) $y$ (b) and z (c) components magnetic field components along $z$ direction in the cavity center for half of the domain.

### 5.2.5 Magnetic field penetration into the vacuum

The induced magnetic field can penetrate far beyond the conductor and even into the vacuum. The depth at which the induced magnetic field penetrates into the vacuum is of interest because this provides useful information about the range validity of approximate local magnetic BCs. Very far from a dipole magnetic field, the field strength decreases with the inverse-cube of the distance ($1/|\mathbf{r}|^3$) but may differ for more complicated magnetic field

distributions. Specifically, local effects may cause increases in the induced magnetic field in the vacuum region nearby the conductor.

The farther the magnetic field penetrates into the vacuum, the larger the computational domain must be to satisfy the physically accurate magnetic BCs, $\mathbf{B}^1 = \mathbf{0}$, far from the conductor. Furthermore, there is interest in *how* the magnetic field penetrates into the vacuum. That is, the induced magnetic field has interface-normal and tangential components. Since approximate BCs assume that the tangential component is zero, the ratio of tangential to normal components of the induced magnetic field across the interface is of interest to better understand the range of validity of approximate induced magnetic field BCs.

First, we analyzed the decay of the induced magnetic field in vacuum. The $1/|\mathbf{r}|^3$ decay of the induced magnetic field in the vacuum domain was confirmed using a least-square fit of the induced magnetic field magnitude along the x-direction, resulted in the slopes (3.22, 3.15, 3.13, 3.13, 3.16, 3.21, 3.29, 3.41, 3.54, 3.52) for $Re_m = 100, ..., 1000$ respectively. This result confirms that our model of the physical system is accurately capturing the decay of the induced magnetic field. Furthermore, this confirms that the domain size used in the domain is sufficiently large that the weakening of the induced magnetic field satisfies continuity in the vacuum.

### 5.2.6 Energy balance and distribution as $Re_m$ increases

The only power input to the system is via the shear driven-lid (Ref. [77]),

$$\mathcal{P} = \int_{\Gamma_{lid}} u\tau_w d\Gamma. \tag{5.5}$$

Here, $\tau_w = Re^{-1}\partial_y u$ is the driving lid shear stress. Therefore, the power input depends on $Re$ and $\partial_y u$ (i.e., depends on the solution) and is therefore variable in time and space on the driving lid.

This power input is a continuous source for kinetic and magnetic energy and also accounts for dissipation losses as seen from the following equations showing the energy balance in the

entire domain, including moving liquid, solid conducting wall, and surrounding vacuum:

$$\partial_t E_K = \dot{E}_{\mathcal{C}_K} + \dot{E}_p + \dot{E}_{\mathcal{D}_K} + \dot{E}_\Phi + \dot{E}^{KE}_{\mathcal{C}_M} + \dot{E}^{KE}_{\mathcal{M}_S}, \tag{5.6}$$

$$\partial_t E_M = \dot{E}_{\mathbf{j}} + \dot{E}_{\mathcal{P}} + \dot{E}^{ME}_{\mathcal{C}_M} + \dot{E}^{ME}_{\mathcal{M}_S}. \tag{5.7}$$

Here, $\dot{E}_p, \dot{E}_{\mathcal{C}_K}, \dot{E}_{\mathcal{D}_K}, \dot{E}_\Phi, \dot{E}_{\mathcal{C}_M}, \dot{E}_{\mathcal{M}_S}, \dot{E}_{\mathbf{j}}$, and $\dot{E}_{\mathcal{P}}$ are the components of the energy balance associated with pressure, convection of kinetic energy, diffusion of kinetic energy, viscous dissipation, convection of magnetic energy, Maxwell stresses, Joule heat, and radiation (Poynting term) correspondingly. The mathematical definitions of these terms are:

$$\dot{E}^{ME}_{\mathcal{M}_S} = -Al\mathbf{u} \bullet (\mathbf{B} \bullet \nabla \mathbf{B}), \qquad \dot{E}^{KE}_{\mathcal{M}_S} = Al\mathbf{u} \bullet (\mathbf{B} \bullet \nabla \mathbf{B}),$$

$$\dot{E}^{ME}_{\mathcal{C}_M} = (\mathbf{u} \bullet \nabla) E_M, \qquad \dot{E}^{KE}_{\mathcal{C}_M} = -(\mathbf{u} \bullet \nabla) E_M,$$

$$\dot{E}_{\mathcal{P}} = Al\nabla \bullet \left[ \left( \mathbf{u} \times \mathbf{B} - \frac{\mathbf{j}}{\overline{\sigma}} \right) \times \mathbf{B} \right], \qquad \dot{E}_p = \nabla \bullet (\mathbf{u} p),$$

$$\dot{E}_{\mathbf{j}} = -AlRe_m \frac{\mathbf{j}^2}{\overline{\sigma}}, \tag{5.8}$$

$$\dot{E}_{\mathcal{C}_K} = -(\mathbf{u} \bullet \nabla) E_K,$$

$$\dot{E}_{\mathcal{D}_K} = \frac{1}{Re} \nabla^2 E_K,$$

$$\dot{E}_\Phi = -\frac{1}{Re} (\nabla \mathbf{u}) : (\nabla \mathbf{u}). \tag{5.9}$$

It is worth noting that $\dot{E}^{KE}_{\mathcal{M}_S}$ and $\dot{E}^{ME}_{\mathcal{M}_S}$, and $\dot{E}^{KE}_{\mathcal{C}_M}$ and $\dot{E}^{ME}_{\mathcal{C}_M}$, are equal with opposite signs respectively.

Equations (5.6) and (5.7) are written in a dimensionless form using the same scales such that all energy, dissipation, and other terms can be directly compared. The physical representation of most terms in Eq. (5.7) are discussed in Ref. [1] and not repeated here.

The convection and pressure terms spatially integrate (over the entire domain) to zero and do not add nor remove energy from the system. At steady-state, the unsteady terms are zero. The volume integral of the Poynting term can be converted into a surface inte-

gral and thus can be viewed as a source of magnetic energy to penetrate into the vacuum $Al\int_{\Gamma_c}\left[\left(\mathbf{u}\times\mathbf{B}-\frac{\mathbf{j}}{\bar{\sigma}}\right)\times\mathbf{B}\right]\bullet\mathbf{n}d\Gamma$. The Poynting term is zero at steady-state also, with the following explanation. Consider Eq. (5.7) in the vacuum in proximity to a conductor. No electric currents exist, and no material is moving, so the only remaining terms are the unsteady and Poynting terms. Therefore, the Poynting term spatially integrates to zero at steady-state. Therefore, the only remaining non-zero terms in Eqs. (5.6) and (5.7) after spatially integrating at steady-state are $\dot{E}_{\mathcal{D}_K}$, $\dot{E}_{\Phi}$, $\dot{E}_{\mathcal{M}_S}$ and $\dot{E}_{\mathbf{j}}$. These remaining terms were plotted in Fig. 5.19a. Interestingly, the Joule heat varies noticeably with changes in $Re_m$ and reaches a local maximum at $Re_m = 1000$. This also means, however, that *more* energy is converted from kinetic energy to magnetic energy, through the Maxwell stress term, at $Re_m = 1000$ compared to $Re_m = 2000$. Also, the steady-state integral kinetic and induced magnetic field energies were plotted together as a function of $Re_m$ in Fig. 5.19b.

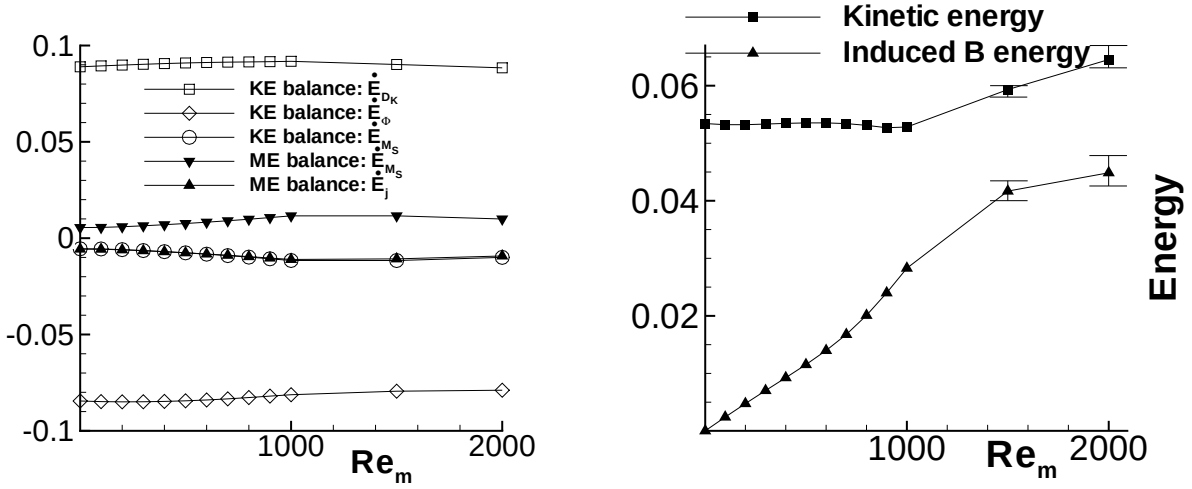


(a) Spatially integrated energy balance components in Eqs. (5.6) and (5.7).

(b) The steady-state kinetic and induced magnetic field energies.

Figure 5.19: Graphical representation of energy and energy components. The flows at $Re_m = 1500$ and $Re_m = 2000$ are unsteady. Values were computed at the last time-step for points shown without variation bars.

The striking result from Fig. 5.19b is that the kinetic energy varies very little across a large range of $Re_m$ (up to $Re_m = 1000$). The magnetic energy grows most rapidly, and the Joule heating also increases noticeably but for $Re_m < 900$, the kinetic energy of the moving

liquid is always higher than that of the induced magnetic field. Based on the computations up to $Re_m = 1000$, the steady-state induced magnetic field energy in the fluid can be roughly estimated using the following cubic formula:

$$ME(Re_m)|_{\Omega_f} = 2.1 \times 10^{-11} Re_m^3 - 2 \times 10^{-8} Re_m^2 + 2.8 \times 10^{-5} Re_m - 5.6 \times 10^{-5}. \tag{5.10}$$

Using this formula, the kinetic and magnetic energies can be estimated to become equal at $Re_m = 1320.13$. Additional computations were carried out at $Re_m = 1500$ and $Re_m = 2000$, which reveal that the transition from the kinetic energy-dominated regime to the magnetic energy-dominated regime does not occur due to significant growth in the kinetic energy and a decrease in the nominal growth of the induced magnetic field energy. Besides, these additional computations resulted in non-symmetric (with respect to the $z = 0$ plane) and unsteady flows. Due to the non-symmetric flow, both computed cases for $Re_m = 1500$ and $Re_m = 2000$ were computed using the full three-dimensional geometry, unlike many computed cases at lower $Re_m$, which utilized symmetric and anti-symmetric BCs.

Another interesting feature of the energy balance is the distribution of the magnetic energy between the conducting domain (fluid and containing walls) and the vacuum. The magnetic energy was computed in each of the domains and plotted in Fig. 5.20. Interestingly, the magnetic energy in the fluid is between 1 and 2 orders of magnitude larger than that of the wall and vacuum, which are within an order of magnitude of each other, for all $Re_m$ and the magnetic energy seems to increase with $Re_m$ at the same rate in all of the domains equally.

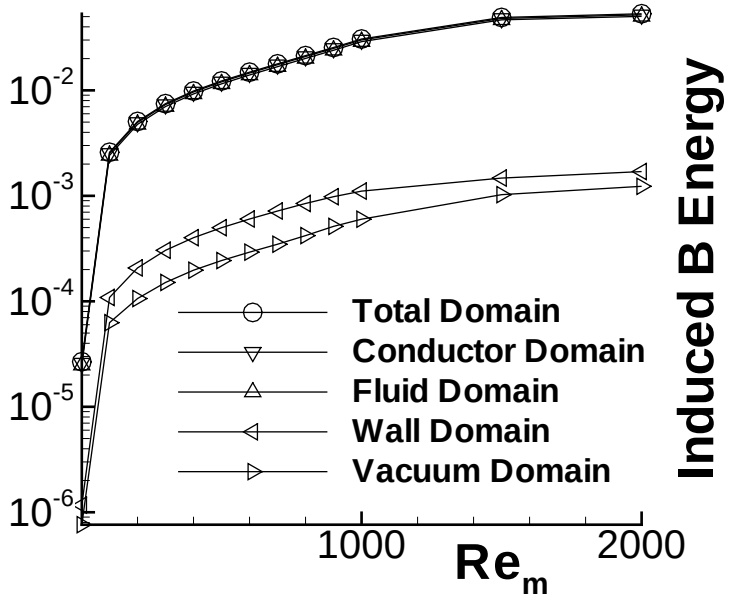

Figure 5.20: The steady-state magnetic energy in different domains.

Analyzing the energy balance in more detail, iso-surfaces of the steady-state kinetic energy and induced magnetic field energy were plotted in Figs. 5.21 and 5.22 respectively. The velocity streamtraces (Fig. 5.21) show a contorted path, which changes shape with increasing $Re_m$. Obviously, most of the kinetic and magnetic energy is localized near the driving lid. In the liquid, the kinetic and magnetic energies resemble a "j"-like shape and roughly coincide with lower $Re_m$ (Figs. 5.21 and 5.22). At higher $Re_m$, the "j"-like shape structure of kinetic and magnetic energy breaks down.

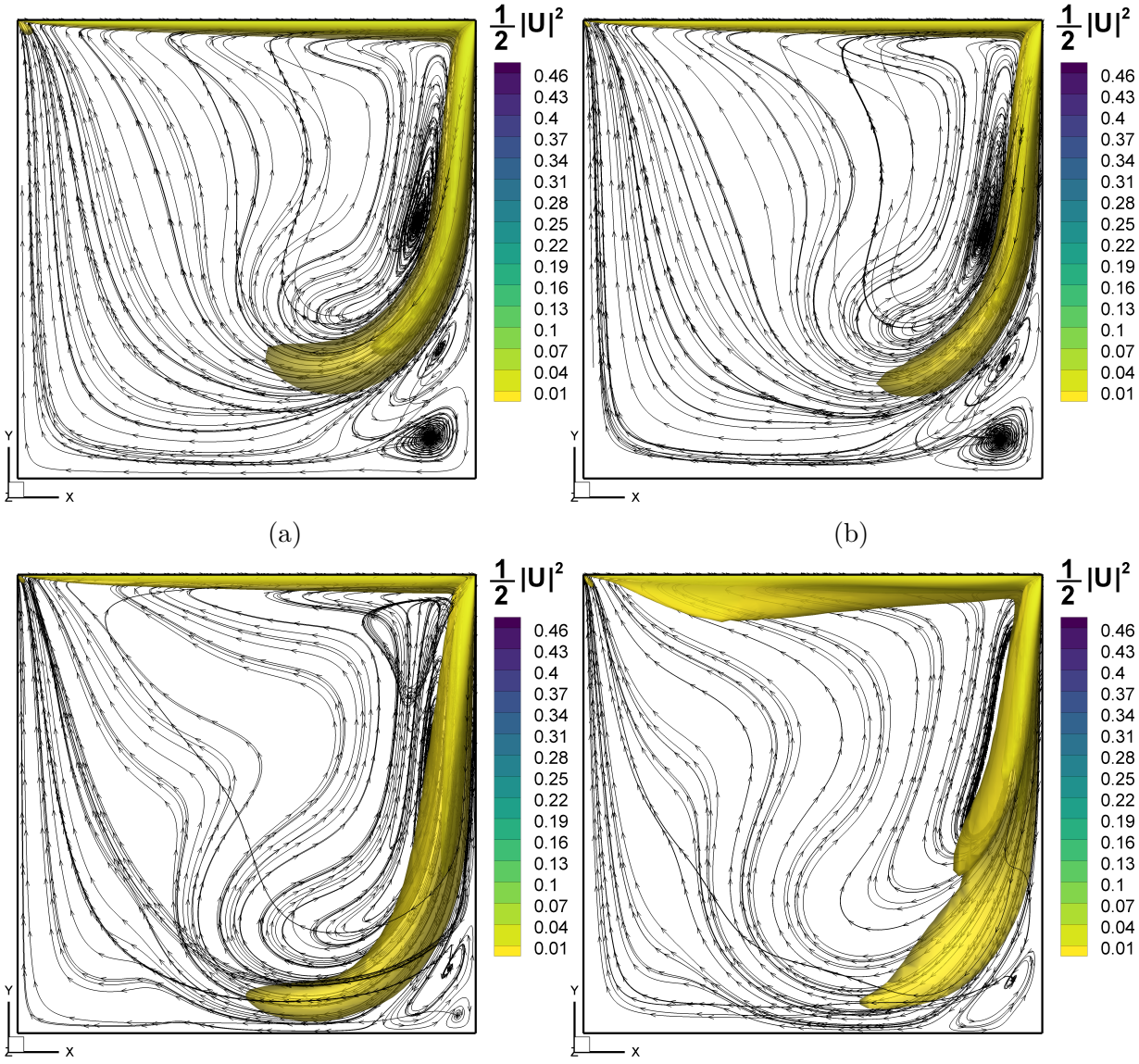


Figure 5.21: Kinetic energy iso-surfaces and three-dimensional velocity streamlines for (a) $Re_m = 1$, (b) $Re_m = 100$, (c) $Re_m = 500$, and (d) $Re_m = 1000$.

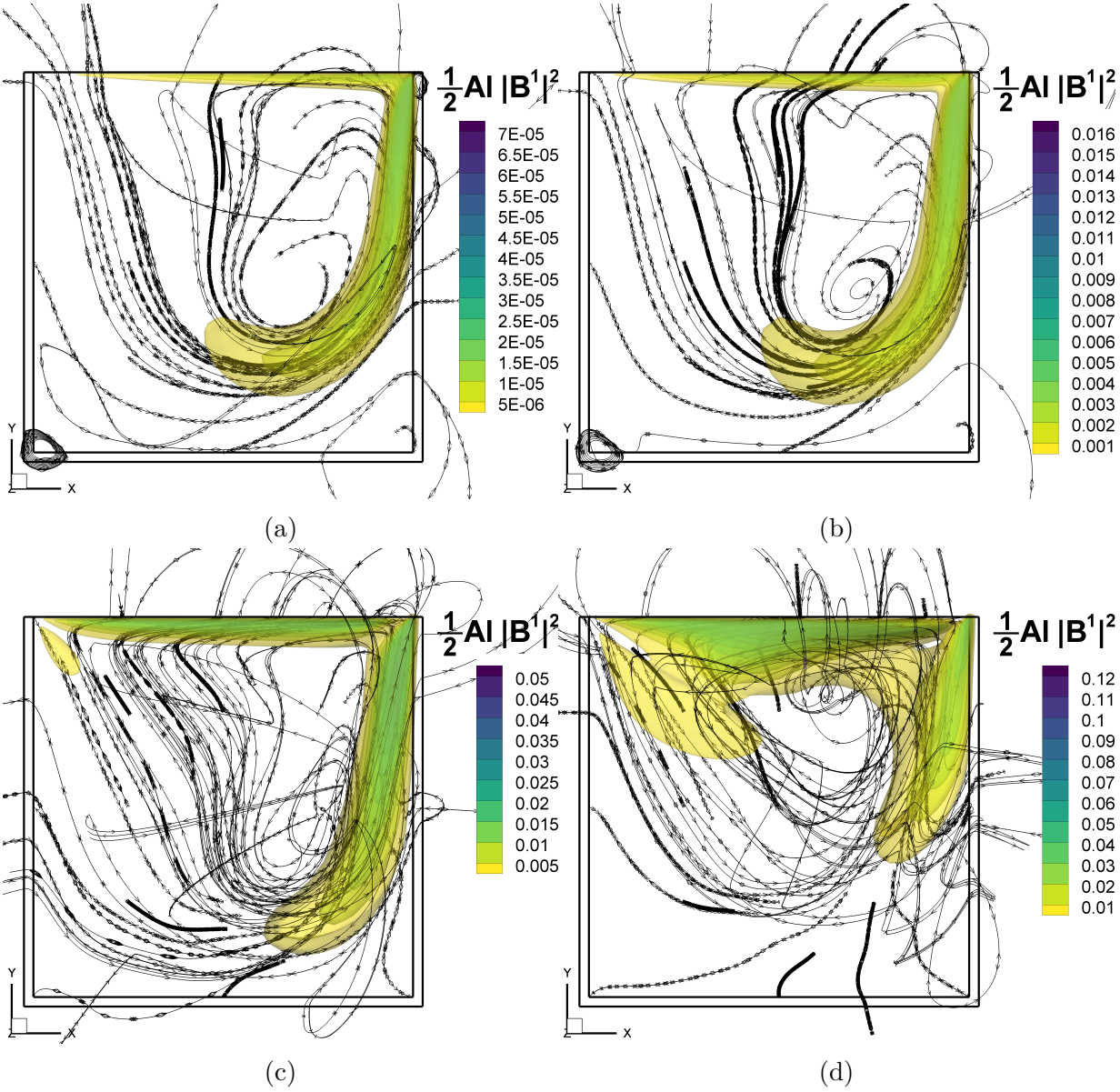


Figure 5.22: Induced magnetic field energy iso-surfaces and streamtraces for (a) $Re_m = 1$, (b) $Re_m = 100$, (c) $Re_m = 500$, and (d) $Re_m = 1000$.

### 5.2.7 Linear and non-linear dynamo tests

In this section, tests for a kinematic and full dynamo are presented. For the kinematic dynamo test, the fluid flow equations are solved in the absence of the Lorentz force until the flow has reached a statistically steady state. Then, the velocity is frozen in time, and the induction equation is solved for the instantaneous velocity distribution. A given MHD flow

is considered to be a kinematic dynamo if the induced magnetic field increases boundlessly. Alternatively, the flow is considered not a kinematic dynamo if the induced magnetic field plateaus.

Results suggest that the MHD LDC flow may behave as a kinematic dynamo above a critical magnetic Reynolds number, $Re_{mcrit}$, (see Fig. 5.23). Due to the large time-scales associated with the growth of the induced magnetic field, it is difficult to precisely determine $Re_{mcrit}$. Another difficulty is that the induced magnetic field penetrates further into the vacuum, in proportion with $Re_m$ [see Eq. (2.15)], as $Re_m$ increases, and encroaches on the truncated boundary. Based on Fig. 5.23, we suspect that this flow has ingredients for a kinematic dynamo due to the rapid growth in induced magnetic energy with respect to the increase in $Re_m$. It is important to note that the applied magnetic field energy is different for each of $Re_m$, since the scaling for the energy [see Eq. (5.2)] includes $Re_m$.

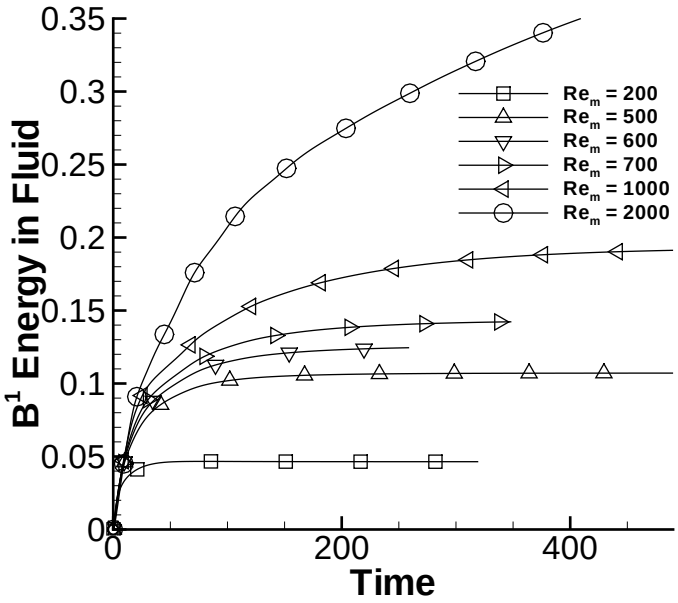


Figure 5.23: Induced magnetic field energy vs time for kinematic dynamo test.

For the full dynamo test, the coupled MHD equations are solved until the flow reaches a statistically steady state, and then the applied magnetic field is abruptly turned off. The MHD flow is considered to be a full dynamo if the induced magnetic field is sustained after

the applied field is turned off. A full dynamo occurs when the transfer of kinetic energy, which is injected into the system via the driving lid, into magnetic energy persists when the applied field is turned off. To our knowledge, a LDC has never been shown, let alone tested, to demonstrate dynamo physics. This test was only performed at $Re_m = 2000$ (see Fig. 5.24), since these computations are very expensive. The applied magnetic field was turned off at $t = 543.255$. Interestingly, there is a region of $\mathbf{B}^1$ energy growth at around $t = 600$, which seems to be a turning point where the $\mathbf{B}^1$ energy drops below the $\mathbf{B}^0$ energy. The $\mathbf{B}^1$ energy reaches a minimum of $E_{\mathbf{B}^1}(\Omega_f, t = 598.5) = 0.011$ and starts to significantly increase to a local maximum of $E_{\mathbf{B}^1}(\Omega_f, t = 607.3) = 0.0123$, after which the $\mathbf{B}^1$ energy continues on its nearly monotonic decent to zero.

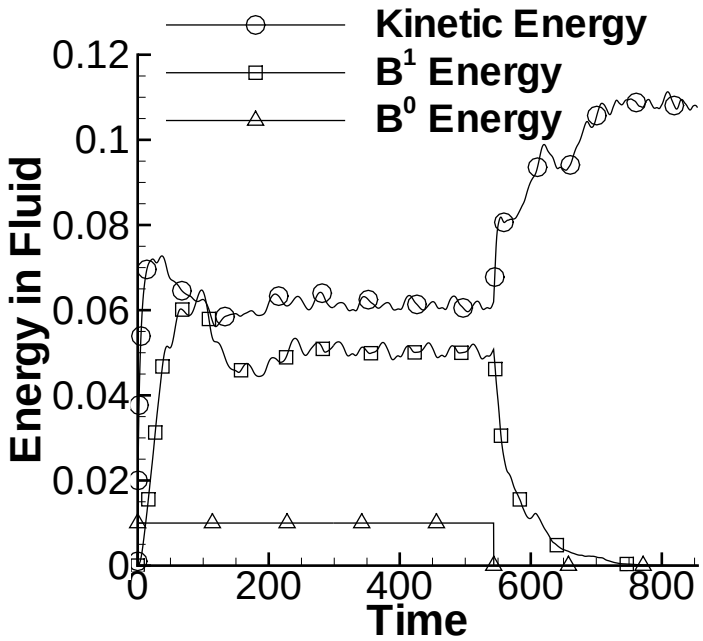


Figure 5.24: Kinetic and induced magnetic field energies vs time for full dynamo test at $Re_m = 2000$. $\mathbf{B}^0$ was turned off at $t = 543.255$.

## 5.3 Magnetic boundary conditions

### 5.3.1 Real vacuum magnetic boundary conditions

We consider a LDC MHD flow with a transversely applied magnetic field (Fig. 5.25) using RV BCs far from the conducting domain.

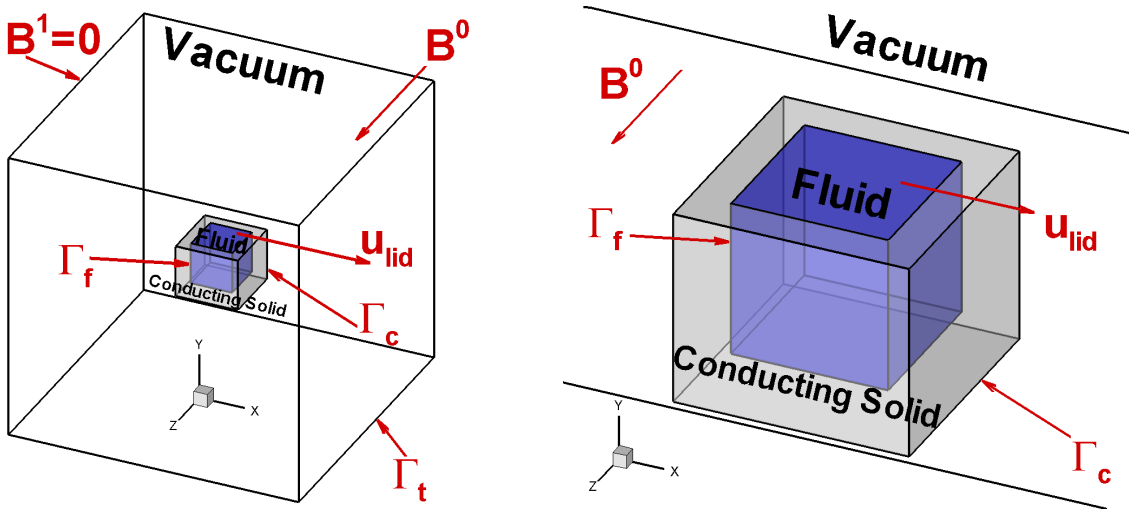


(a) Whole view. (b) Zoomed view.

Figure 5.25: LDC MHD flow schematic (left). Zoomed view (right).

Our preliminary results show that the magnetic lines travel far outside the conductor (Fig. 5.26a). Furthermore, kinetic energy and magnetic energy roughly spatially coincide, as seen in Fig. 5.26. This coincidence is expected since the fluid motion is the source of magnetic induction.

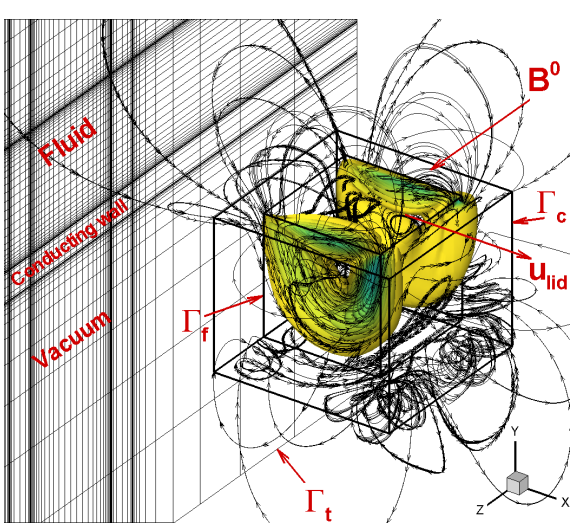


(a) $|\mathbf{B}|^2$ iso-surfaces and $\mathbf{B}^1$ lines.

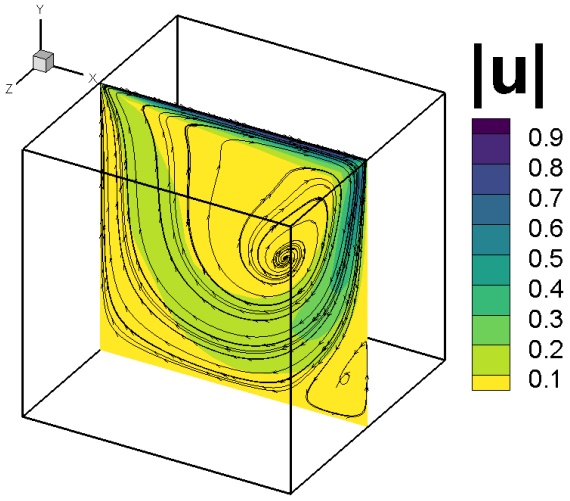


(b) Velocity magnitude and streamlines in the cavity mid-plane.

Figure 5.26: Results of a LDC MHD flow using RV BCs at $Re = 400$, $Ha = 20$, $Re_m = 100$, $t_{wall} = 0.5$.

### 5.3.2 Pseudo vacuum magnetic boundary conditions

Here, we consider the same setup studied using RV BCs (Fig. 5.25a), except $\Omega_v$ has been removed and PV BCs are applied at $\Gamma_c$ (Fig. 5.27).

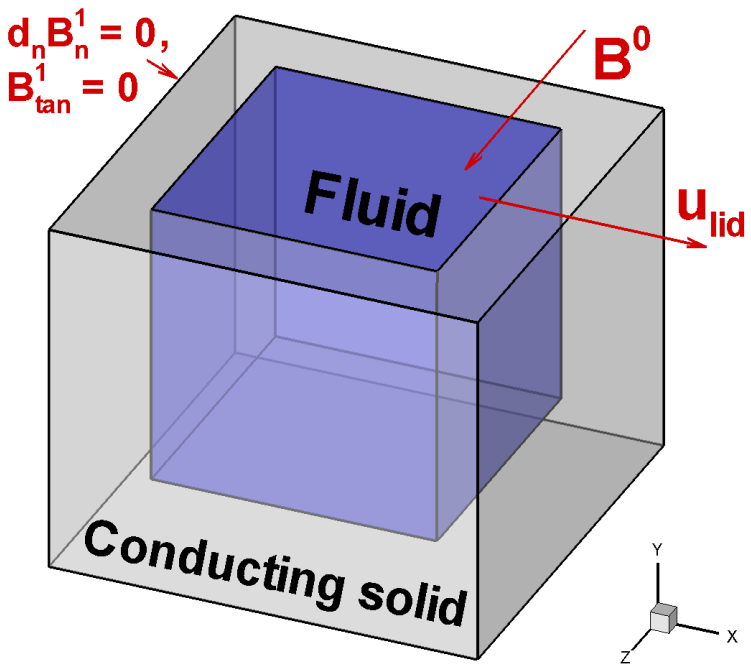

Figure 5.27: LDC MHD flow schematic for RV (left) and PV (right) BCs.

While the magnitude of the induced magnetic field in Fig. 5.28a appears similar to Fig. 5.26a, the induced magnetic field lines are not easily comparable because they do not close inside $\Omega_c$. In order to more easily compare the induced magnetic field lines, the induced magnetic field was reconstructed in $\Omega_v$, governed by Eq. (2.13), by solving $\partial_t \mathbf{B} + \nabla \times (\overline{\sigma}^{-1}\mathbf{j}_{PV}) = \nabla \times (\mathbf{u}_{PV} \times \mathbf{B}_{PV})$ using $\mathbf{B}|_{\Gamma_t} = \mathbf{0}$ for magnetic BCs. Here, $\mathbf{u}_{PV}$, $\mathbf{B}_{PV}$, and $\mathbf{j}_{PV}$ are steady solutions of $\mathbf{u}$, $\mathbf{B}$, and $\mathbf{j}$ computed using PV BCs on $\Gamma_c$ while $\mathbf{u}_{PV}$, $\mathbf{j}_{PV} = \mathbf{0}$ in $\Omega_v$. The reconstructed magnetic field from the PV case is shown in Fig. 5.28b.

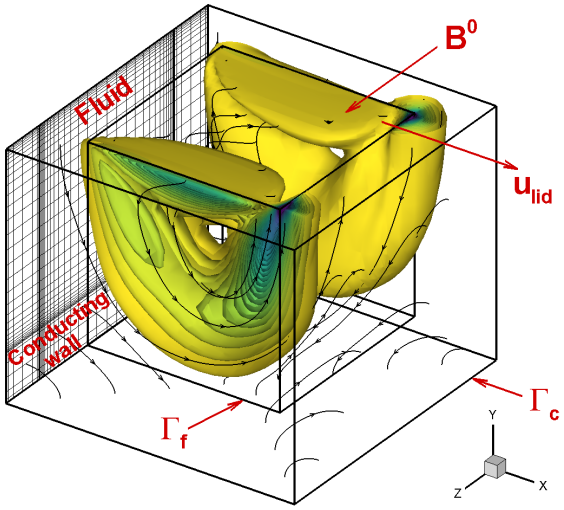


(a) PV BCs.

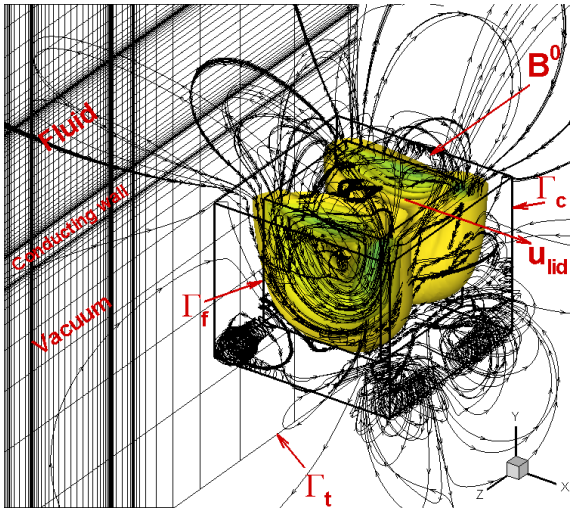


(b) PV BCs. **B** in vacuum has been reconstructed.

Figure 5.28: $|\mathbf{B}^1|^2$ iso-surfaces at $Re = 400$, $Ha = 20$, $Re_m = 100$, $t_{wall} = 0.5$.

It is important to note that PV BCs are incompatible with the moving lid BC in the high $Re_m$ limit. In this limit, magnetic field lines become *frozen* to the velocity field and, therefore, the total magnetic field lines become purely tangential at the driven lid (see Ref. [1]). PV BCs enforce the total magnetic field lines perpendicular to the boundary (see Fig. 5.29a), while RV BCs allow non-zero tangential components (see Figs. 5.29b and 5.30b), therefore we can expect to see significantly larger differences between PV and RV BCs as $Re_m$ is increased. One might argue that this problem is not suitable for a moderate $Re_m$ benchmark due to this incompatibility; however, we believe that this kinematic velocity boundary condition is very suitable because it provides a balance between kinematic and dynamic physics. Purely kinematic MHD flows were studied in Refs. [15, 64], however, they lack dynamics and **u** and **B** coupling. Fully coupled MHD flows have been studied in Ref. [45], however, these flows are complex and difficult to analyze. The driven cavity MHD flow provides a kinematic momentum, and induction, source term (the driven lid), which dynamically convects and diffuses "downstream" through the cavity.

### 5.3.3 Comparison of real and pseudo-vacuum magnetic boundary conditions

To compare RV and PV magnetic BCs for steady MHD flows as a function of $Re_m$, we compare the LDC MHD flows from the previous sections. Preliminary results show that PV BCs are a good approximation. The **B** energy distribution for PV and RV BCs are very well matched (Figs. 5.26a and 5.28a).

We observed that **u** and **j** distributions show a good match between RV and PV BCs, however, differences in the induced magnetic field lines can easily be seen (Figs. 5.29 and 5.30). Contours of the $|\mathbf{B}_{tangent}|$ were plotted on $\Gamma_c$. While these contours are trivially zero for PV BCs, non-zero tangential components are easily seen in Fig. 5.30 for RV BCs. What this study has shown us so far is that accuracy of the velocity and magnetic fields must be studied separately because, while **u** may match well between two different BCs, the magnetic field can appear quite different in magnitude. This is in agreement with the fact that the induced magnetic field does not enter the MHD equations at low $Re_m$ and will only introduce error as $Re_m$ increases.

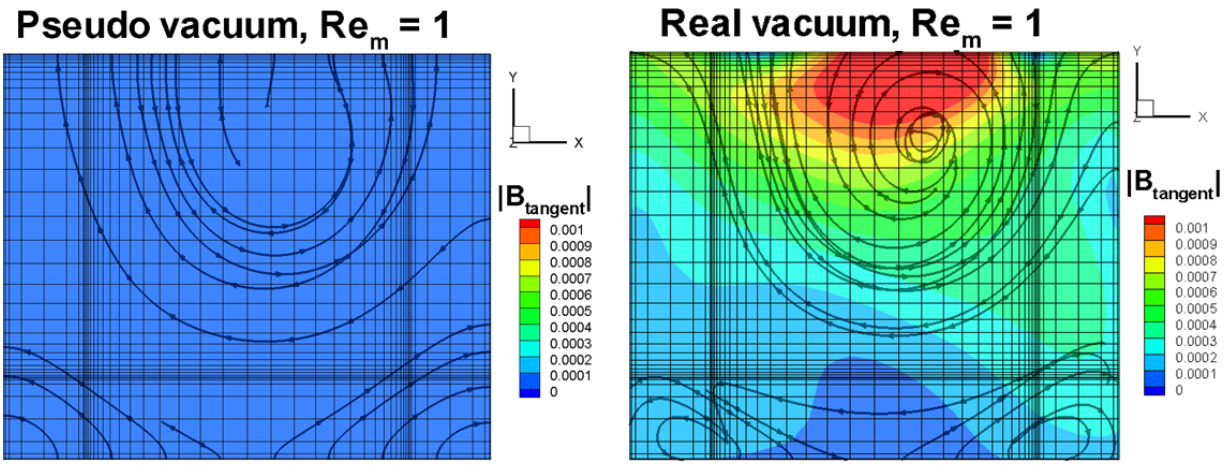


(a) PV BCs.

(b) RV BCs.

Figure 5.29: $|\mathbf{B}^1{}_{tangent}|$ at conductor surface for different BCs for $Re_m = 1$.

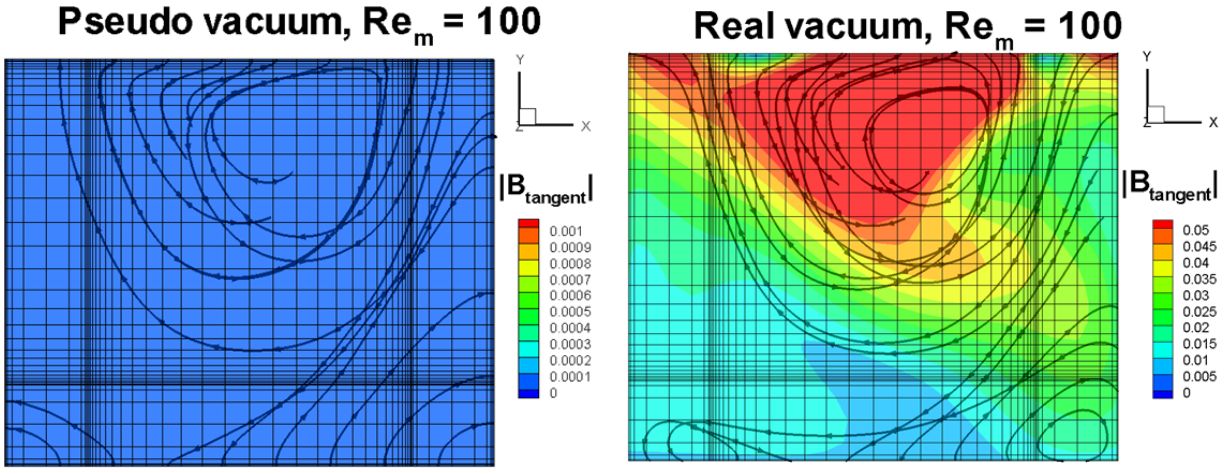


(a) PV BCs.

(b) RV BCs.

Figure 5.30: $|\mathbf{B}^1{}_{tangent}|$ at conductor surface for different BCs for $Re_m = 100$.

Results in § (5.2) suggest that the inductionless approximation appears valid in the $Re_m$ range $0 \leq Re_m \leq 100$ so long the flow is steady. Therefore, the PV BCs are expected to provide accurate results in this $Re_m$ range at steady-state. These BCs are likely invalid for unsteady flows, however, because significant differences in the integral kinetic energy are apparent for all $Re_m$. Therefore, a more systematic analysis of the applicability of PV BCs is necessary.

Furthermore, this analysis holds specifically for the LDC MHD flow at the given dimensionless parameters. There is no guarantee that PV BCs will provide accurate results for different flow configurations (an MHD flow over a sphere, or a duct MHD flow), flow regimes (e.g., turbulent or Q2D turbulent flows) and at different dimensionless parameters (higher $Re$, $Ha$, $Re_m$).

## 5.4 LM MHD flows induced by plasma disruptions

In this section, we present results of a LM MHD flow in the presence of a plasma disruption. Our focus region of the reactor is shown in Fig. 5.31. Different regions of the reactor are subject to varying strength magnetic fields and time-varying magnetic fields during a

disruption (Ref. [57]). Here, we consider a long enclosure with walls on all sides (Fig. 5.32). The time-varying poloidal field (Fig. 5.33) is due to the loss of toroidal plasma current. The time-varying $B_{poloidal}$ data was computed from a plasma code (DINA), used for plasma disruption calculations. The toroidal magnetic field, however, remains unchanged because it is generated by poloidal coils, hence the constant $B_{toroidal}$. To simplify our analysis, we neglect the radial field, which also decays but with a much smaller magnitude compared to the poloidal magnetic field. The yield strength of reduced-activation ferritic steel (F82H) is about 520 [MPa] (see Fig. 5 in Ref. [78]). It is essential that stresses in the solid structure do not exceed this limit as not to damage the blanket.

The dimensional and non-dimensional parameters are given in the following table:

| **Parameter** | **Value** |
|---|---|
| $\rho_{\text{lithium}}$ | 9300 [kg/m$^3$] |
| $\mu_{\text{lithium}}$ | 0.001 [kg/(m s)] |
| $\mu_{m\text{lithium}}$ | $1.2566 \times 10^{-6}$ [Ohm s/m] |
| $\sigma_{\text{lithium}}$ | $7 \times 10^5$ [Ohm$^{-1}$m$^{-1}$] |
| poloidal half-length | 1 [m] |
| toroidal half-length | 0.1 [m] |
| radial half-length | 0.1 [m] |
| $B_{toroidal}$ | 5 [T] |
| $B_{poloidal}$ | $\sim 1$ [T] |
| $L$ (characteristic length) | 0.1 [m] |
| $B^0$ (characteristic magnetic field) | 1 [T] |
| $\lvert\partial_t B_{poloidal}\rvert$ | $\sim 212.766$ [T/s] |
| $U \sim L\sqrt{\lvert B_{toroidal}\rvert\lvert\partial_t B^0{}_{poloidal}\rvert\frac{\sigma_{\text{lithium}}}{\rho_{\text{lithium}}}}$ | 28.29 [m/s] |
| $Re = \frac{UL}{\nu_l}$ | $26.31 \times 10^6$ |
| $Ha = BL\sqrt{\frac{\sigma_l}{\rho_l \nu_l}}$ | $2.65 \times 10^3$ |
| $Re_m = UL\sigma_l\mu_{ml}$ | 2.49 |

Table 5.1: Dimensional parameters for plasma disruption scenario.

To convert the dimensionless quantities to dimensional parameters in our numerical computations, Table (5.2) outlines the dimensional kinetic and magnetic energy scales and the EM force scale. The column "Dimensionless term" contains terms that are computed in MOONS.

| Quantity | Dimensionless term | Scale to multiply by | Scale value |
|---|---|---|---|
| Kinetic energy | $\int_V \frac{1}{2}\mathbf{u} \bullet \mathbf{u} dV$ | $\rho U^2 L^3$ | $7.4468 \times 10^3$ [J] |
| Magnetic energy | $Al \int_V \frac{1}{2}\mathbf{B} \bullet \mathbf{B} dV$ | $\rho U^2 L^3$ | $7.4468 \times 10^3$ [J] |
| EM force | $N\mathbf{j} \times \mathbf{B} dV$ | $\rho U^2 / L$ | $74.468 \times 10^6$ [N] |
| Maxwell Stress | $Al\mathbf{B} \otimes \mathbf{B}$ | $\rho U_c^2$ | 7.4468 [MPa] |
| Velocity field | $\mathbf{u}$ | $U$ | 28.29 [m/s] |
| Magnetic field | $\mathbf{B}$ | $B$ | 1 [T] |

Table 5.2: Conversion to dimensional values.

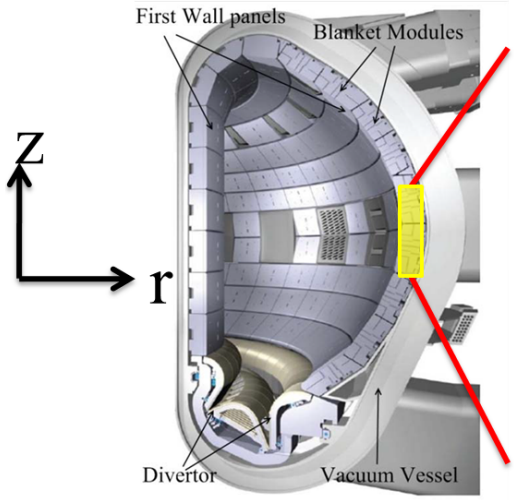


Figure 5.31: Our focused region in ITER tokamak.

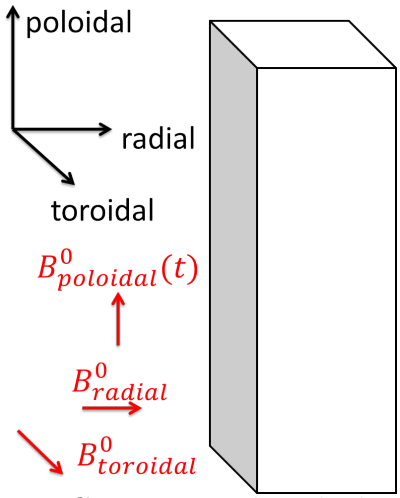


Figure 5.32: Geometry and applied magnetic field configuration.

Preliminary computations, performed at lower viscosity and lower applied magnetic field, show that the induced flow is circulating and symmetric about the radial mid-plane (Fig. 5.34). Animations were made in a short period of the simulation (shown in the red dotted box in Fig. 5.36) of the poloidal velocity in the poloidal mid-plane as a function of time, which showed strong velocity circulations, similar in appearance to the analytic solution we found, but with side BLs.

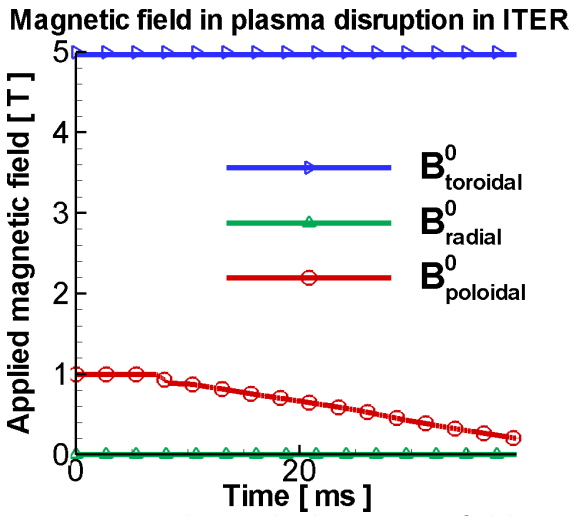


Figure 5.33: The applied magnetic field computed from the DINA plasma code.

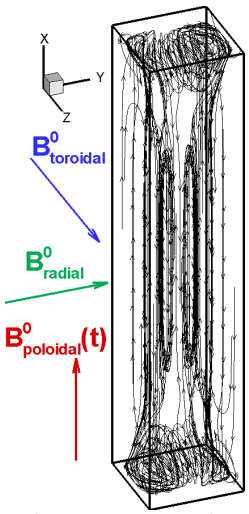


Figure 5.34: Velocity streamlines for preliminary computations for the plasma disruption scenario.

Due to the fine grid required to resolve the thin BL, the desired parameter space was too computationally expensive to perform full three-dimensional computations at the fusion-relevant parameter space. So, the geometry was simplified, to circumvent this difficulty, to a two-dimensional cross-section at the center of the poloidal section in Fig. 5.32 to reach the desired parameter space. This geometric simplification expanded the parameter space to visualize a characteristic velocity profile in the duct. Furthermore, we can compare this solution with the 1D analytic distribution derived in § (A.1).

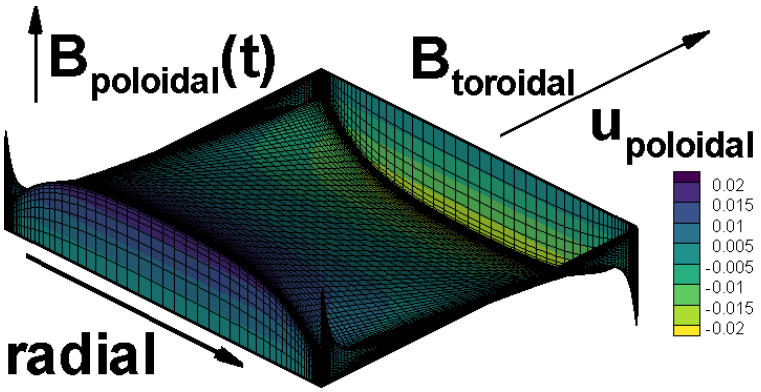


Figure 5.35: The poloidal velocity at $t = 1$.

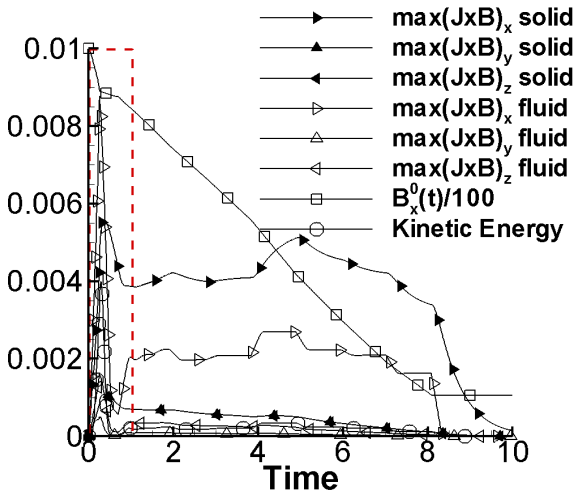


Figure 5.36: The poloidal magnetic field, Lorentz force, and kinetic energy vs. time.

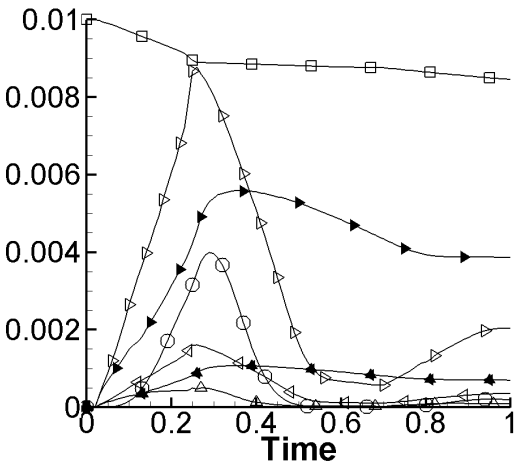


Figure 5.37: Zoomed view in the time range $0 \leq t \leq 1$.

As seen in Fig. 5.37, there are two important points in time in the unsteady event. First, the sudden increase in $|\partial_t B_{poloidal}|$ at roughly $t = 0.3$. The velocity reaches its maximum soon after this peak. Secondly, in the long decay time from $1 \leq t \leq 8$, as seen in Fig. 5.36, the velocity field distribution remains nearly unchanged. The velocity distribution in this long time window is shown in Fig. 5.35. Main velocity jets form near the Hartmann layers and corner velocity spikes form due to electric current paths. The maximum observed poloidal velocity was 2.3 [m/s].

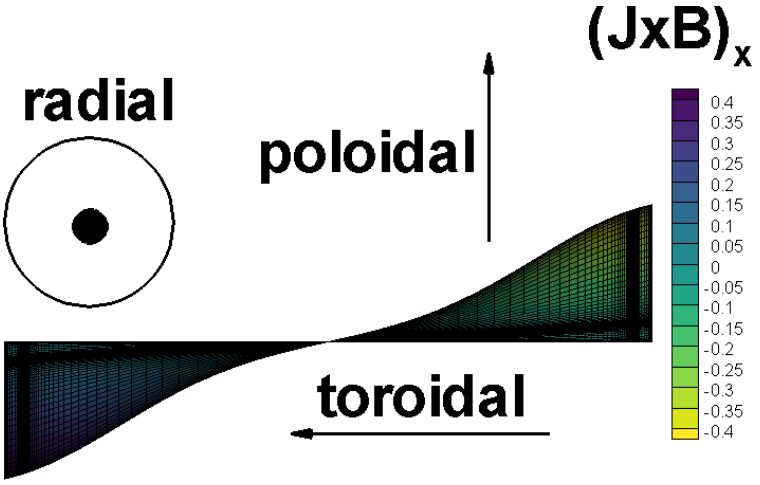


Figure 5.38: Solid bar: Lorentz force at $t = 0.4$.

In addition, computations for a reference case of a solid bar were performed to analyze and compare the EM forces between the solid bar and fluid bar cases. The $x$-component of the Lorentz force is plotted in Fig. 5.38 at $t = 0.4$. One interesting feature observed between the liquid and solid bar is that the Lorentz force is very concentrated in the walls in the case of the fluid bar, and is much more uniform in the solid bar case.

Preliminary results showed that shear stresses in the flow containing walls are lower for the fluid bar compared to the solid bar cases. This makes sense from an energy balance point of view. The energy input to the system enters through the time-varying and applied magnetic fields terms, which result in the substantial EM forces. In the case of the solid bar, energy can only be dissipated by Joule heat. In the fluid bar case, magnetic energy is converted into kinetic energy of the LM, which can dissipate energy through viscous dissipation.

# CHAPTER 6

# Concluding Remarks

## 6.1 Conclusions

In this study, mathematical and numerical methodologies were developed, and an induction-based incompressible MHD flow solver was created, to study moderate LM MHD flows for fusion blanket design.

First, we focused on the reference case of an incompressible LDC MHD flow subject to a transversely applied magnetic field. The primary focus in the study was on the effect of the magnetic Reynolds number on the flow inside an electrically conducting square cavity driven by a moving lid and on the magnetic field generated by the flowing liquid. To address such effects, the $Re_m$ was changed in the computations from low values typical to the inductionless approximation ($Re_m << 1$) to moderate and even high $Re_m$ (up to 2000) for which dynamo-type physics might be expected, while the hydrodynamic Reynolds number and the Hartmann number were constant, at 2000 and 100 respectively. The computational domain included the electrically conducting fluid, surrounding solid walls and an outer vacuum domain, which is sufficiently large to ensure physically correct far-field magnetic BCs. First, a new three-dimensional numerical code was developed and carefully tested using the induced magnetic field as the primary electromagnetic variable, and then the code was applied to the LDC flow to reveal for the first time a specific flow physics associated with moderate $Re_m$, which was found to be very different from both the purely hydrodynamic flows and MHD flows at low $Re_m$. Many new exciting features have been observed with regard to the effect of $Re_m$ on the MHD BL and the bulk flow, generation of a magnetic field and its penetration into vacuum, energy balance (including kinetic and magnetic field energy distributions), frozen magnetic field behavior and associated magnetic field expulsion from

the fluid domain, transition to unsteady flows, and self-excitation of the magnetic field and the associated dynamo-type action at high $Re_m$. In addition to these exciting observations we expect that the detailed velocity and magnetic field distributions obtained in this study for the variety of $Re_m$ will help to establish a new database necessary for benchmarking of existing and new full induction MHD codes, which are needed for successful advancement of several vital applications such as liquid metal blankets of a fusion power reactor.

A summary of changes that happen in the flow and associated flow and magnetic field features as $Re_m$ is increased from much less than unity to the maximum value ($Re_m = 2000$) employed in the present computations is the following. First of all, we have noticed a significant difference in the effect of $Re_m$ on the flow between steady and time-dependent flows, including truly unsteady flows and those transitioning from the initial condition to a steady-state. In steady-state flows, we observed that the $Re_m$ effect on the flow is negligible for $Re_m \lesssim 100$ as seen from the integral kinetic energy versus $Re_m$ plotted in Fig. 5.19b, and from the velocity distributions shown in Fig. 5.5 for several $Re_m$ values. At the same time, the induced magnetic field in this range of $Re_m$ changes linearly in magnitude with $Re_m$, but its distribution is qualitatively the same. Moreover, the induced magnetic field is much smaller compared to the applied one in this $Re_m$ range. These observations suggest that the inductionless approximation is still valid (at least for particular values of $Re$ and $Ha$ used in this study) even for $Re_m \sim 1$ and higher, $1 < Re_m \lesssim 100$. This conclusion, however, is not applicable to time-dependent flows, for which the validity of the inductionless approximation seems to be limited to the conventional restriction $Re_m << 1$.

All computed solutions converged eventually to a steady-state except for two cases at the highest $Re_m = 1500$ and $Re_m = 2000$. For $100 \lesssim Re_m \lesssim 1000$, the flow is steady but the magnetic Reynolds number has a non-linear effect on the flow as seen from the magnetic field plot in Fig. 5.19b and Eq. (5.10). Equation (5.10) approximates the integral induced magnetic field in the flow domain as a cubic polynomial of $Re_m$. Clearly, the inductionless approximation is not valid for $Re_m > 100$. The magnetic energy grows fast as $Re_m$ is increased while the kinetic energy almost does not significantly change. The

kinetic energy and the magnetic energy were estimated to become equal at $Re_m = 1320$, [based on Eq. (5.10)], based on the behavior of the induced magnetic field in the range $0 \leq Re_m \leq 1000$. However, additional computations revealed that the flow remains in the kinetic energy-dominated regime at $Re_m = 1500$ and even $Re_m = 1500$, where a significant increase in the integral kinetic energy and a nominally lower increase in the induced magnetic field energy occur. Also, the flow becomes unsteady and results in full three-dimensional (non-symmetric with respect to the $z = 0$ plane) solutions. Another characteristic value is $Re_m \approx 850$ such that for all $Re_m$ higher than 850, the averaged magnetic field in the flow domain is higher than the applied one as seen in Fig. 5.4.

Magnetic Reynolds numbers higher than 100 were found to have a substantial effect on the flow structure. Both the Hartmann layers and the 2D bulk flow typical to low $Re_m$, or high $Ha$, MHD flows seem to experience significant modifications compared to the flows for which the inductionless approximation is valid. In particular, our results show that the flow is mostly two-dimensional (except for the Hartmann layers) when $Re_m < 100$, but becomes more three-dimensional as $Re_m$ increases.

A distinguished feature of the induced magnetic field is its penetration into the vacuum domain. The computations show that the behavior of the magnetic field in the insulating outer domain is similar to that of the magnetic dipole. Namely, far from the liquid domain where the magnetic field is generated, the magnetic field strength drops very fast—as one divided by the cubic distance from the conductor, in agreement with the Biot-Savart law. In doing so, about 97% of the induced magnetic energy is located in the conducting domain for all $Re_m$. About 4% of the energy is located in the conducting wall and at most 3% of the energy is located in the vacuum (Fig. 5.20).

The observed changes in the flow and magnetic field behavior at high $Re_m \sim 10^2$-$10^3$ (non-linearity, unsteadiness, kinetic energy dominating over magnetic energy and high magnitudes of the induced magnetic field) motivated us to perform special tests to see whether or not the LDC flow can exhibit a dynamo action. Two particular numerical experiments were conducted to check for linear (kinematic) and non-linear dynamos. In the kinematic dynamo

test, the full induction problem was solved for a given hydrodynamic velocity field computed in the absence of the Lorentz force. Results suggest that the MHD LDC flow may exhibit a kinematic dynamo action above a critical $Re_m$. In the non-linear dynamo test, the coupled MHD equations are solved until the flow reaches a statistically steady state, and then the applied magnetic field is abruptly turned off. This test was only performed at $Re_m = 2000$, since such computations are costly. Although no dynamo action was demonstrated, a local peak in the magnetic energy was observed suggesting that the full dynamo might be possible at higher $Re_m$.

The results obtained in this study for moderate and high $Re_m$ are also useful for implementation of approximate PV BCs as briefly discussed in § (1.2.6). It is important to note that PV BCs are the true BCs for $Re_m << 1$ (Ref. [45]) but incompatible with the moving lid BC in the high $Re_m$ limit. In this limit, magnetic field lines become frozen to the velocity field and, therefore, magnetic field lines become purely tangential at the driving lid. Pseudo-vacuum magnetic BCs enforce the magnetic field lines to stretch perpendicular to the boundary, which are nearly matched by the $Re_m = 1$ case (see Fig. 5.22a), while RV BCs allow non-zero tangential field components (Figs. 5.22b, 5.22c, 5.22d), therefore we can expect to see significantly larger differences in the results between PV and RV BCs as $Re_m$ is increased. Obtaining the $Re_m$ limits for the use of the approximate PV BCs is an important practical goal as utilization of such BCs would allow much cheaper computations that do not require solving the induction equation in the outer domain. Although no full systematic studies on the comparison of different BC types were performed in the present study, our results suggest that the PV BCs should apply to steady-state flows for $Re_m$ up to several hundred until frozen magnetic field effects become pronounced. A dedicated, detailed study is needed in the future to address this issue for different flows and flow regimes, first of all for unsteady flows, for which applicability of the PV BCs seem to be more limited compared to steady-state flows.

# Appendix A

# Appendix

## A.1 Analytic 1D solution to an unsteady applied magnetic field induced flow

Here, we briefly derive the analytic solution to the 1D analytic solution for flow induced due to an unsteady applied magnetic field. The dimensional momentum and induction equations are:

$$\begin{aligned} \partial_t u_i + u_j \partial_j u_i = -\frac{1}{\rho}\partial_i p + \nu \partial_{jj} u_i + \frac{1}{\rho \mu_{ml}}(B_j \partial_j B_i - \tfrac{1}{2}\partial_i B_j B_j), \\ \partial_t B_i = \frac{1}{\sigma_l \mu_{ml}} \partial_{jj} B_i - \partial_j (u_j B_i - u_i B_j). \end{aligned} \tag{A.1}$$

Consider a steady channel flow and induced magnetic field, with no changes along $x$ and $y$, and $v = 0$ and $w = 0$, $\partial_t B_z^0 = \partial_t B_y^0 = 0$. Further assume a steady time varying magnetic field $\partial_t B_z^0$, a steady $B_x^0$ and no pressure gradient $\partial_x p = 0$. Our governing equations simplify to

$$\begin{aligned} \partial_{zz} u = -\frac{1}{\rho \nu \mu_{ml}} B_z^0 \partial_z B_x \\ \partial_{zz} B_x = \sigma_l \mu_{ml} \partial_t B_x^0 - \sigma_l \mu_{ml} B_z^0 \partial_z u \end{aligned} \tag{A.2}$$

More compactly, we have

$$u'' = -A B_x^{1\prime}, \qquad B_x^{1\prime\prime} = C - D u', \tag{A.3}$$

Where

$$A = \frac{1}{\rho \nu \mu_{ml}} B_z^0, \qquad C = \sigma_l \mu_{ml} \partial_t B_x^0, \qquad D = \sigma_l \mu_{ml} B_z^0. \tag{A.4}$$

To solve this system of equations, we first decouple the equations by using the transfor-

mations:

$$\begin{aligned} X &= u + FB_x^1, \qquad u = \frac{1}{2}\left(X+Y\right), \\ Y &= u - FB_x^1, \qquad B_x^1 = \frac{1}{2F}\left(X-Y\right), \qquad F = \sqrt{\frac{A}{D}}. \end{aligned} \tag{A.5}$$

Substituting this transformation into the governing equation yields the following decoupled equations:

$$X'' + FDX' = FC, \qquad Y'' - FDY' = -FC. \tag{A.6}$$

The general solution to this system of equations is

$$X = \frac{C}{D}z + \frac{e^{-FDz}}{FD}\alpha_1 + \alpha_2, \qquad Y = \frac{C}{D}z + \frac{e^{+FDz}}{FD}\beta_1 + \beta_2. \tag{A.7}$$

To determine the particular solution, we apply boundary conditions $u = 0, B_x^1 = 0$ at $z = [-a, a]$ to determine coefficients $\alpha_1, \alpha_2, \beta_1, \beta_2$. The coefficients, we found, are

$$\begin{aligned} \alpha_1 &= \frac{+2FCa}{(e^{+FDa} - e^{-FDa})} = +\frac{FCa}{\sinh(FDa)}, \\ \beta_1 &= \frac{-2FCa}{(e^{+FDa} - e^{-FDa})} = -\frac{FCa}{\sinh(FDa)}, \\ \alpha_2 &= -\frac{Ca}{D\sinh(FDa)}(\sinh(FDa) + e^{-FDa}), \\ \beta_2 &= -\frac{Ca}{D\sinh(FDa)}(\sinh(FDa) - e^{+FDa}). \end{aligned} \tag{A.8}$$

After substituting these coefficients into the general solution and simplifying, we obtain

$$\begin{aligned} X &= \frac{aC}{D}\left[\frac{z}{a} - 1 + \frac{1}{\sinh(FDa)}\left(e^{-FDz} - e^{-FDa}\right)\right], \\ Y &= \frac{aC}{D}\left[\frac{z}{a} - 1 + \frac{1}{\sinh(FDa)}\left(-e^{FDz} + e^{FDa}\right)\right]. \end{aligned} \tag{A.9}$$

Substituting these solutions into the inverse transformations to obtain the primitive variable

solutions and simplifying yields

$$\begin{aligned} B_x^1 &= -\sqrt{\mu\sigma_l a^2 {\mu_m}^2}\frac{1}{B_z^0}\frac{\partial B_x^0}{\partial t}\left(\frac{1}{\tanh(Ha)} - \frac{\cosh\left(Ha\frac{z}{a}\right)}{\sinh(Ha)}\right), \\ u &= -a\frac{1}{B_z^0}\frac{\partial B_x^0}{\partial t}\left(\frac{\sinh\left(Ha\frac{z}{a}\right)}{\sinh(Ha)} - \frac{z}{a}\right), \\ Ha &= aB_z^0\sqrt{\frac{\sigma_l}{\rho\nu}}. \end{aligned} \tag{A.10}$$

Non-dimensionalizing using scales $[z] = a, [t] = \frac{L}{U}, [U] = U, [B] = B_z^0, [J] = \sigma_l UB$, yields our final dimensionless solution:

$$\begin{aligned} B_x^{1*} &= -\frac{Re_m}{Ha}\frac{1}{B_z^{0*}}\frac{\partial B_x^{0*}}{\partial t^*}\left(\frac{1}{\tanh(Ha)} - \frac{\cosh\left(Haz^*\right)}{\sinh(Ha)}\right), \\ u^* &= -\frac{1}{B_z^{0*}}\frac{\partial B_x^{0*}}{\partial t^*}\left(\frac{\sinh\left(Haz^*\right)}{\sinh(Ha)} - z^*\right), \\ Re_m &= \sigma_l\mu_m Ua, \qquad Ha = aB_z^0\sqrt{\frac{\sigma_l}{\rho\nu}}. \end{aligned} \tag{A.11}$$

Bibliography

[1] R. Moreau, magnetohydrodynamics, Kluwer, 1990.

[2] R. Munipalli, A comprehensive high performance predictive tool for fusion liquid metal hydromagnetics, Technical Report, HyPerComp Inc., Westlake Village, CA (United States), 2014.

[3] J. D. Kotulski, M. Ulrickson, IEEE/NPSS 24th Symp. Fusion Eng. (2011) 0–4.

[4] G. K. Batchelor, Proc. R. Soc. London. Ser. A 201 (1950) 405–416.

[5] A. Gailitis, O. Lielausis, S. Dement, et al., Phys. Rev. Lett. (2000) 4365–4368.

[6] P. A. Davidson, Introduction to magnetohydrodynamics, volume 55, Cambridge university press, 2016.

[7] M. Abdou, C. Maynard, Nuclear Science and Engineering 56 (1975) 381–398.

[8] M. Abdou, N. B. Morley, S. Smolentsev, et al., Fusion Eng. Des. 100 (2015) 2–43.

[9] S. Smolentsev, S. Badia, R. Bhattacharyay, et al., Fusion Eng. Des. 100 (2015) 65–72.

[10] S. Smolentsev, R. Moreau, M. Abdou, Fusion Eng. Des. 83 (2008) 771–783.

[11] G. Guj, F. Stella, J. Comput. Phys. 298 (1993) 286–298.

[12] U. Ghia, K. N. Ghia, C. Shin, J. Comput. Phys. 411 (1982) 387–411.

[13] J. Priede, S. Aleksandrova, S. Molokov, J. Fluid Mech. 649 (2010) 115.

[14] M. Kinet, B. Knaepen, S. Molokov, Phys. Rev. Lett. 103 (2009) 1–4.

[15] N. O. Weiss, Proc. R. Soc. A Math. Phys. Eng. Sci. 293 (1966) 310–328.

[16] A. Jackson, A. Sheyko, P. Marti, et al., Geophys. J. Int. 196 (2013) 712–723.

[17] S. Smolentsev, S. Cuevas, A. Beltran, J. Comput. Phys. 229 (2010) 1558–1572.

[18] I. E. Sarris, G. K. Zikos, a. P. Grecos, N. S. Vlachos, Numer. Heat Transf. Part B Fundam. 50 (2006) 157–180.

[19] N. B. Salah, A. Soulaimani, W. Habashi, Comput. Methods Appl. Mech. Engrg. 190 (2001) 5867–5892.

[20] J. A. Shercliff, G. K. Batchelor, Math. Proc. Cambridge Philos. Soc. 49 (1953) 136.

[21] J. C. R. Hunt, K. Stewartson, J. Fluid Mech. 23 (1965) 563.

[22] S. Smolentsev, N. Morley, M. Abdou, Fusion Eng. Des. 73 (2005) 83–93.

[23] L. Barleon, U. Burr, K. Mack, R. Stieglitz, Fusion Eng. Des. (2000) 723–733.

[24] J. Young, S. Smolentsev, M. Abdou 89 (2014) 1163–1167.

[25] R. Klein, A. Potherat, Phys. Rev. Lett. 104 (2010) 1–4.

[26] S. Smolentsev, R. Moreau, Phys. Fluids 19 (2007) 078101.

[27] L. E. P. M. Madylam, E. Bp, S. Martin, H. Cedex, J. Fluid Mech. 456 (2002) 137–159.

[28] R. Chaudhary, S. P. Vanka, B. G. Thomas, Phys. Fluids 22 (2010) 1–15.

[29] S. Khan, J. N. Davidson, Ann. Nucl. Energy 6 (1979) 499–509.

[30] M. Bourgoin, P. Odier, J. F. Pinton, Y. Ricard, Phys. Fluids 16 (2004) 2529–2547.

[31] G. A. Glatzmaier, P. H. Roberts, Nature 377 (1995) 203–209.

[32] F. Hamba, M. Tsuchiya, Phys. Plasmas 17 (2010) 012301.

[33] U. Müller, R. Stieglitz, Naturwissenschaften (2000) 381–390.

[34] A. Gailitis, O. Lielausis, E. Platacis, et al., Phys. Rev. Lett. (2001).

[35] S. Kenjereš, New J. Phys. (2007).

[36] A. B. Iskakov, A. A. Schekochihin, S. C. Cowley, J. C. Mcwilliams, M. R. E. Proctor, Phys. Rev. Lett. 208501 (2007) 2–5.

[37] V. Bandaru, I. Sokolov, T. Boeck, IEEE Trans. Magn. 9464 (2016) 1–1.

[38] R. Kaiser, A. Tilgner, Phys. Rev. E 60 (1999) 2949–2952.

[39] E. Bullard, D. Gubbins, Geophys. Astrophys. Fluid Dyn. 101 (1976).

[40] T. V. S. Sekhar, R. Sivakumar, T. V. R. R. Kumar (2009) 1351–1368.

[41] B. Knaepen, S. Kassinos, D. Carati, J. Fluid Mech. 513 (2004) 199–220.

[42] H. Kamkar, H. K. Moffatt, J. Fluid Mech. 121 (1982) 107.

[43] V. Bandaru, J. Pracht, T. Boeck, J. Schumacher, Theor. Comput. Fluid Dyn. 29 (2015) 263–276.

[44] C. Kawczynski, S. Smolentsev, M. Abdou, Fusion Eng. Des. (2016) 2–5.

[45] V. Bandaru, T. Boeck, D. Krasnov, J. Schumacher, J. Comput. Phys. 304 (2016) 320–339.

[46] A. B. Iskakov, S. Descombes, E. Dormy, J. Comput. Phys. 197 (2004) 540–554.

[47] A. Iskakov, E. Dormy, Geophys. Astrophys. Fluid Dyn. 99 (2005) 481–492.

[48] C. Gissinger, A. Iskakov, S. Fauve, E. Dormy, Europhys. Lett. 82 (2008) 29001.

[49] J. Thelen, F. Cattaneo, Mon. Not. R. Aston. Soc. 17 (2000).

[50] J. A. Shercliff, J. Fluid Mech. 1 (1956) 644–666.

[51] A. Pothérat, J. Sommeria, R. Moreau, Phys. Fluids 14 (2002) 403–410.

[52] R. Avalos-zuniga, F. Plunian, A. Gailitis (2003) 1–8.

[53] J. Brackbill, J. Comput. Phys. 430 (1980) 426–430.

[54] G. Tóth, J. Comput. Phys. 161 (2000) 605–652.

[55] D. S. Balsara, D. S. Spicer, J. Comput. Phys. 149 (1999) 270–292.

[56] T. S. Tricco, D. J. Price, J. Comput. Phys. 231 (2016) 7214–7236.

[57] L. R. Turner, IEEE Trans. Magn. 26 (1990).

[58] A. H. Boozer, Phys. Plasmas 19 (2012).

[59] G. Tóth, J. Comput. Phys. 161 (2000) 605–652.

[60] J. Sommeria, R. Moreau, S. J. &. M. R., J. Fluid Mech. 118 (1982) 507.

[61] Y. Ponty, P. D. Mininni, D. C. Montgomery, et al., Phys. Rev. Lett. 94 (2005) 2–5.

[62] D. Jackson John, Classical electrodynamics, 1999.

[63] B. S. A. Jepps, J. Fluid Mech. 67 (1975).

[64] J. L. Guermond, J. Léorat, C. Nore, Eur. J. Mech. B/Fluids 22 (2003) 555–579.

[65] G. Rüdiger, Y. Zhang, Astron. Astrophys. 378 (2001) 302–308.

[66] R. H. Pletcher, J. C. Tannehill, D. Anderson, Computational Fluid Mechanics And Heat Transfer, CRC Press, 2012.

[67] J. Perot, J. Comput. Phys. 108 (1993) 51–58.

[68] C. R. Evans, J. F. Hawley, Astrophys. J. 332 (1988) 659–677.

[69] J. Kim, P. Moin, J. Comput. Phys. 323 (1985) 308–323.

[70] H. Le, P. Moin, J. Comput. Phys. 379 (1991).

[71] A. J. Chorin, Math. Comput. 22 (1968) 745.

[72] P. J. Roache, Annu. Rev. Fluid. Mech. 29 (1997) 123–60.

[73] P. J. Roache, Error Bars for CFD, in: 41st Aerosp. Sci. Meet. Exhib., January, 2003, pp. 6–9. doi:10.2514/6.2003-408.

[74] J. Hunt, Proc. R. Soc. London Ser. A-Mathematical Phys. Eng. Sci. 293 (1966) 342–358.

[75] M. J. Pattison, K. N. Premnath, N. B. Morley, M. A. Abdou, Fusion Eng. Des. 83 (2008) 557–572.

[76] H. Araseki, J. Comput. Phys. 110 (1994) 301–309.

[77] E. Leriche, S. Gavrilakis, Phys. Fluids 12 (2000).

[78] R. Kasada, D. Ishii, M. Ando, H. Tanigawa, M. Ohata 100 (2015) 146–151.